In presenting the dissertation as a partial fulfillment of the requirements for an advanced degree from the Georgia Institute of Technology, I agree that the Library of the Institute shall make it available for inspection and circulation in accordance with its regulations governing materials of this type. I agree that permission to copy from, or to publish from, this dissertation may be granted by the professor under whose direction it was written, or, in his absence, by the Dean of the Graduate Division when such copying or publication is solely for scholarly purposes and does not involve potential financial gain. It is understood that any copying from, or publication of, this dissertation which involves potential financial gain will not be allowed without written permission.

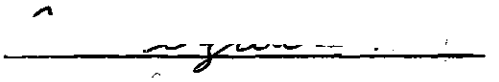

7/25/68

ANGULAR DISTRIBUTION OF H(2s) FORMED BY ELECTRON CAPTURE AND DISSOCIATION COLLISIONS

A THESIS

Presented to

The Faculty of the Graduate Division

by

Roger Louis Fitzwilson

In Partial Fulfillment

of the Requirements for the Degree

Doctor of Philosophy

in the School of Physics

Georgia Institute of Technology

August, 1971

ANGULAR DISTRIBUTION OF H(2s) FORMED BY ELECTRON CAPTURE

AND DISSOCIATION COLLISIONS

Approved:

Chairman

Date approved by Chairman: 8-6-71

ACKNOWLEDGMENTS

It is my pleasure to thank Dr. E. W. Thomas for the guidance and encouragement provided while this research was being performed. His exceptional ability as an experimental physicist and his untiring patience give him the qualities of an outstanding advisor. The helpful comments by Dr. J. W. Hooper and Dr. T. F. Moran on this manuscript are appreciated.

I would like to thank Mr. Isidor Sauers for his assistance in taking portions of the dissociation data. Thanks also go to Mr. K. B. Springfield of the School of Physics and Mr. J. D. Dameron and Mr. T. Hardin of the Mechanical Services Branch of the Engineering Experiment Station for their useful suggestions and excellent workmanship in the construction of the several components of this apparatus.

This work was partially supported by the Controlled Thermonuclear Research Program, Division of Research, U. S. Atomic Energy Commission. A three-year traineeship from the National Aeronautics and Space Administration permitted full-time work on this study. I am appreciative of these sources of support.

Thanks go to Miss Wynette Wright for the typing of the rough draft and to Mrs. Lydia Geeslin for her expert typing of the final manuscript.

Finally, I would like to give special thanks to my wife, Phyllis, for her encouragement and support throughout my graduate program.

TABLE OF CONTENTS

	Page
ACKNOWLEDGMENTS	ii
LIST OF TABLES	vi
LIST OF ILLUSTRATIONS	vii
SUMMARY	ix
Chapter	
I. INTRODUCTION	1
II. OPERATIONAL DEFINITION OF A DIFFERENTIAL CROSS SECTION	7
III. PREVIOUS WORK — EXPERIMENTAL AND THEORETICAL	18
Previous Experimental Work for Electron Capture	18
Previous Theoretical Work for Electron Capture	25
Classical Scattering of Heavy Particles	27
Coupled-State Impact Parameter Method	32
Molecular Model and Semi-Empirical Formulae	35
Previous Dissociation Work — Experimental and Theoretical	38
IV. APPARATUS	42
Accelerator	43
Vacuum Chamber	45
Module Support System	48
Beam Preparation Modules	53
Target Chamber and Gas Feed System	55
Scattered Flux Collimator	57
Metastable Detector	59
Ion and Neutral Detector	64
Data Acquisition	67
V. ERROR ANALYSIS	70
Projectile Purity	70
Target Purity	71
Projectile Energy	71
Scattering Angle	71

TABLE OF CONTENTS (Continued)

Chapter		Page
V.	Beam Current.	72
	Target Density.	74
	Scattered H^+ and H^o Flux.	74
	Scattered H(2s) Flux.	76
	Geometrical Factor.	79
	Cascade Effects	80
	Summary	81
VI.	ELECTRON CAPTURE RESULTS AND DISCUSSION	85
	Measured Differential Cross Sections.	85
	Total Differential Cross Section.	88
	Electron Capture Probability.	90
	Metastable Content of the Neutral Flux.	97
VII.	DISSOCIATION RESULTS AND DISCUSSION	104
Appendices		
A.	DATA TABLES	113
B.	METASTABLE FLUX DETECTION EFFICIENCY.	129
	Definition of Metastable Detection Efficiency	129
	Calibration of the H(2s) Detection Efficiency	133
	Routine Monitor of Efficiency	136
	Energy Dependence of the Detection Efficiency	137
	H(2s) Signal Saturation	139
C.	EVALUATION OF THE SECONDARY EMISSION COEFFICIENT FOR H^o.	144
D.	MEASUREMENT OF THE TOTAL ELECTRON CAPTURE CROSS SECTION σ	151
E.	ALIGNMENT PROCEDURES.	154
F.	APPARATUS FUNCTION.	156
	Evaluation of $G(\theta)$.	156
	Finite Beam Considerations.	162
	Apparatus Resolution.	163
	Effects of Finite Resolution.	163

TABLE OF CONTENTS (Concluded)

Appendices Page

G. MEASUREMENT OF TOTAL CROSS SECTIONS FOR THE FORMATION OF H(2s) 165

REFERENCES 171

VITA 177

LIST OF TABLES

Data Table		Page
1.	Differential Cross Sections for Formation of H^+, H^o, and H(2s) by Charge Transfer	114
2.	Differential Cross Sections for Formation of H^+, H^o, and H(2s) by Dissociation.	119
3.	Differential Cross Sections for Formation of H^+, H^o, and H(2s) by Dissociation.	122
4.	Differential Cross Sections for Formation of H^+, H^o, and H(2s) by Dissociation.	123
5.	Fractional Content of Scattered Neutral Flux That Is in the 2s State (Charge Transfer Reaction)	124
6.	Total Cross Sections for Formation of H(2s)	126
7.	Total Cross Section for Formation of H^o	128

LIST OF ILLUSTRATIONS

Figure		Page
1.	Photograph of the Apparatus	46
2.	Cross Sectional View of the Apparatus	50
3.	Plane View of the Apparatus	51
4.	Detail of the Scattered Flux Collimator and Target Cell	55
5.	Metastable Flux Detector.	60
6.	Representative Count Rate Saturation Curves	62
7.	Faraday Cup Arrangement for Detection of Ions and Atoms	65
8.	Flow Charts for Data Handling	69
9.	Differential Cross Sections for the Scattering of H^+ by He.	86
10.	Total Differential Cross Sections for the Scattering of H^+ by He.	89
11.	Relation Between θE and Impact Parameter.	91
12.	Energy Dependence of P_o	92
13.	Energy Dependence of P_{2s}.	93
14.	Fractional H(2s) Content of the Scattered Neutral Flux.	99
15.	Potential Energy Curves for the HeH^+ Molecule	101
16.	Metastable Fractional Content of Scattered Neutral Flux for 6.25 keV Impact Energy	103
17.	Differential Cross Sections for the Scattering of H_2^+ by He	105

LIST OF ILLUSTRATIONS (Concluded)

Figure		Page
18.	Differential Cross Sections for the Scattering of H_2^+ by H_2	106
19.	Differential Cross Sections for the Scattering of H_3^+ by H_2	107
20.	Potential Energy Curves and Correlation Diagram for H_2^+	110
21.	H(2s) Detector Saturation Curves.	140
22.	Electric Field Dependence of the Metastable Transition Probability.	142
23.	Flow Chart for Measuring the Neutral Secondary Emission Coefficient.	146
24.	The Ratio of the Secondary Emission Coefficient for H^+ to the Secondary Emission Coefficient for H^o	148
25.	Energy Dependence of Secondary Emission Coefficient for H^+.	150
26.	Total Electron Capture Cross Section for Protons Incident on Helium.	153
27.	Scattered Flux Collimation Apertures.	158
28.	Geometrical Factor $\int_L \omega dx$	161

SUMMARY

The differential cross section for the formation of hydrogen atoms in the metastable 2s state has been measured for electron capture and dissociation collisions. The reactions were studied for impact energies between 4 and 20 keV and scattering angles between 0.5 and 3 degrees. For the electron capture reaction, the single projectile-target combination of H^+ and He was studied. For the dissociation work, collisions involving projectiles of H_2^+ and H_3^+ and targets of H_2 and He were studied.

The exceptionally long natural lifetime of metastable 2s level of hydrogen permitted atoms formed in this state to travel macroscopic distances with no appreciable loss due to natural decay. Flux scattered by an angle θ left the collision chamber and proceeded to the H(2s) detectors where a transverse electric field mixed the 2s level with the neighboring 2p levels. This had the effect of reducing the lifetime of the state and thus caused the atoms to emit a 1216 Angstrom Lyman-alpha photon. A fraction of these photons was then detected by an open-ended electron multiplier. Absolute values were assigned by normalizing a particular total cross section to a previously published absolute value.

For comparison with previous theoretical and experimental work on electron capture, the differential cross sections for the formation of H^+ and H^o were also measured. From the three cross sections were found the probability P_{2s} for the formation of H(2s), and the probability P_o,

for the formation of H^o. The fractional metastable content of the scattered neutral flux, P_{2s}/P_o, was also evaluated and compared with existing theory. Similar probabilities were formed for the dissociation processes and compared with the electron capture results.

All differential cross sections for electron capture were found to be smoothly varying functions of scattering angle. The data fit curves of the form $K\theta^{-n}$ where n ranged from 2.5 to 3.2, depending on the energy and the particular cross section. The probabilities P_{2s} and P_o were found to be fairly independent of scattering angle for angles greater than 0.7 degree but showed oscillatory structure as the impact energy was varied. The metastable fractional content of the scattered neutral flux, P_{2s}/P_o, was found to rise from a small value at low angles to a high value at large angles; the magnitude of the rise depended on the impact energy.

The dissociation data were also smoothly varying functions of angle. The differential cross sections for the dissociation of H_2^+ demonstrated a change in slope at scattering angles that could be correlated with known potential energy curves for the H_2^+ molecular ion if Frank-Conden excitations to anti-bonding states are assumed to be the mode of dissociation. The H_3^+ data showed no such breaks in the differential cross sections.

CHAPTER I

INTRODUCTION

After a period of some thirty years of relative inactivity, interest in the field of atomic collisions has recently undergone a phenomenal growth. This interest has been stimulated by the growing aerospace and space exploration industries and the recent large-scale effort to develop a practical thermonuclear fusion reactor. A knowledge of certain reaction rates and collision cross sections is of primal importance in understanding and controlling the propagation of communication signals through the upper regions of the earth's atmosphere. Although the problems of a controlled fusion reactor have not been solved, considerable study has been given to the heating of a magnetically confined plasma by injecting high-energy neutral atoms which, once past the magnetic barrier, are stripped of one or more electrons, thus becoming trapped in the plasma. The feasibility of such a process obviously depends on the magnitudes and energy dependence of the various cross sections for ionization and recombinations between the injected atoms and the constituents of the plasma.

Once experiments were under way for measuring cross sections of practical import, another factor arose which even further increased the interest in atomic collisions, at least from an academic point of view. Variations of cross sections with impact energy and scattering angle

began to show structures where none were thought to be. Systems of resonances comparable to those of optical spectroscopy emerged, and theorists immediately began to develop the theoretical structure necessary for understanding the new structures.

One of the most interesting structures uncovered was that of the energy dependence of the probability (P_o) for electron capture in violent large-scale collisions between protons and hydrogen atoms. In 1962 Lockwood and Everhart[1] published data showing that the probability was an oscillatory function of the energy whose peaks were almost evenly spaced when plotted versus the time of interaction (see Chapter VI). Ziemba, Lockwood, Morgan, and Everhart[2] found a similar but highly damped oscillatory structure for P_o when the hydrogen target was replaced with helium. Many attempts have been made to theoretically explain this damped oscillatory structure, but none have been fully successful. Since the interactions are known analytically (Coulomb potential), it might be expected that the collision problem could be solved exactly and accurate results obtained. Unfortunately, this is not the case for heavy-particle collisions in the energy range in which this structure was found (1 to 100 keV). The problem is one of practicality. Although the interaction Hamiltonian is known, the wave function for the system (projectile plus target) is unknown and thus must be represented by an expansion in some complete orthonormal basis set. When this is done, the solution of the Schrodinger wave equation reduces to the solution of an infinite set of coupled differential equations for the unknown coefficients. Even using modern computers, the exact solution of this system of equations is impractical,

and the theorist often resorts to experimental data for guidance in the selection of an appropriate finite basis set.

To provide additional information to theorists concerning the electron capture process between protons and helium as well as to provide practical cross sections for other experimentalists and engineers, a study of the reaction

$$H^+ + He \rightarrow H(2s) + [He^+] \qquad (1)$$

was undertaken. The brackets denote a lack of knowledge of the state of the post-collision target. This reaction is a subset of the net electron capture reaction measured by Everhart and co-workers and as such provides a finer test of theoretical approximations. The 2s state was chosen because it is metastable with a natural lifetime of ~ 0.14 sec, thus permitting flux in this state to traverse a macroscopic distance in the laboratory before detection and in so doing define the angle of scattering. Other bound hydrogenic states have lifetimes so short that they decay in the target region and thus become a scattered neutral in the ground state. Measuring angular distributions for electron capture into these states is possible (at least for the 2p state) using coincidence techniques.[3]

Specifically, the effective differential-in-angle cross section* for the formation of H(2s) has been measured for angles between 0.5 and 2 degrees and for impact energies between 4.0 and 20.0 keV.

In order to make detailed comparisons with existing theories and to

---

*Here "effective" means that population of the 2s level by cascade from higher levels contributes to the net measured cross section.

compare with previous experimental work, several additional cross sections were measured. Differential cross sections were measured for the formation of all neutrals,

$$H^+ + He \rightarrow H^o + [He^+] , \tag{2}$$

and for the quasi-elastic scattering of protons,

$$H^+ + He \rightarrow H^+ + [He] . \tag{3}$$

In addition, total cross sections were measured for reactions 1 and 2. From the measured differential cross sections, the probabilities for electron capture into the 2s state, P_{2s}, and for capture into any state, P_o, were formed and compared with existing data and theories. The total cross sections were compared with previous data as a check on the operation of the scattered flux detectors.

Several subsidiary experiments were performed using the molecular ions H_2^+ and H_3^+ as projectiles and helium and hydrogen as targets. The primary reason for performing these experiments was to ascertain the efficiency for production of metastable H(2s) flux via a dissociation process as compared with that of an electron-capture process. The same three differential cross sections were measured, and P_{2s} and P_o were formed. The reactions,

$$H_2^+ + He, H_2 \rightarrow H(2s) + [H^+ + He, H_2] \tag{4}$$

and

$$H_3^+ + H_2 \rightarrow H(2s) + [H_2^+ + H_2] , \tag{5}$$

where the brackets indicate a lack of knowledge of the details of the H(2s) formation process, are completely different in nature from the electron capture process and thus shed no light on the development of the charge exchange theory. However, from a practical point of view, it is quite illuminating to compare H(2s) yield by the two processes. In addition, it is hoped that these data will aid in the development of the theory for dissociative collisions.

Both types of experiments were performed with the same apparatus and in the same manner; the only difference was that, for electron capture, a proton beam was selected from the accelerator and, for dissociation, a beam of H_2^+ or H_3^+ was selected. The monoenergetic, well collimated ion beam was introduced into a chamber containing the gaseous target. Flux scattered out of the beam and into an angular range $\Delta\theta$ about θ was permitted to exit the chamber through a set of narrow vertical apertures and proceed to the detection region. Flux in the metastable 2s state was detected by applying an electric field which mixed the 2s level with the neighboring 2p levels, thus inducing the emission of a Lyman-alpha (L_α) photon. A fraction of these photons was subsequently detected by a continuous funneled electron multiplier.[4] Scattered H^+ and H^o were detected by monitoring the current of secondary electrons generated by bombardment of a metal plate. Calibration of the H(2s) detection efficiency was done by normalizing a measured total (in angle) cross section to a previously published absolute value (see Appendix B). The detection efficiencies for H^+ and H^o were measured directly, as described in Appendix C. Further details of the scattered flux detectors are presented in Chapter IV. The

operational definitions of a differential and a total cross section are presented in Chapter II. Previous experimental and theoretical work are discussed in Chapter III; Chapter IV is a description of the apparatus. An analysis of possible errors is presented in Chapter V. Chapters VI and VII contain the experimental results, interpretations, and comparisons for the electron-capture and dissociation experiments.

CHAPTER II

OPERATIONAL DEFINITION OF A DIFFERENTIAL CROSS SECTION

The terms "collision" and "collision cross section" are used in many fields of physics and have numerous definitions and connotations. Even in the specific field of atomic collisions, these terms are used somewhat loosely on the assumption that researchers in the field know from experience what is meant. Since this practice is often the source of some confusion to those without considerable experience in the field, this section is devoted to clearly defining the terminology used in this study and deriving the functional relationship between atomic or molecular cross sections, which are microscopic properties and not directly measurable, and macroscopic parameters measurable in the laboratory.

The occurrence of a collision may be defined by considering a system composed of a projectile moving parallel to the x axis of a rectangular coordinate system toward a target situated at the origin. For the present, both are considered to have bound excited states. The "state of the system" is defined by specifying the value of all measurable system variables. Consider a multi-dimensional space S, each of whose axes represents a system variable. The state of the system may be represented by a point in this space. A collision is said to have occurred if this point moves from its initial position to some new position as the projectile passes the vicinity of the target.*

*The axes in S space representing the coordinates of the projectile

Borrowing from chemical terminology, a collision may also be referred to as a reaction where the projectiles and the target are the reactants.

When one considers the numerous states to which both the projectile and target may be excited as well as angular deflection and other processes, it becomes clear why few investigators have studied the total collision process for any given set of reactants in a single experiment. Indeed, for impact energies of several kilovolts and above, when all excited states are energetically accessible, the task becomes overwhelming. What is usually done is to select a certain subset of all possible collisions, and the experimental apparatus is designed to detect these processes and ignore all others. This is equivalent to sampling only a subregion of S space after the collision. It is of utmost importance for experimental researchers to clearly delineate what processes were excluded as well as which were studied. This is because other researchers must include or exclude the same regions of S space if similar results are to be obtained. In addition, theoretical investigations of the collision process must also exclude the same reactions if agreement with experiment is to be expected.

In order to discuss the relative probability of various collision processes, the collision cross section is now introduced. For clarity and brevity the discussion will be restricted to processes of direct interest in this study. The fundamental process investigated was the

---

and the target are excluded from consideration; also, it is assumed that the target is incapable of capturing the projectile.

angular distribution of post-collision, fast hydrogen atoms formed in the metastable 2S state produced by the encounter of a fast projectile with a stationary target. In addition, the angular distributions of post-collision, fast protons and hydrogen atoms in any bound state were measured in order to present certain probabilities.

As long as the specific cause of the angular deflection, which is a matter of interpretation (see Chapter III), is overlooked, the probability and cross section for both the charge transfer and the dissociation process may be discussed in the same general terms.

Consider a region of space centered on the origin of a rectangular coordinate system where the target density is N_t cm^{-3}. The probability that, while the projectile moves a distance dx in this region, it will undergo a collision in which the post-collision products H(2s), H^o, or H^+ are scattered into a differential solid angle $d\omega$ centered on the polar angles θ, Φ is clearly proportional to N_t and dx. Thus

$$d^2P_i(\theta,\Phi) = d\sigma_i\ (\theta,\Phi)\ N_t\ dx\ , \qquad (6)$$

where the proportionality constant $d\sigma_i$ is called the differential scattering cross section for the production of the i^{th} post-collision species in the angular range $d\omega$. Notice that $d\sigma_i$ has the units of cm^2 in keeping with the common concept of a cross section representing an area. Since $d\sigma_i$ is related to the probability for scattering into an infinitesimal solid angle, a problem arises when one decides to measure it. No matter how small the resolution of the apparatus is made, the measured cross

section will not approach a limit independent of apparatus resolution. This is because the probability for scattering into an angular range $d\omega$ is, in fact, proportional to $d\omega$. Thus equation (6) may be written

$$d^2P_i(\theta,\Phi) = I_i(\theta,\Phi)\ d\omega\ N_t\ dx\ , \tag{7}$$

where

$$I_i(\theta,\Phi) = \left(\frac{d\sigma}{d\omega}\ (\theta,\Phi)\right)_i = \left(\frac{d\sigma}{d\omega}\right)_i\ . \tag{8}$$

The differential cross section per unit solid angle $\left(\frac{d\sigma}{d\omega}\right)_i$ does not depend on $d\omega$ and may thus be used to measure the probability of the collision of interest. Although this quantity is not strictly a cross section, it is often referred to as such in the literature. This practice, which is acceptable so long as the above definition is kept in mind, will be followed in this study as a matter of convenience.

In order to derive the relationship between $\left(\frac{d\sigma}{d\omega}\right)_i$, which is a microscopic property of two atomic or molecular reactants, and the macroscopic variables measured in the laboratory, consider a uniform beam of projectiles of volume density N_p cm^{-3} and speed v incident on the region of space containing the targets. Assume for the moment that the experimental apparatus is only capable of detecting post-collision flux scattered into an infinitesimal solid angle $d\omega$ from an infinitesimal volume $d^3\tau$ centered on the origin. The count rate (counts/sec) of the i^{th} species detector will be

$$d^4N_i(\theta,\Phi) = (D_e)_i\ N_p N_t v \left(\frac{d\sigma}{d\omega}\right)_i d\omega\ d^3\tau\ , \tag{9}$$

where $(D_e)_i$ is the detection efficiency of the i^{th} detector. Thus the quantity of interest $\left(\frac{d\sigma}{d\omega}\right)_i$ may be written

$$\left(\frac{d\sigma}{d\omega}\right)_i = \frac{d^4N_i(\theta,\Phi)}{(D_e)_i\ N_p N_t v\ d\omega\ d^3\tau}\ . \tag{10}$$

This is the basic relationship between measurable parameters (those on the right-hand side) and the microscopic collision property $\left(\frac{d\sigma}{d\omega}\right)_i$.

In practice, the experimental apparatus accepts flux scattered into a small but finite solid angle $\Delta\omega$ from a small but finite volume ΔV. The effect of the size of these variables on the measured value of $\left(\frac{d\sigma}{d\omega}\right)_i$ will now be discussed. A finite acceptance angle $\Delta\omega$ permits flux originating from an infinitesimal volume element $d^3\tau$ but scattered through a range of angles to be detected. The net count rate will be the integral of equation (9) over the permissible range of angles $\Delta\omega$. Thus

$$\overline{d^3N_i(\bar{\theta},\bar{\Phi})} = (D_e)_i\ N_p N_t v\ d^3\tau \int_{\Delta\omega} \left(\frac{d\sigma}{d\omega}\right)_i d\omega\ , \tag{11}$$

where $\overline{d^3N_i(\bar{\theta},\bar{\Phi})}$ is the net count rate from $d^3\tau$. Notice that θ and Φ are no longer precisely defined and have been replaced by effective scattering angles $\bar{\theta}$ and $\bar{\Phi}$, which are the average of each angle weighted according to the value of $\left(\frac{d\sigma}{d\omega}\right)_i$ at each value within $\Delta\omega$. If $\left(\overline{\frac{d\sigma}{d\omega}\ (\bar{\theta},\bar{\Phi})}\right)_i$ is the

average value of $\left(\frac{d\sigma}{d\omega}(\theta,\Phi)\right)_i$ over $\Delta\omega$, then equation (11) may be written

$$\overline{d^3N_i(\bar{\bar{\theta}},\bar{\bar{\Phi}})} = D_e N_p N_t v \left(\overline{\frac{d\sigma}{d\omega}(\bar{\bar{\theta}},\bar{\bar{\Phi}})}\right)_i \Delta\omega\, d^3\tau \ . \tag{12}$$

If the apparatus accepts flux scattered from a finite volume ΔV in the target region, the net count rate will be the integral of equation (12) over ΔV. Thus

$$\overline{\overline{N_i(\theta,\Phi)}} = D_e N_p N_t v \int_{\Delta V} \left(\overline{\frac{d\sigma}{d\omega}(\bar{\theta},\bar{\Phi})}\right)_i \Delta\omega\, d^3\tau \ , \tag{13}$$

where $\overline{\overline{N_i(\theta,\Phi)}}$ is the net count rate from ΔV. Notice again that another weighted average of θ and Φ has been indicated by the double bar. If $\left(\overline{\overline{\frac{d\sigma}{d\omega}(\theta,\Phi)}}\right)_i$ represents the weighted average of $\left(\overline{\frac{d\sigma}{d\omega}(\bar{\theta},\bar{\Phi})}\right)_i$ over ΔV, then equation (13) may be written

$$\overline{\overline{N_i(\bar{\bar{\theta}},\bar{\bar{\Phi}})}} = D_e N_p N_t v \left(\overline{\overline{\frac{d\sigma}{d\omega}(\bar{\bar{\theta}},\bar{\bar{\Phi}})}}\right)_i \int_{\Delta V} \Delta\omega\, d^3\tau \ . \tag{14}$$

In order to write equation (14), it was implicitly assumed that N_p is independent of position within ΔV. Strictly speaking, this cannot be true since each scattering collision removes a projectile from the beam. However, for small enough target densities N_t, the fraction of projectiles lost from the beam becomes small and N_p may be assumed to be constant. The range of target densities where this approximation is valid depends on the magnitude of the collision cross sections and the size of the

target region. An operational test is usually performed to ascertain this range of densities. The detector count rate is measured as a function of target density and, if a linear relationship is demonstrated, equation (14) may be employed. Operation within this linear range is often referred to as "operation under single-collision conditions."

The differential cross section measured by a practical apparatus with a finite resolution may be written

$$\left(\overline{\overline{\frac{d\sigma}{d\omega}\,(\bar{\bar{\theta}},\bar{\bar{\Phi}})}}\right)_i = \frac{\overline{\overline{N_i(\bar{\bar{\theta}},\bar{\bar{\Phi}})}}}{D_e N_p N_t v \int_{\Delta V} \Delta\omega \; d^3\tau} \tag{15}$$

The accuracy with which this quantity represents the true differential cross section is a function of how rapidly $\left(\frac{d\sigma}{d\omega}\right)_i$ varies with θ or Φ in relation to the sizes of $\Delta\omega$ and ΔV. If, for instance, the differential cross section were independent of θ, Φ, then the measured cross section would be identical to the true value. On the other hand, if $\left(\frac{d\sigma}{d\omega}\right)_i$ had many oscillations within $\Delta\omega$, the measured value would be an average over $\Delta\omega$ and would show no structure. Thus, one continually attempts to decrease $\Delta\omega$ and ΔV to improve accuracy; the limitation is usually one of obtaining a measurable count rate in the detector. An evaluation of the apparatus function $\int_{\Delta V} \Delta\omega \; d^3\tau$ and a discussion of resolution are located in Appendix F. For convenience the average bars of equation (15) will be dropped for the rest of the thesis. It should be kept in mind, however,

that all measured flux and quantities derived from them are in reality averaged over $\Delta\omega$ and ΔV. Thus equation (15) may be written

$$\left(\frac{d\sigma}{d\omega}\ (\theta,\Phi)\right)_i = \frac{N_i(\theta,\Phi)}{D_e N_p N_t v\ G(\theta,\Phi)}\ , \tag{16}$$

where

$$G(\theta,\Phi) = \int_{\Delta V} \Delta\omega\ d^3\tau\ . \tag{17}$$

For the present work, neither the projectile nor the target is polarized, and the differential cross section is not expected to exhibit a Φ dependence. It will be assumed that $\left(\frac{d\sigma}{d\omega}\right)_i$ is independent of Φ, so equation (16) may be written

$$\left(\frac{d\sigma}{d\omega}\ (\theta)\right)_i = \frac{N_i(\theta)}{(D_e)_i N_p N_t v\ G(\theta)}\ . \tag{18}$$

In general, the angle notation will also be dropped, and the differential cross section per unit solid angle for the i^{th} reaction will simply be referred to as $(d\sigma/d\omega)_i$.

It will be shown in Appendix F that, for the scattered flux collimation system used in this experiment, the apparatus function $G(\theta)$ may, with negligible error, be written

$$G(\theta) = A \int_{L(\theta)} \Delta\omega\ dx\ , \tag{19}$$

where A is the cross-sectional area of the projectile beam and $L(\theta)$ is

the portion of the x axis where $\Delta\omega$ is not zero. Using equation (19), the operational definition for the differential cross section for the i^{th} reaction may be written

$$\left(\frac{d\sigma}{d\omega}\right)_i = \frac{N_i(\theta)|e|}{(D_e)_i N_t I_p \int_{L(\theta)} \Delta\omega \, dx} , \tag{20}$$

where $|e|$ is the magnitude of the electronic charge and I_p is the current of ionic projectiles. Notice that, since $N_i(\theta)$ has units of sec^{-1}, the numerator of equation (20) has units of current, and the denominator has units of current $\cdot$ Sr/cm^2 so that the differential cross section has the expected units of cm^2/Sr.

Several subsidiary experiments were performed for detector calibration purposes. These experiments measured the "total" cross section for the i^{th} reaction. In this study, "total cross section" will mean the cross section for formation of the i^{th} post-collision species independent of its angular deflection. The relationship between measured quantities and the total cross section may be derived in a fashion similar to that used for the differential cross section. Consider a single projectile incident on a volume where the target density is again N_t cm^{-3}. The probability that the projectile undergoes to i^{th} reaction (now ignoring angular deflection) while moving a distance dx in the volume is again proportional to N_t and dx. Thus

$$dP_i = \sigma_i N_t \, dx , \tag{21}$$

where σ_i is the total (all angles) cross section for the i^{th} reaction.

If a beam of projectiles of volume density N_p cm^{-3}, speed v, and cross-sectional area A is incident on this volume of targets, the count rate of the i^{th} species detector due to collisions in dx, dN_i (counts/sec) will be

$$dN_i = (D_e)_i \, N_p \, A \, v dP_i = (D_e)_i \, [N_p N_t v A] \, \sigma_i \, dx \, . \tag{22}$$

If N_t is small enough so that the depletion of N_p may be ignored, equation (22) may be integrated to give

$$N_i = D_e N_p v A N_t \, \sigma_i \, L \, , \tag{23}$$

where L is the length of the target region. As was the case for differential cross section, the validity of this approximation may be checked by showing a linear relationship between N_i and N_t. Thus

$$\sigma_i = \frac{N_i}{D_e N_p v A N_t L} \, . \tag{24}$$

One additional test must be performed so that equation (22) represents the true value of σ_i. It must be shown that the detector does not exclude any appreciable fraction of the post-collision flux due to angular deflection. This may be done either by increasing the size of the scattered flux apertures until there is no further change in detector count rate or by measuring the scattered flux angular distribution and setting the aperture size accordingly. Since the apparatus was designed for this

type of measurement, the latter method was used.

Finally, a relation between the total cross section for production of the i^{th} species and the differential cross section (per unit solid angle) for the i^{th} species may be derived by considering equations (9) and (22). Integrating equation (9) over all scattering angles and over the area of the beam, one obtains the same detector count rate as presented in equation (22). Thus,

$$\int_A \int_{\theta,\Phi} d^4 N_i(\theta,\Phi) = D_e N_p N_t v A \int_\theta \left(\frac{d\sigma}{d\omega}(\theta,\Phi)\right)_i d\omega dx = D_e N_p N_t v A \sigma_i dx \ . \quad (25)$$

Solving for σ_i, one finds

$$\sigma_i = \int_\theta \int_\Phi \left(\frac{d\sigma}{d\omega}(\theta,\Phi)\right)_i d\omega \ . \quad (26)$$

If the differential cross section can be assumed to be independent of Φ, equation (26) may be written

$$\sigma_i = 2\pi \int_\theta \left(\frac{d\sigma}{d\omega}(\theta)\right)_i \sin\theta \, d\theta \ . \quad (27)$$

CHAPTER III

PREVIOUS WORK — EXPERIMENTAL AND THEORETICAL

The two collision processes studied in this research (electron capture and dissociation) have been the subject of considerable experimental and theoretical research. The large number and broad scope of these investigations make it impractical to present a general and comprehensive review of all previous work. For this reason, the discussion presented in this chapter will be limited to those works which have direct bearing on either the presentation or the interpretation of the data presented in Chapters VI and VII. The first two sections of this chapter are reviews of the experimental and theoretical work on electron capture; the last section deals with dissociation processes.

Previous Experimental Work for Electron Capture

Since 1952 the total cross section, σ_o, for the electron capture process $H^+ + He \rightarrow H^o + [He^+]$ has been measured by several investigators for impact energies between 4 and 20 keV.

Techniques used to measure this cross section are reviewed by Allison et al.,[5] where additional references may be found to work prior to 1962. Stedeford and Hasted[6] (1955) measured the absolute value of σ_o for impact energies between 0.10 and 40 keV by monitoring the net slow ion current in the collision region. A more recent investigation (1966) using the same principle as Stedeford et al.[6] has been conducted by DeHeer

et al.[7] for impact energies between 10 and 140 keV. Attention was given to reduction of systematic errors due to mercury diffusion effects in the McLeod pressure gauge. Stier and Barnett[8] (1956) employed two methods to measure σ_o in the energy range 4 to 200 keV. The first method was based on monitoring the decrease in beam current as target pressure was increased. Care was exercised to account for scattering effects. The second method was to measure the fraction of the beam in each charge state (+, 0, -) after passing through a "thick" target. These fractions were then related to the σ_o cross section. Excellent agreement between data measured both ways was found. Finally, Williams and Dunbar[9] (1966) measured the energy dependence of σ_o between 2 and 50 keV and normalized to Stier et al.[8] at 10 keV. These investigations were chosen as representative of the various methods of measuring σ_o.

The total cross section, σ_{2s}, for the reaction $H^+ + He \rightarrow H(2s) + [He^+]$ has been measured by Colli et al.[10] (1962), Jaecks et al.[11] (1965), Dose[12] (1966), Ryding et al.[13] (1966), Andreev et al.[14](1966), and Fitzwilson et al.[15] (1971).

Colli et al.[10] measured the relative value of σ_{2s} for impact energies between 7 and 40 keV. Absolute values were assigned by normalizing the experimental data to the Born approximation at 40 keV. No mass analysis was performed on the ion beam which was produced by a Thoneman source. After exiting the target region, H(2s) flux was electric field quenched, and the emitted radiation was detected by means of a vacuum u-v photomultiplier.

Jaecks et al.[11] measured the absolute value of σ_{2s} for impact energies between 1.5 and 23 keV. A mass-analyzed proton beam was introduced into a collision chamber containing the target gas. An oxygen-filtered, helium-iodine vapor filled photon detector viewed the collision region and registered photons resulting from H(2p) emission. A spatially varying electric field was then used to induce the H(2s) to decay in the target cell. The difference in detected signal was related to σ_{2s}. Absolute values were assigned by relating the 2p electron-capture cross section to the reaction $e^- + H_2 \rightarrow$ countable ultraviolet, whose magnitude was based on measurements of the reaction $e^- + H \rightarrow$ Lyman-alpha.[16] The reproducibility was ± 5 percent and the estimated possible absolute error was 45 percent. This estimate of possible absolute error is likely to be too low because the basis for normalization [$e^- + H \rightarrow$ Lyman-alpha] was in turn normalized to theory and was not confirmed experimentally; moreover, there is now known to be some error involved in the use of $e^- + H_2 \rightarrow$ countable ultraviolet as a transfer standard.

Dose[12] measured σ_{2s} on a relative basis for impact energies between 3 and 71 keV. The metastable 2s flux was quenched in the target region by an axial electric field. Emitted radiation was detected by a helium-iodine detector similar to that used by Jaecks except that the oxygen filter was omitted to eliminate the possibility of signal reduction due to Doppler shifting the Lyman-alpha photon out of the narrow passband.

The work of Ryding et al.[13] was concerned with the energy range 40 to 200 keV, which is above that used in the present work; thus, no direct comparison to Ryding's work is possible.

Andreev et al.[14] measured the absolute value of σ_{2s} for impact energies between 10 and 40 keV. Target gases of helium, neon, argon, krypton, and xenon were used. Since all of the 2s data presented in this study were normalized to Andreev's data for an argon target (see Appendix B), this work will be discussed in some detail. A beam of monoenergetic, mass-analyzed protons was introduced into a chamber containing the target gas and a parallel plate capacitator. Target gas pressures were measured with a McLeod gauge. A vacuum monochromator, which viewed the target region between the capacitator plates, was used to select Lyman-alpha radiation and direct it to a sodium salicylate coated photomultiplier for detection. The difference in signal when the quench field was on and then off was related to the cross section for electron capture into the 2s state. The signal with the quench field off was related to the σ_{2s} cross section. The use of a high resolution monochromator permitted Lyman-alpha radiation to be separated from nearby radiation from excited target atoms. A two-step procedure was used to assign absolute values to all cross sections. First, the signal arising from 2p electron capture was measured at 16 keV impact energy for all target gases. This allowed the absolute calibration of the detection system to be done at only one energy. The monochromator was then removed, and an absolute measurement of the σ_{2p} cross section for the reaction $H^+ + Ne \rightarrow H(2p) + [Ne^+]$ was made at an impact energy of 16 keV. A nitric oxide (NO) photo-ionization chamber with a lithium fluoride (LiF) window[17] was used to monitor the proton flux. The photo-ionization current was a measure of the L_α intensity only if there was no emission from the target in the spectral range between the

LiF cutoff (1050 Å) and the photo-ionization threshold of the NO molecule (1346 Å). Measurements with the monochromator showed that, for the reaction $H^+ + Ne$, there were no target excitation lines in this range. The 2s cross sections were then related to this absolute measurement via the measured ratios σ_{2s}/σ_{2p} taken with and without the quench field. The estimated possible error for the absolute magnitude of the 2s data was ± 20 percent with a ± 5 percent reproducibility. Additional discussion of Andreev's work is presented in Appendix B, where the normalization procedure used in the present work is described, and in Chapter V, where errors are discussed.

The work of Fitzwilson et al.[15] is presented in its entirety in Appendix G. It should be noted that these data were normalized to a slightly different cross section from that used in this study (see Appendix B).

The angle and energy dependence of the electron-capture collision process $H^+ + He \rightarrow H^o + [He^+]$ was first investigated by Ziemba, Lockwood, Morgan, and Everhart[2] in 1960. These measurements were later extended and refined by Helbig and Everhart[18] in 1964. The only other published measurement of this reaction was by Jaecks, Crandall, and McKnight[3] in 1970. All three groups of investigators presented data in the form of P_o, the ratio of scattered neutral flux to total scattered flux. Since this ratio does not depend on beam intensity or target gas pressure (as long as single collision conditions prevail), the measuring techniques for these quantities need not be reviewed. However, in the case of Jaecks et al.,[3] certain unpublished absolute cross sections will be

reported in this study, and a review of the measuring techniques employed will be presented.

The work of Ziemba et al.[2] presents measurements of P_o for a fixed laboratory scattering angle of five degrees and for impact energies between 1 and 200 keV. When plotted as a function of reciprocal impact velocity, P_o exhibited the strongly damped oscillatory structure which has since received extensive theoretical attention. The angular resolution of the apparatus (defined here as the maximum range in angles acceptable when the apparatus was nominally set to five degrees) was approximately 0.8 degree. Ziemba used an open-ended electron multiplier to monitor the scattered flux of protons and hydrogen atoms. Since only ratios of flux were reported, absolute calibration of the detector was unnecessary. No direct comparison was made of the relative detection efficiency for ions and neutrals although several indirect arguments were presented which indicated that the efficiency was charge independent. In 1964 Helbig et al.[18] extended those measurements to include angle dependence of P_o for angles between 0.5 and 4 degrees. The equipment and procedure used were similar to those used in the original work by Ziemba. The results of Helbig et al.[18] are presented in Chapter VI for comparison with P_o measured in the present work.

The work of Jaecks et al.[3] is a portion of a thesis by Crandall[19] concerning the large scattering-angle, electron-capture process for protons incident on helium and argon. A full description of the apparatus and measurement technique is presented in that thesis. Since data from Crandall's thesis will be quoted frequently in Chapter VI, the relevant

aspects of his experiment will be reviewed here. A beam of mass-analyzed protons was introduced into a region containing the target gas through the 0.10 cm diameter collimating apertures. Scattered flux was collimated by a two-slit arrangement similar to that used in the present work. The first slit was 0.0513 cm wide and 1.63 cm from the center of the collision cell. The second aperture was 0.1010 cm wide, 0.3727 cm high, and 14.29 cm from the collision chamber. Thus, the resolution (as previously defined) was ~ 0.8 degree. Beam current was monitored by a current integrator while data were being taken. Target gas pressure was monitored with an ionization gauge, which was in turn calibrated against a McLeod gauge. Scattered ions and neutrals were detected by an open-ended electron multiplier. The detection efficiency for neutrals was measured in two ways. First, a coincidence technique based on work by Christofori et al.[20] was used to relate the emission of a quenched Lyman-alpha photon with the existence of a particular neutral atom. The efficiency was found to vary from 10 percent at 4 keV to 14 percent at 20 keV. The second technique employed was based on comparing the net scattered flux (protons plus atoms) with that predicted by classical calculations by Dose.[21] The two methods yielded similar results for the neutral efficiency. No direct measurement of detector efficiency for protons was carried out.

The only previous measurements of the differential cross section for electron capture into the 2s state via the reaction $H^+ + He \rightarrow H(2s) + [He^+]$ are by Dose[22] (1966) and Crandall.[19]* Dose[22] presents the energy

*Part of the data contained in Crandall's thesis has been published (see references 3 and 23).

dependence of the probability for electron capture into the 2s state, P_{2s} (2s flux divided by net scattered flux), for the fixed scattering angle of 2.2 degrees. Impact energies between 4.5 keV and 60 keV were used. Few details are available concerning the work of Dose. Neither the type photon detector used nor the method used to monitor the net scattered flux (which is necessary to form the probability P_{2s}) was described. Dose states that the efficiency of the photon detector was evaluated by normalizing to the work of Colli et al.[10] It is now known that the work of Colli is inconsistent with recent measurements.[24] For these reasons, the absolute value of P_{2s} as presented by Dose must be considered suspect. The variation of P_{2s} with impact energy is quite possibly accurate and is presented in Chapter VI for comparison purposes.

The work of Crandall is more extensive in that both the angular (1 to 7 degrees) and energy (3 to 20 keV) dependence of P_{2s} was studied. The photon detector was a solar-blind photomultiplier fitted with an LiF window. Detection efficiency was calibrated by normalization to a previously published total 2s electron-capture cross section.

Previous Theoretical Work for Electron Capture

Electron capture is one of the most difficult atomic collision processes to describe mathematically. Not only does it exhibit the difficulties of the many body problem, but the nature of the process discourages the use of the highly developed approximations of electron-atom collisions[25] and precludes the use of many of the methods employed for atom-atom excitation collisions.[26] The approximation methods which have

proven most successful for describing the capture process may be classified into three major groups according to the magnitude of the projectile velocity. For very fast collisions (proton energy > 100 keV), the Born series, the impulse approximation, and the continuum distorted wave method have been used with considerable success in explaining the energy dependence and magnitude of the total capture cross section.* Since these methods are applicable to energies outside the scope of the present work, they will not be discussed here. Details of these calculations may be found in reviews by Bransden,[27] McDowell,[28] and Bates,[29] and papers by Salin[30] (continuum distorted wave approximation) and Coleman[31] (impulse approximation). For intermediate velocities (proton energy between 5 and 50 keV), one of the most successful approaches has been a coupled-state, impact-parameter calculation using an atomic orbital expansion. Since much of the data presented in Chapter VI will be compared with theoretical predictions based on this method, the coupled-state treatment will be discussed below. For slow collisions, the system begins to assume the characteristics of a temporary or quasi-molecule. Several treatments based on this concept are available. Two methods of direct interest here are the coupled-state impact parameter formalism using a molecular orbital expansion and a semi-empirical method that is quite useful in qualitative discussion of the capture process.

The essence of the coupled-state impact parameter treatment is that the nuclei follow classical orbits throughout the collision, the trajectory being defined by the interatomic forces. To calculate the cap-

*There is still some question concerning the exact high energy dependence of the total cross section (see reference 27).

ture probability, the further assumption is usually made that the projectile suffers no angular deflection at all during the collision and traverses a straight line trajectory. The probability for electron capture is then calculated as a function of impact parameter. The total cross section may then be obtained by integration over all impact parameters. Differential cross sections require the assessment of a deflection function via classical scattering theory.

A discussion is presented below of classical scattering theories that are applicable to the subject of this study; comments are also made on the coupled-state impact parameter method and also on the semi-empirical quasi-molecule approach. Additional information on the many theoretical methods developed for the electron capture process may be found in references 28-30, 32, and 33.

Classical Scattering of Heavy Particles

Mott and Massey[34] have specified the criteria which must be satisfied for classical scattering theory to adequately describe the angular deflection of an atomic projectile. Consider a projectile of mass m and velocity v incident on a scattering potential of order D and extent a. For a classical treatment to be valid, the following two conditions must hold: (a) the deBroglie wavelength of the projectile must be small compared to a and (b) the deflection of the projectile must be well defined within the limitations of the uncertainty principle.

The first condition requires that $a \gg h/mv$. Using the screening length of the screened Coulomb potential (discussed later) for a, this inequality may be shown to be valid for all impact energies used in the

present study.

The second condition requires that, if Δp is the transverse momentum transfer in the collision, then $a\Delta p \gg h$. Dividing by the projectile momentum p and noting that, for small scattering angles $\theta \approx \Delta p/p$, this criterion may be written $\theta \gg h/ap$. The ratio h/ap is essentially the ratio of the projectile deBroglie wavelength to the dimensions of the scattering potential. Again using the screening length for the screened Coulomb potential, the minimum angle of scattering which may be described classically is ≈ 0.1 degree for 4 keV protons on helium. This angle is smaller for more energetic projectiles. No data are presented in this study for angles smaller than this limit.

Thus the angular deflection of protons by helium targets may be described classically. However, the actual calculation of the classical deflection functions is difficult because of a lack of knowledge of the exact scattering potential.

In the center-of-mass reference frame, the classical description of the two-body collision where only radial forces are assumed to exist may be formulated in the form of a single projectile of reduced mass scattering from a fixed center.[35-37] In this coordinate system the scattering angle θ_{cm} corresponding to a given impact parameter b is given by

$$\theta_{cm} = \pi - 2 \int_{r_o}^{\infty} \frac{dr}{r \sqrt{\frac{r^2}{b^2} - 1 - \frac{r^2 V(r)}{b\, E}}} , \qquad (28)$$

where E is the center-of-mass kinetic energy before and after the collision (assumption here is that collision is elastic), r_o is the distance

of closest approach of the colliding atoms (largest positive root of the denominator), and V(r) is the interaction potential between the atoms. The inelastic effect of the 11- or 21-eV energy defect associated with the electron capture processes is unimportant since the relative kinetic energy was always greater than 3 keV. For a given energy E and functional form V(r), equation (28) may be thought of as providing a one-to-one correspondence between impact parameter b and scattering angle.

The purpose of any impact parameter calculation is to calculate the probability $P_i(b)$ that a collision at an impact parameter between b and b + db gives rise to the formation of the state i. The true differential cross section, $d\sigma_i$ (defined by equation (6), is simply given by

$$d\sigma_i = 2\pi P_i(b)\ b\ d\ b \tag{29}$$

Theoretical predictions may be tested by comparing a measurement of differential cross section at some angle θ with the theoretical predictions at a corresponding impact parameter b, the relationship between b and θ being derived from equation (28). A less sensitive test is to compare the measured value of a total cross section, σ_i, with the value calculated by integrating $d\sigma_i$ over all impact parameters:

$$\sigma_i = 2\pi \int_0^\infty P_i(b)\ b\ d\ b\ . \tag{30}$$

Exact specification of the potential function V(r) is somewhat difficult for an electron capture collision, since the prior collision

interaction potential usually differs from the post-collision potential. The result of this jump from one potential curve to another is that there is no one-to-one correspondence between impact parameter and scattering angle. This effect becomes more important as the impact energy is reduced [18] and provides a limitation on the usefulness of the classical interpretation of differential scattering

An approximation to V(r) which is frequently employed is the screened Coulomb potential,

$$V(r) = \left(\frac{Z_1 Z_2 e^2}{r}\right) e^{-r/a} , \qquad (31)$$

where eZ_1 and eZ_2 are the nuclear charges of the target and projectile and a is the parameter which measures the effectiveness of the electron screening. Bohr[38] has discussed this potential in some detail and has suggested the expression

$$a = \frac{a_0}{[Z_1^{2/3} + Z_2^{2/3}]^{1/2}} \qquad (32)$$

for the screening length. Here a_0 is 0.53×10^{-8} cm, the radius of the first orbit in hydrogen. Equation (28) has been numerically calculated for this potential by Everhart et al.[39] and Bingham.[40]

The screened Coulomb potential does not allow for any shell structure in either atom. Smith[41] has proposed a modified form of equation (29) in which the potential of the target atom is taken to be $V(r) = \frac{e}{r}\sum_{\nu} \alpha_\nu e^{-r/a}$, where α_ν = 2,8,8 for K,L, and M shells, respectively, and

$\alpha_\nu = a_o(I_H/I_\nu)^{1/2}$, I being the ionization potential of hydrogen and I_ν the closed shell ionization potential of the K,L, and M shell of target atom. Dose[21] has applied this potential to the scattering of protons by helium.

F. W. Bingham (private communication) has recently devised a "static potential" that takes into account all interactions between electrons and nuclei at all points during the collision process. By following these interactions at all internuclear separations, he calculates the cross sections for scattering the projectile.

If the scattering angle θ is small and if the impact energy E is much greater than the interaction potential V(r), Kennard[42] showed that equation (28) for the center-of-mass scattering angle may be approximated to a high degree of accuracy by

$$\theta_{cm}E_{cm} \cong r_o \int_{r_o}^{\infty} \frac{[V(r_o) - V(r)]}{(r^2 - r_o^2)^{3/2}} rdr \ . \qquad (33)$$

Thus the product θ E is function only of the distance of closest approach r_o. Notice that the value of θ E will be the same in the center-of-mass or laboratory coordinates (for small angle scattering). Smith et al.[43] have thoroughly investigated this expansion and have discussed its applicability. The usefulness of this result lies in the fact that differential data prescribed for a constant θ E product represent a study of the reaction at a fixed distance of closest approach and, to a good approximation, a fixed impact parameter.

The evaluation of equation (33) depends on the particular functional

form of the interaction potential V(r). Two basic limitations exist on the usefulness of equation (33) in addition to the quantum limitation discussed earlier. The first is the validity with which V(r) represents the two interaction potential, and the second is the problem mentioned earlier concerning the fact that, for the electron capture reaction, the collision occurs partly on one potential curve and partly on another.

In Chapter VI cross sections for scattering projectiles that have been calculated using the potentials discussed above will be compared with the results of the present experiments.

Coupled-State Impact Parameter Method

In the coupled-state impact parameter method, the projectile is assumed to move on a classical trajectory, and the total electronic wave function, ψ, is expanded in a linear combination of atomic eigenfunctions for the target and projectile, ψ_i. (The molecular expansion follows a similar development.) Thus

$$\psi_i = \sum_i a_i(t)\ \psi_i(\underline{r}) \ , \tag{34}$$

where $\underline{r}$ represents the several system coordinates and t = 0 when the projectile is at its distance of closest approach. The motion of the projectiles, which is usually assumed to be rectilinear, introduces a time-dependent perturbation among the various basis states ψ_i causing transitions to occur. If the total wave function is required to satisfy the time-dependent Schrodinger wave equation with the boundary conditions $a_1(-\infty) = 1$ and $a_{i \neq 1}(-\infty) = 0$, a system of coupled differential equations

for the coefficients, $a_i(t)$ results. The probability for electron capture into the i^{th} state is given by

$$P_i(b) = |a_i(t = +\infty, b)|^2 \quad . \tag{35}$$

The primary difficulty in using the coupled-state method is in the selection of a sufficient number of basis functions to adequately represent the collision. Since the solution of the system of coupled differential equations becomes quite tedious as the number of basis functions is increased above two or three, a judicious choice of basis functions is required. It has been shown that the results of the coupled-state impact parameter method is reasonably insensitive to the precise form chosen for the target helium wave function.[44-46] The number of hydrogenic wave functions needed to describe the electron capture process is a question which has not yet been answered.

Green et al.[44] performed a "two-state" calculation for the reaction $H^+ + He \rightarrow H(1s) + He^+$ in which the total wave function was expanded as a linear combination of the states $[H^+, He(1s^2)]$ and $[H(1s), He^+(1s)]$. These results are essentially the same as those in a similar but more comprehensive four-state calculation by Sin Fai Lam.

Sin Fai Lam[47] used a four-state traveling atomic orbital expansion (1s, 2s, $2p_x$, and $2p_z$) to ascertain the effects of allowing the n = 2 states to participate in the capture process. Calculations of the following cross sections were presented: (a) total cross section for electron capture into the 1s, 2s, and 2p states and (b) impact parameter and energy

dependence of the probability for electron capture into the 1s, 2s, and 2p states. This calculation is the only one known to the author which presents $P_{2s}(b,v)$ and thus provides the only theoretical comparison to the present differential 2s data.

Colegrave and Stephens[46] used a two-state molecular orbital expansion (sometimes referred to as the perturbed stationary state method) to calculate $P_{1s}(b)$ and the total capture cross section for the 1s state. The nature of their calculations was that it should become a better approximation as the impact energy was reduced below 10 keV. Good agreement was found with measured total capture cross sections between 1 and 16 keV. The calculated P_o curve is compared with the results of Ziemba et al.[2] and the present work in Chapter VI.

The calculations described above are direct electron capture, i.e., electron transfer from the helium $1s^2$ state directly into the state of interest (1s, 2s, or 2p). Polvektov and Presnyakov[48] have formulated a theory which describes capture into a state via an intermediate or virtual state. This two-step process is of most importance when the cross section for direct capture is very small while the cross section for capture into the intermediate state is large. In the case of capture into the 2s state, this intermediate state was taken to be the 1s ground state. It was found that the cross section for electron capture into the excited state, σ_{2s}, may be written

$$\sigma_{2s} = \sigma_{2s} + \sigma_{1s,1s \rightarrow 2s} . \qquad (36)$$

Here $\sigma_{2s} = 2\pi \int_0^\infty P_{2s}\ b\ d\ b$ and $\sigma_{1s,1s \rightarrow 2s} = \frac{\pi}{2} \int_0^\infty P_{1s}P_{1s \rightarrow 2s}\ b\ d\ b$

where P_{2s} is the probability for direct capture into the excited state, P_{1s} is the probability for direct capture into the ground state, and $P_{1s \rightarrow 2s}$ is the probability of excitation from the ground to the excited state.

The cross section for electron capture via an intermediate state, $\sigma_{1s,1s \rightarrow 2s}$, was not explicitly evaluated by Polvektov et al.[48] but it is thought to be proportional to the cross section for capture into the ground state, σ_{1s}.

Molecular Model and Semi-Empirical Formulae

The oscillatory nature of the large angle P_o curves of Lockwood et al.[1] and Helbig et al.[18] suggests a damped resonance structure. Lichten[49,50] has discussed a particular molecular model which provides a qualitative picture of the origin of these oscillations. The original development[49] was for the resonant $H^+ + H$ collision, but the same principle has been applied to the quasi-resonant $H^+ + He$ collision.[50] Before the projectile enters the neighborhood of the target, the system wave function is clearly best represented by atomic orbitals in which the "active" electron is bound to the target. During the collision, however, the system takes on the characteristics of a molecule. Two stationary states, split by an energy $[V_1(r) - V_2(r)]^*$ exist for the molecular ion: (1) a symmetric sum of the two atomic orbitals which represent the electron residing on the target and the projectile, respectively, and (2) an anti-

*Here $V_1(r)$ and $V_2(r)$ are the molecular system energy for states 1 and 2.

symmetric combination of the two atomic orbitals. The system wave equation is not a stationary state during the collision because its initial boundary condition (i.e., the electron attached to the target) was not a molecular eigenfunction. Thus, during the collision, the total wave function oscillates between the two limiting states (1) and (2) with an exchange frequency $[V_1(r) - V_2(r)]/h$. If one can assign a distance R_o to be the internuclear separation where the system is best described as a quasi-molecule (R_o is obviously not well defined), then it is clear that the time of interaction is a function of reciprocal impact velocity. The number of exchange oscillations the system can make depends on the frequency $[V_1(r) - V_2(r)]/h$ and the time of interaction. If the system makes 1/2, 3/2, etc. oscillations, the electron will be attached to the projectile, and electron capture will have occurred. An integral number of oscillations would leave the target in its original state and the probability of electron capture would be low.

Lockwood and Everhard[1] employed the above concepts in the interpretations of the oscillations in P_o for the reactions $H^+ + H^o \rightarrow H^o + H^+$, $He^+ + He \rightarrow He + He^+$, and $H^+ + He \rightarrow H^o + He^+$. Assuming that the time of interaction could be represented by $2R_o/v$, they derived the following expression:

$$h/V = 2R_o\,[1/v_1 - 1/v_3]\,, \tag{37}$$

where v_1 and v_3 are the impact velocities corresponding to two adjacent valleys or peaks and $V = V_1(R) - V_2(R)$. This equation was generalized and written as

$$\langle VR \rangle_n = \frac{h}{(1/v_{n+2}) - (1/v_n)} \quad , \tag{38}$$

where the brackets indicate an effective value for the product of energy and length. Neither quantity is well defined since the collision begins and ends gradually and the energy difference is a function of internuclear separation. It was suggested that the effective value of $\langle VR \rangle$ might be calculated using

$$\langle VR \rangle = \int_{-R_o}^{R_o} [V_1(r) - V_2(r)]\, dr \quad , \tag{39}$$

where dr is an element of path length along the trajectory followed by the projectile and $V_1(r) - V_2(r)$ is the energy separation between the two molecular states of concern. The above derivation is certainly not rigorous, but it is quite interesting that the calculated values of $\langle VR \rangle$ using reasonable values of R_o and adiabatic molecular potential curves compare quite well with that evaluated by fitting equation (38) to the experimental data.[1]

Lockwood et al.[1] suggested that an empirical formula which correctly fits the experimental data is

$$P_o = K_1(1/v) + K_2(1/v) \sin^2 \left[\left(\frac{\pi \langle VR \rangle}{vh}\right) - \beta\right] \tag{40}$$

where K_1 and K_2 are slowly varying functions of reciprocal velocity. The constants $\langle VR \rangle$ and β were determined to be 84.6 ± 1 eV-Å and $(0.26 \pm 0.02)\pi$ by comparison of equations (38) and (40) with experiment.

It is clear that, for a molecular interpretation of a collision

process, knowledge of the molecular energy levels as a function of internuclear separation is necessary. Michels[51] has performed an adiabatic calculation of the lower levels for the HeH^+ molecule; his results are included in Chapter VI.

Previous Dissociation Work — Experimental and Theoretical

The review of previous dissociation work will be quite brief in comparison with the very extensive work which has been done in this field. Only experimental and theoretical work directly comparable with the present results will be cited. Additional references to previous dissociation work will be found in papers by Durup et al.[52] and Green and Peek.[53]

No previous experimental work has been found concerning the measurement of the differential cross section for the formation of metastable H(2s) atoms via the dissociation reactions $H_2^+ + H_2$, $H_2^+ + He$, or $H_3^+ + H$.

The only quantitative information published on the angular distribution of H_2^+ dissociation fragments is that of McClure,[54] Sweetman,[55] and Gibson et al.[56] for a target of H_2; Damadaran[57] for targets of H_2, N_2, and argon; Fedorenko et al.[58] for a target of argon; Barnett et al.[59] for an H_2O target; and Gibson and Los[60] for targets of H_2 and He.

Only McClure[54] and Gibson and Los[60] present data in a form directly comparable with the present work. Gibson and Los[60] include a single relative angular scan of protons produced by dissociation of 10 keV H_2^+ incident on an H_2 target. This scan is normalized to the work of McClure[54] and agrees well in angular dependence. McClure[54] presents angular scans of H^+ and H^0 produced by the dissociation of H_2^+ incident on H_2. Projec-

tile energies between 5 and 80 keV were used. A mass sensitive counter was used so that scattered H^o and H_2 could be distinguished. Angular resolution was stated to vary linearly from 0.18 to 0.31 degree when the apparatus was moved from a scattering angle of 0 to 2.58 degrees. Absolute values were determined by integrating the relative differential cross sections and fitting the integrals to the total dissociation cross sections presented in a previous paper,[61] which were in turn normalized via previous measurements of the total cross section for the reaction $H^+ + H_2 \rightarrow H^o + [H_2^+]$. The estimated absolute accuracy was ± 20 percent while relative accuracy (mostly statistical counting errors) varied from 3 percent at small angles to 20 percent at large angles where the count rate was low.

Peek[62] and Green and Peek[53] have published calculations of the dissociation process for targets of hydrogen atoms, helium, and argon. The salient features of these calculations may best be related by considering the mechanism which is assumed to produce the dissociation. An incident ion enters the collision region in the $1s\sigma_g^*$ state with a certain nuclear spacing R and with an orientation angle Φ with respect to the direction of motion.** The Born approximation is employed to calculate the probability that the projectile is perturbed by the target into making a transition to an unbound state such as the $2p\sigma_u$. The transition is assumed to occur fast enough so that the internuclear separation re-

---

*Standard molecular notation will be used (see, for example, reference 62).

**The vibrational and rational periods are large compared to the time of the collision, thus R and Φ may be specified.

mains unchanged during the collision. After the collision, the repulsive potential causes the molecule to dissociate into the pair $H^+ + H^o$ (or $H^+ + H^*$ if the projectile was excited to a higher state such as the $2p\pi_u$ or $2s\sigma_u$ states. Each fragment receives a kinetic energy equal to $Q(R)/2$ where $Q(R)$ is the change in the repulsive potential energy curve between the point R where the transition occurred and $R = \infty$. Accordingly, each fragment gains a velocity $\underline{u}$ in the rest frame of the projectile where $|\underline{u}| = [Q(r)/M]^{1/2}$ and M = proton mass. Since $|\underline{u}| \ll |\underline{v}|$ where $\underline{v}$ is the initial projectile velocity, the following relation holds to a good approximation:

$$\theta_{Lab} = \frac{u}{v} \sin \Phi \ ,$$

where θ_{Lab} is the laboratory angle at which the dissociation fragments appear. The interesting fact to note is that, since u and sin Φ have an upper limit, there exists an upper limit on θ_{Lab} beyond which no dissociation products may appear. This limit should vary approximately as the inverse square root of the projectile energy.

A detailed comparison between theory and experiment requires the following: an accurate calculation of the cross sections for excitation to the various repulsive states $\sigma_i(R,\Phi)$ as a function of internuclear separation R and orientation angle Φ; a knowledge of the vibrational state populations so that σ_i may be averaged over the variable R with the appropriate weighting factor; an average of $\sigma_i(R,\Phi)$ over Φ must be performed; an accurate knowledge of the Q(R) for the various states; finally the results must be transformed from the H_2^+ rest frame to the lab frame.

McClure,[54] assuming a vibrational population calculated by McGowan

and Kerwin[64] and using the cross section calculations of Peek (unpublished) for excitation to the $2p\sigma_u$ state, performed the calculations outlined above for the angular distribution of protons produced by 10 keV H_2^+ incident on H_2. The results were normalized to experiment at 0.8 degree and showed good agreement in angular dependence.

CHAPTER IV

APPARATUS

An apparatus for the study of differential scattering must include a region for collimating the beam, a target region, and finally a detector for monitoring particles scattered into a small range of angles. It is necessary to provide a high degree of collimation of the incoming projectile beam and a fine resolution of the scattered particles. Consequently, the assembly and alignment of the various apertures is rather critical and has received considerable attention in the design of the present apparatus.

The apparatus consisted of two basic components: an ion accelerator which provided the projectile beam and a large vacuum tank housing the scattering apparatus. The accelerator system comprised an ion source, accelerator, focusing system, and mass analyzer; many of these components were obtained commercially.

The experimental region was housed in a single large vacuum vessel; within this tank were mounted the various components of the experimental arrangement as well as devices for preparing the projectile beam. The incoming beam from the accelerator is prepared by collimation and final alignment, then directed through the target. A slit system selects particles scattered into a small range of angles, and finally the fluxes of scattered particles are detected. Considerable attention was directed

toward design of the vacuum vessel and the mounting of components within it; these matters will also be discussed in detail. The arrangements for handling of signals by the various electronics packages will be discussed at the end of this chapter.

Accelerator

Ions for the experiment were provided by a 4 to 30 keV ion accelerator. The ions were extracted from a conventional RF discharge source, accelerated through a gap lens, focused, mass analyzed, and refocused; the resulting monoenergetic, mass-selected projectiles were then introduced into the experimental vacuum chamber.

The ion source was a conventional ORTEC type 320 source provided with an axial magnetic field for proton current enhancement. The extraction potential could be set from 0 to 5 kV. The source area was RF shielded to prevent interference with sensitive equipment in the laboratory. The various supplies to the source, including voltages, RF power, and gas were all provided from a cabinet maintained at high potential; alteration of operating parameters was by mechanical linkages through insulating Plexiglas rods.

The accelerating potential across the gap lens was provided by two stabilized voltage supplies operated in series. One supply provided the majority of the accelerating potential while the other provided a reproducible fine control for the precise setting and adjustment of the accelerating potential. This adjustment was necessary to compensate for small, long-term changes in the beam energy. It is thought that these changes, which were typically of magnitude of some tens of volts, were due to

changes in the plasma potential within the source.

After being accelerated to the desired velocity, the ions were focused into a parallel beam by an ORTEC type 369B einzel lens. This unit was operated in the decell-accell mode and was most effective for beam energies below 15 keV. Above 15 keV, maximum beam intensity was achieved with no focusing by this lens.

The focused ion beam was then mass analyzed by 60-degree deflection in a transverse magnetic field. The beam passed between pole faces 20.4 cm in diameter and 3.8 cm apart and was shielded from fringing fields by soft iron encasings around the beam entrance and exit tubes. The current which produced the magnetic field was provided by a well regulated Hewlett-Packard constant current supply, type 6296A.

To compensate for small misalignments between the ion source and the rest of the accelerator, two sets of parallel plates were placed between the source and the analyzing magnet. The plates were oriented to permit horizontal movement of the ion beam before entering the magnetic field.

After mass analysis, the ion beam is refocused by a second einzel lens. This lens consists of three brass rings 3.8 cm in diameter and 1.9 cm long. The first and last rings were grounded while a positive potential of up to 6 kV was applied to the middle ring. The inclusion of this unit in the accelerator increased the maximum usable ion beam intensity by a factor of 4.

Pumping for the accelerator was provided by an 800 liters/sec oil diffusion pump trapped with a water-cooled baffle. The pressure directly

above the pump was 3×10^{-7} Torr with the source off, and 2×10^{-6} Torr with the accelerator running.

The source parameters (i.e., pressure, extraction potential, and axial magnetic field) were adjusted to produce the maximum current of the desired ion consistent with a stable beam. It was found that an extraction potential of 3 to 4 kV was optimum for all ion species. Maximum proton content of the extracted ion beam was achieved for pressures just large enough to sustain the discharge. At higher pressures, the H_2^+ and H_3^+ content was increased. Under optimum conditions, the accelerator produced several micro-amperes of mass analyzed beam current. However, the extreme collimation of the experiment reduced this current to ~ 0.1 μA before entering the target chamber.

Vacuum Chamber

All components of the scattering experiment were contained within the large vacuum chamber shown in Figure 1. The chamber was a cylinder with the axis vertical; the internal diameter was 102 cm, and the height was 46 cm. All construction was in type 304 stainless steel. The base of the chamber forms a flat "table top" upon which all of the various experimental components and support systems are mounted. Electrical instrumentation, target gas, and mechanical linkages are supplied through this baseplate. The vacuum pumping stations for the chamber are also located beneath the baseplate. A cylindrical ring is placed around the components on the table, and a flat lid on top completes the vacuum chamber.

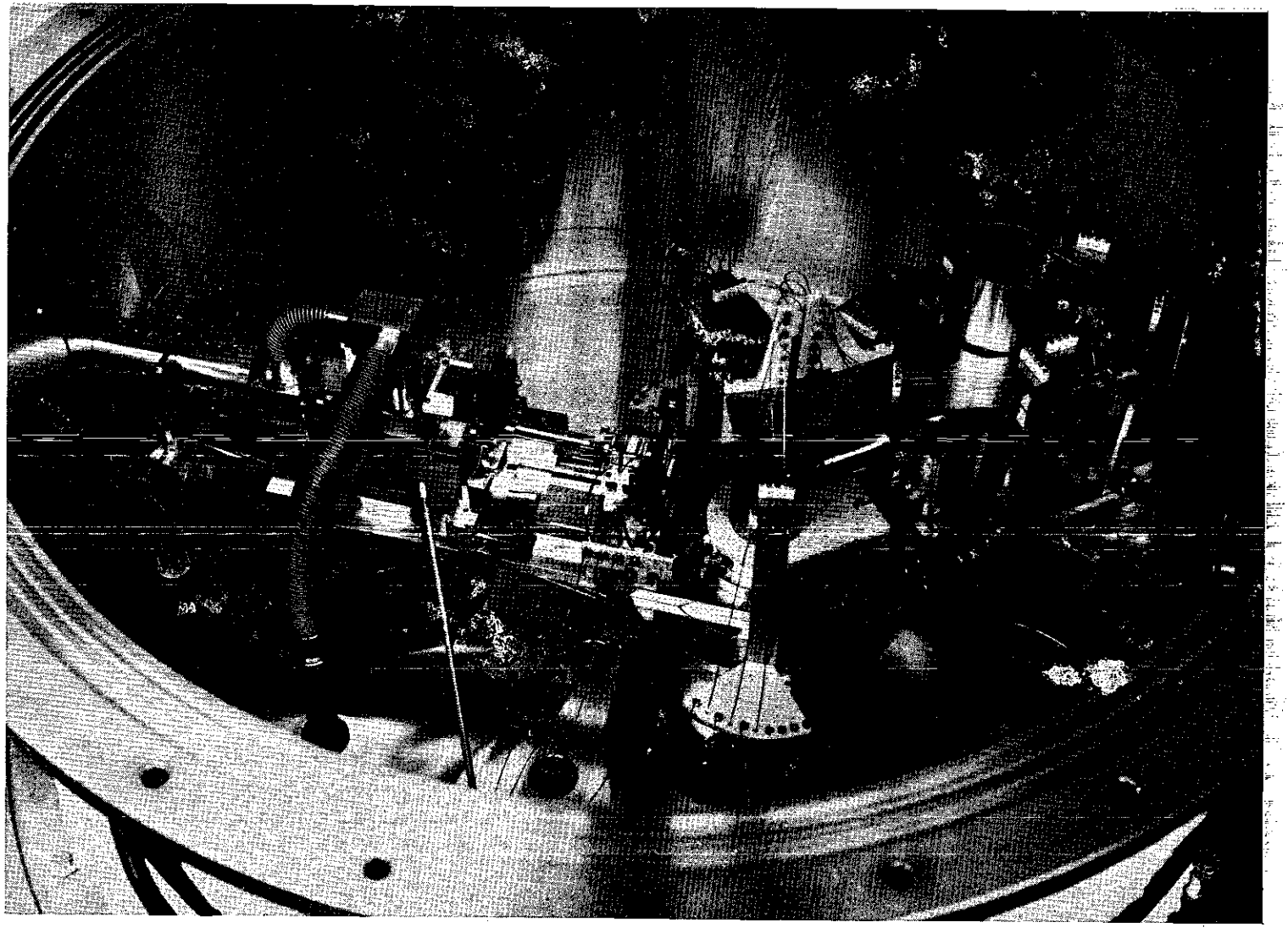

Figure 1 Photograph of the Apparatus.

The cylindrical ring is provided with two 10.2 cm ports at opposite ends of a diameter. To one port is attached a gate-valve which connects the chamber to the accelerator. A 10.2 cm Ultek window is attached to the opposite port. Flanges welded around the top and bottom of the cylinder carry the vacuum seal for both the "table top" and the top cover plate. Each flange contains two concentric O-ring grooves with a pump-out groove between them; Viton O-rings were used in the grooves. It was intended that this groove would be evacuated in order to inhibit permeation of gases through the O-rings into the chamber; however, use of this facility did not appreciably reduce the background pressure, and it was generally not employed.

All electrical leads to the experimental apparatus are fed through vacuum feedthroughs in the baseplate. Vacuum-sealed coaxial feedthroughs are used for low noise signal leads, while Varian 8- or 20-pin feedthroughs are used for non-critical signal leads and voltage supplies. A total of 52 electrical feedthroughs is provided, 4 of which are low-level signal leads.

The chamber is evacuated to a base pressure of 10^{-7} Torr by two 15.2 cm pumping stations. Each station consists of a 2400 ℓ/s NRC VHS-6 diffusion pump trapped with an NRC water baffle and a CVC sorbent trap. A sorbent-trapped Welch 1397B forepump backs the diffusion pumps and roughs the chamber. Pressure in the chamber was monitored by two RG75K Veeco ion gauges, with the second gauge serving as a check on the calibration of the first.

Module Support System

Support of the experimental modules presents several challenging design problems. In any beam collision experiment, accurate alignment of the beam collimators is necessary; but in a differential scattering experiment, especially one designed for measurement near the beam edge, alignment of beam and scattered flux collimators is of paramount concern. For example, a misalignment of only 0.0025 cm can cause a serious asymmetry in the small-angle scattered flux profile. Thus, the support system must lend itself to alignment procedures which are accurate to $\pm$ 0.0013 cm. In addition, it should be possible to move modules along the beam axis and even interchange their position without degrading this alignment. Finally, the support system should be versatile enough so that many experimental configurations may be employed without major modifications.

To satisfy these requirements, a module support system similar to the optical bench routinely used in geometric optics has been constructed. The system consists of two precision rails supported by a central hub. One rail is fixed to the hub and supports the beam-preparation modules, while the other is rotatable in the horizontal plane and supports the scattered flux collimating and detection modules. The target cell, a vertical cylinder, is placed coaxial with the center of rotation of the movable arm and is supplied with target gas and pressure measuring facilities through the hub itself. Since the entire support system rests on the hub, warpage of the baseplate by atmospheric pressure when the chamber is evacuated does not degrade relative module alignment. Any

resulting misalignment with the accelerator is corrected by an electrostatic beam positioner. Figure 2 is a cross-section view of the units assembled and mounted in the vacuum chamber and Figure 3 is a plane view of the scattering apparatus and the module support system.

The hub, as is the entire support system, is constructed of stainless steel type 304. Its large mass is dictated by the rigidity with which it must support the heavy rails and modules. A 10.2 cm hole was bored through its center to allow the target gas to flow from the pressure measuring region below the base to the target cell on top of the hub.

The fixed rail and a large flat plate are attached to the top of the hub. The free end of the 56 cm long rail is supported by a rod extending from the base of the hub to the tip of the rail; this rod prevents warping of the rail when heavy modules are positioned near its end. The flat plate is bolted to the hub and provides support for the rotating rail (see Figure 3). The hub end of the rail is supported on a specially designed ball bearing race placed coaxial with the hub; the free end of the arm is supported on a single captive steel ball. This mounting of the arm permits it to be rotated about the hub through a total angle of 52 degrees (7 degrees to one side of the projectile beam and 45 degrees to the other). The arm is rotated from outside the tank by a mechanical linkage through a vacuum rotary-motion feedthrough. A synchronous motor outside the tank may be coupled to the mechanical drive to permit the arm to be automatically scanned through a range of angles.

Angle measurement is straightforward. A scale, scribed every ten

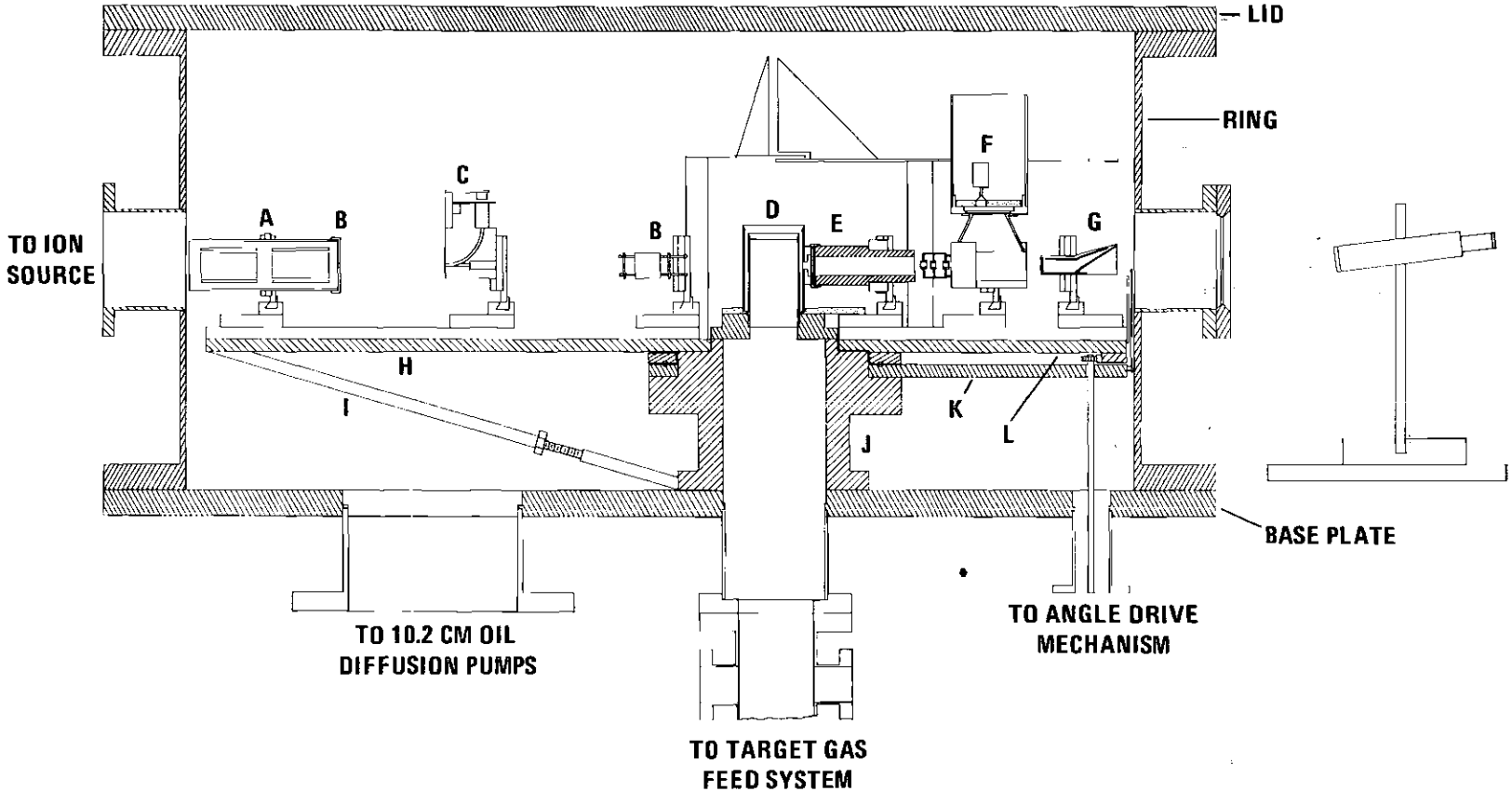

Figure 2 Cross Sectional View of the Apparatus.
A. Beam Positioner; B. Beam Apertures; C. Energy Analyzer; D. Target Chamber;
E. Scattered Flux Collimator; F. H(2s) Detector; G. H^+/H^o Detector; H. Fixed Rail;
I. Support Arm; J. Hub; K. Rotating Rail Support Plate; L. Rotating Rail.

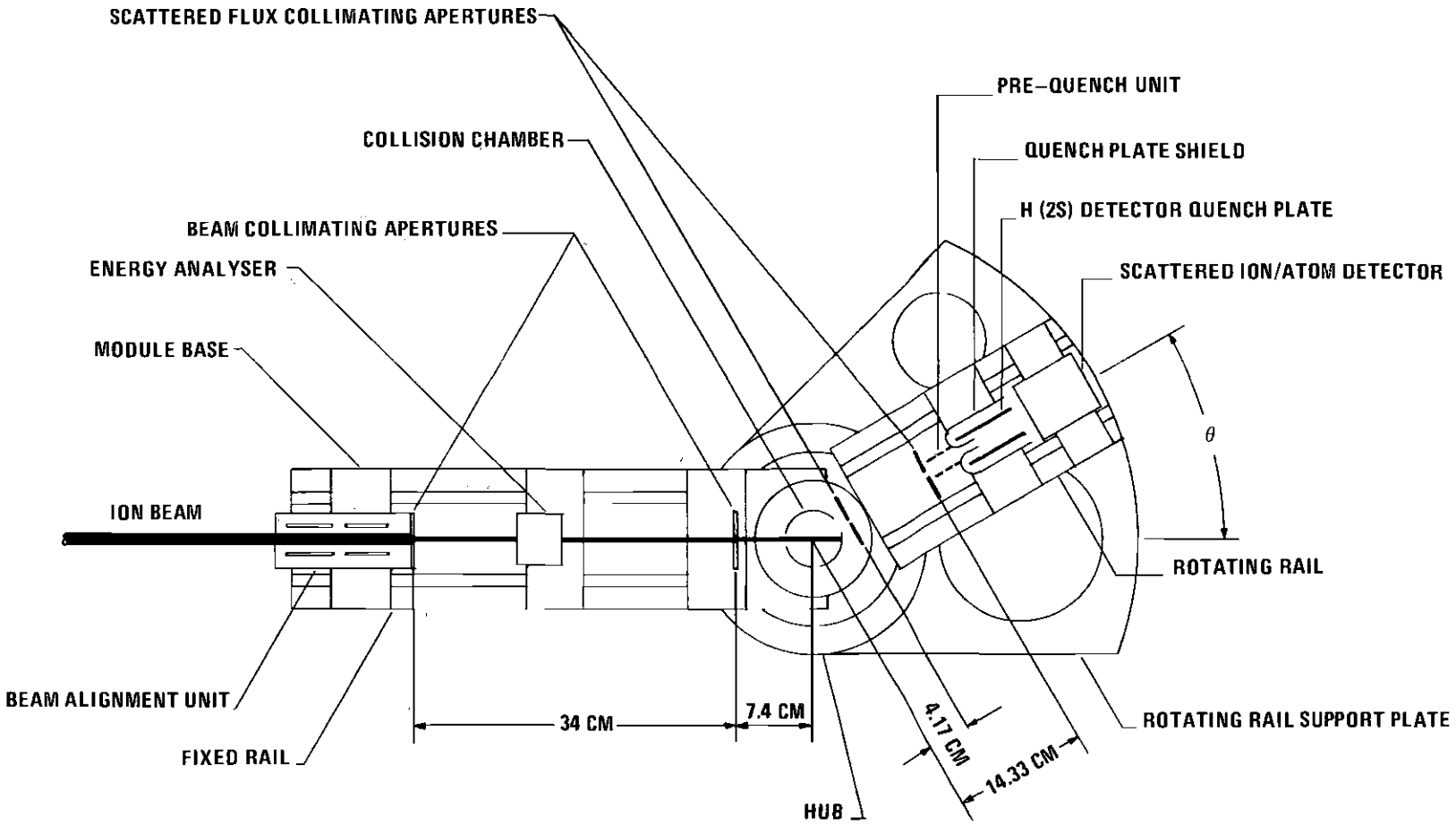

Figure 3 Plan View of the Apparatus.

minutes of arc, is mounted directly to the end of the rotating rail and is read through the window using a telescope mounted outside the vacuum tank. The edge of the scribe marks was resettable to within ± 1 minute. Accuracy of the relative position of the marks on the scale is ± 0.25 minute.

Each support rail consists of two square ridges spaced 10.2 cm apart, extending the length of a flat plate. Since the ridges provide the actual alignment of the experimental modules, considerable care was exercised in their machining. The ridges were machined flat, straight and parallel to within ± 0.0013 cm over their entire length. The center lines of the ridges on both the fixed arm and the rotating arm intersect the vertical axis of the collision chamber, and the rotating arm scans in a plane parallel to the plane defined by the base of the hub* to within ± 0.0013 cm. These stringent machining accuracies were necessary to keep module alignment procedures simple and accurate.

Individual experimental modules are attached to the support arms by a $\sqcap$-shaped clamp called a module base. One side of the base is pulled tight against one ridge by a set screw in the opposite side which presses on the opposite ridge. Modules, which are attached to the flat portion of the base above both ridges, are thus provided a secure, accurate, and versatile mount.

---

*The plane defined by the base of the support hub was used as a convenient reference plane for checking the scanning accuracy of the rotating arm.

Beam Preparation Modules

After entering the vacuum chamber, the ion beam was aligned and collimated by a set of beam preparation modules located on the fixed arm of the rail support system. The beam preparation modules include an electrostatic beam positioner, two beam-collimating assemblies, and an energy analyzer.

The beam alignment unit, which is the first module on the fixed arm, consists of four pairs of electrostatic deflection plates. This unit provided the final alignment of the ion beam from the accelerator with the scattering experiment.

The first beam-collimating assembly was positioned immediately after the alignment module and consisted of an aperture and a secondary electron collector. A second collimator, of similar design, was 34 cm from the first and 7.4 cm from the center of the target cell. The collection of the low-energy electrons produced when the beam was collimated was necessary to reduce the background currents of the scattered flux detectors to reasonable levels. For example, collection of secondary electrons reduced the metastable detector background by two orders of magnitude. The collimating apertures were small holes in thin sheets of stainless steel. Two sets of apertures were used during the experiment. In one set the apertures were circular holes 0.102 cm in diameter; in the other set they were rectangles 0.10 cm high by 0.03 cm wide. The majority of the charge transfer data was taken with the circular apertures, while certain low-angle charge transfer data and all of the dissociation data were taken with the rectangular apertures.

A precision electrostatic energy analyzer was located between the beam collimators and is shown in part C in Figure 2. The analyzer consists of two concentric cylindrical plates whose radii were accurately measured. Normally, the ion beam passed through an aperture in the outer plate and was not deflected. When the energy of the beam was to be measured, accurate potentials were applied to the plates and the ions were deflected through 90 degrees into a Faraday cup. Knowledge of the applied voltage and plate curvature permitted the ion energy to be calculated. A plot of Faraday cup current versus applied potential showed a narrow peak with a full width at half maximum of 2 percent. Since this represented a combination of the energy spread in the ion beam and the finite resolving power of the analyzer (estimated to be ~ 1.5 percent), 2 percent was used as an upper limit on the possible spread in beam energy. Combining the possible errors in the analyzer dimensions and the potentials used, an error of ± 2 percent was assigned to the value of energy corresponding to the peak in the distribution.

Target Chamber and Gas Feed System

The target gas was confined in a vertical cylinder mounted on top of the hollow support hub as shown in Figure 4. The beam was admitted through a small circular aperture and scattered flux exited via a horizontal slot. A second rotatable cylinder was fitted over the first to provide a larger pressure differential (~ 100) and a convenient coupling mechanism to the rotating rail. All apertures in the target cell were large enough to avoid beam interception.

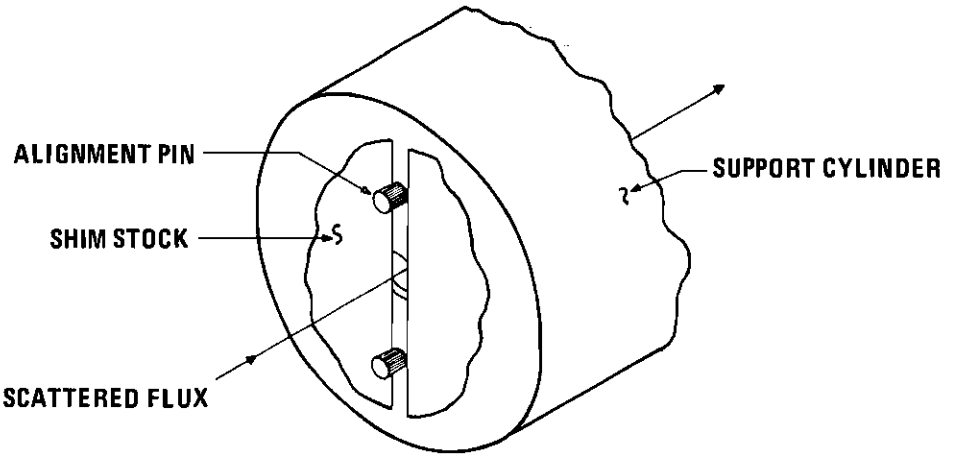

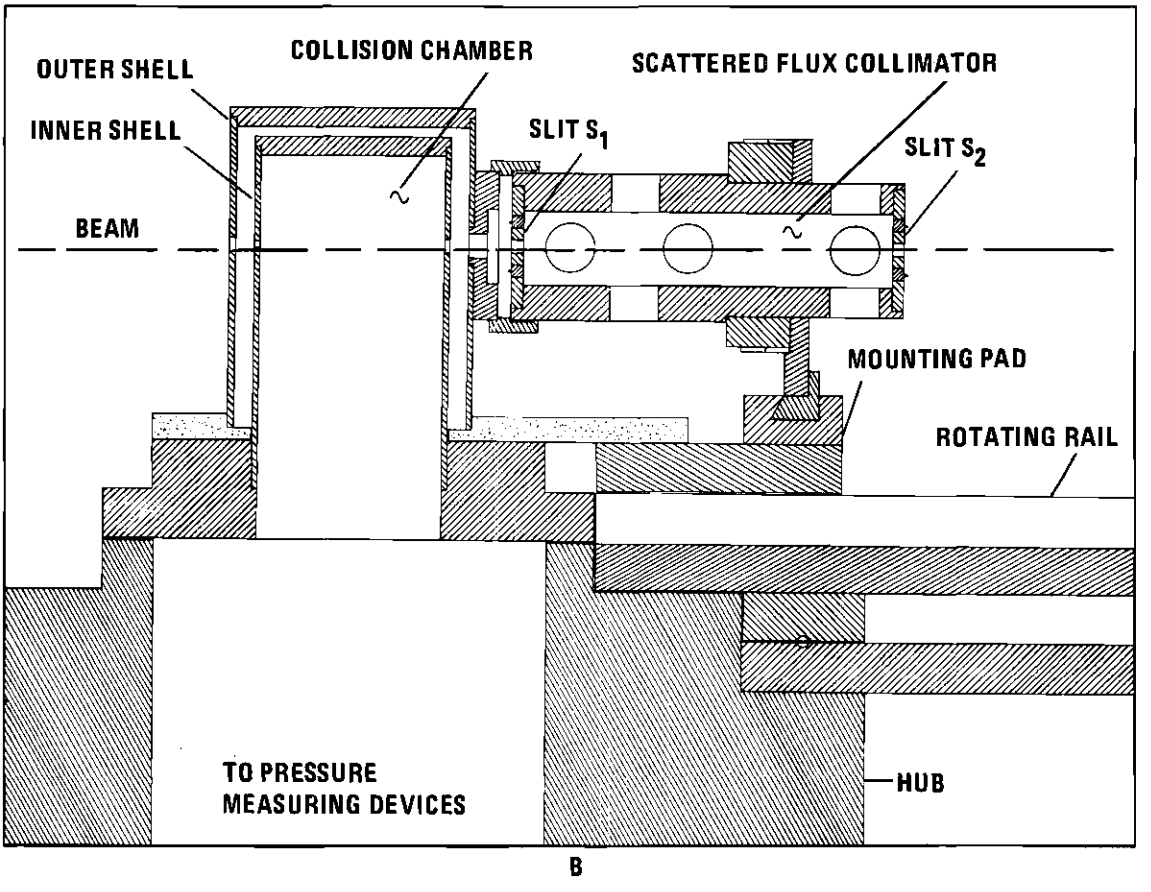

Figure 4 A. Detail of the Scattered Flux Collimator;
B. Detail of Target Cell.

The outer cylinder is 6.03 cm in diameter and has a 0.318 cm high horizontal slot across the projectile entrance side so that it may be rotated without intercepting the ion beam. A narrow vertical slit, which is actually part of the scattered flux collimator, is located on the opposing side for scattered flux removal. The inner shell has a 0.178 cm circular aperture for beam admission and a 0.318 cm high horizontal slot to permit projectiles scattered from +45 to -7 degrees to leave the collision chamber. Both cylinders are electrically insulated for biasing and current monitoring.

The target gas, stated by the manufacturer to be 99.995 percent pure, was supplied from high-pressure tanks and pressure-reducing regulators to a manifold where a solid carbon dioxide and acetone cold trap removed condensable impurities. Provisions for evacuating and baking the gas feed system were provided. The target gas was then leaked into a cylinder attached to the baseplate directly below the hollow support hub. The pressure in this chamber was monitored with a capacitance bridge manometer (MKS Baratron type 771H). In a preliminary experiment, two trapped McLeod gauges using hydrogen gas were used to check the sensitivity of the manometer. The manometer was found to be accurate to within 5 percent from a pressure of 0.4 to 10 microns. The sensing element of the manometer was maintained at an elevated temperature as part of a sensitivity stabilizing system. Corrections were always applied for thermal transpiration caused by differences in temperature between the manometer and the target region.[65]

The target gas flowed from the pressure-measuring region through

the support hub and into the target cell. The large conductance of the hole in the hub effectively eliminated any pressure differential between where pressure is monitored and where the collision takes place.

Scattered Flux Collimator

Projectiles scattered into a range of angles $\Delta\theta$ centered about θ in the azimuthal plane were selected by two narrow vertical slits. As is shown in Figure 4, these slits were mounted on a support assembly which in turn rested on the rotating rail. Considerable care was exercised in the design and construction of these slits and their support structure because any errors in the size, position, or orientation of the collimating slits will be manifest as a systematic error in the measured differential cross section. Since slit widths were on the order of 0.02 cm, alignment and measurement accuracies of 0.001 cm were necessary. To achieve this accuracy, the slits were mounted on opposing ends of a rigid, hollow cylinder, and their relative orientation, both lateral and angular, was checked with an accurate dial indicator to within $\pm$ 0.0013 cm. Correct lateral placement of the module on the rotating arm was checked by the symmetry of the scattered flux.

The slits were formed by partially masking a 0.321 cm hole in each end of the support cylinder with stainless shim stock. Spacing and alignment of the masks were provided by two pins inserted in each end of the cylinder. Figure 4 shows the construction details of one slit.

The first slit (S_1) was 0.0324 cm wide, 0.31 cm high, and 4.17 cm from the center of the target cell, while the second slit (S_2) was 0.1085 cm wide, 0.31 cm high, and 14.33 cm from the center of the target cell.

The slit widths were measured three ways: first by a traveling microscope, second by the diffraction pattern of a 6330 Å laser beam, and third with a micrometer. For S_2, the diffraction method proved inaccurate. Excluding the diffraction method for S_2, all measuring techniques yielded results which agreed within ± 5 percent.

In the calculations presented in Appendix F for the apparatus function, S_2 is assumed to be rectangular. In fact, S_2 is not exactly rectangular, since the top and bottom of the aperture are sections of a circle. The height quoted above is the height of a rectangle whose area is the same as the actual slit and whose width is the measured slit width. Thus, if this height is multiplied by the slit width, the resulting area is the actual area of the slit. Since, in the evaluation of the apparatus function $G(\theta)$, the slit height is used only in the calculation of the area of the aperture, the procedure outlined above introduces negligible error.

Scattered Flux Detectors

After traversing the collimation slits, the scattered flux was monitored by one of the two detectors located on the rotating rail. Scattered neutrals in the metastable 2s state were detected by applying a traverse electric field which mixed the 2s and 2p states, causing the emission of a Lyman-alpha photon. A fraction of these photons was subsequently detected by a funneled electron multiplier operated in the counting mode. Scattered neutrals in any bound state were detected by measuring the current of secondary electrons produced when the atoms were allowed to strike an inclined metal plate. Scattered ions could be detected by secondary emission in the same manner as the neutrals, or the

ion current could be measured directly by changing connections and biases within the module to form a conventional Faraday cup.

Metastable Detector

The metastable flux detection module shown in Figure 5 was located on the rotating rail immediately behind the scattered flux collimator (see Figure 2). The detector consisted of a set of parallel plates which provided the transverse quenching field, a funneled electron multiplier to detect the resulting photon, and a prequench unit for removal of metastables before reaching the field of view of the detector.

The parallel plates were 3.2 cm high by 7.6 cm long and spaced 2.54 cm apart. Two grounded shields were incorporated to reduce the spatial extent of the fringe field; the U-shaped shields wrapped around the front of each quench plate and protruded into the space between the plates approximately 2.6 cm, leaving 5 cm of the quench plate exposed (see Figure 5). Between the quench plates the shields were spaced 0.508 cm apart and were centered on the axis of the scattered flux collimator.

Care was taken to ensure that no appreciable fraction of the metastables was quenched outside the detector's field of view by fringe fields from the quench plates. The intensity of the electric field along the beam axis was calculated to an accuracy of ± 10 percent by the use of a mapping function[66] and was found to rise from 0.1 to 90 percent of its asymptotic value in a distance of 1 cm; it was approximately 50 percent at the edge of the grounded shield. Since the detector viewed a region extending from 2 cm in front of this edge to 7 cm past this edge, the small fraction of metastables quenched by the fringe field contributed to

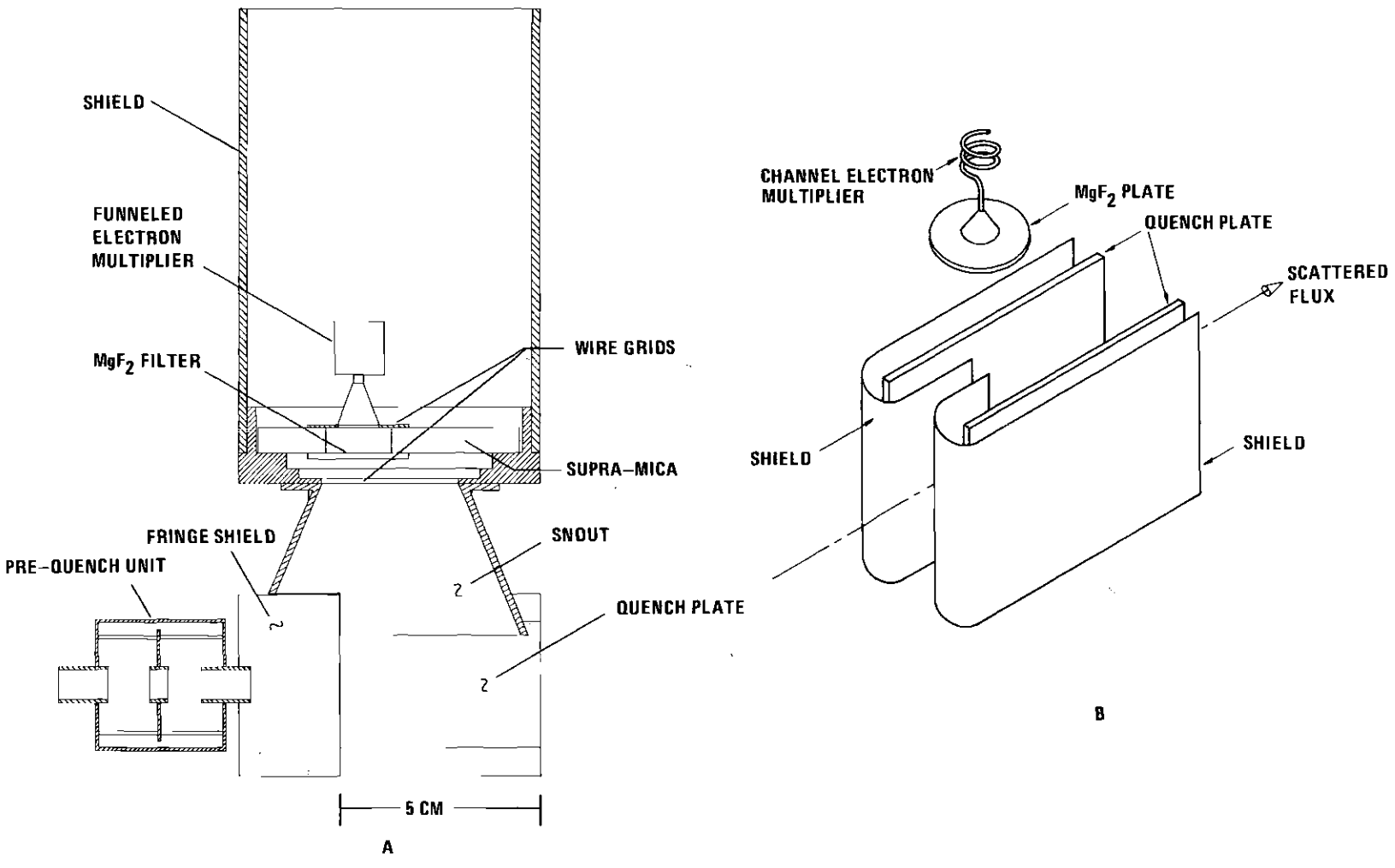

Figure 5 Metastable Flux Detector.
A. Cross Sectional View;
B. Detail of the Quench Plates.

the measured signal. It was concluded that there was no significant loss of signal due to quenching by fringe fields.

It was demonstrated that the signal saturated as the quenching field was increased, and the effective lifetime of the 2s state was lowered until essentially all metastables decayed within view of the detector (see Appendix B). Figure 6 shows a representative saturation curve for impact energy of 25.0 keV. The difference between the signal with the quench field on and with it off should represent the field-induced emission from the 2s state. When the quench field was removed, there was an appreciable background signal. The sources were not completely identified, but the signal included components caused by excitation of the background gas and the impact of the beam on surfaces. There was concern that, when the quench field was turned on, this background might change, particularly due to the alteration in trajectory of the projectile ions and acceleration of stray electrons onto metal surfaces. This problem was obviated by placing before the detection region a "prequench" electric field parallel to the direction defined by the scattered flux collimator. The prequench field removed the metastables before they entered the field of view of the detector. The prequench saturation curve for H(2s) removal for an impact energy of 20 keV is shown in Figure 6. The change in count rate when the quench field was removed while under prequench saturation is a measure of the effectiveness of the prequench unit in removing H(2s). At 20 keV the unit was found to remove 98 percent of the H(2s). For lower energies, this percentage was higher. Background signals observed by the photon detector were unaffected by the presence of the prequench

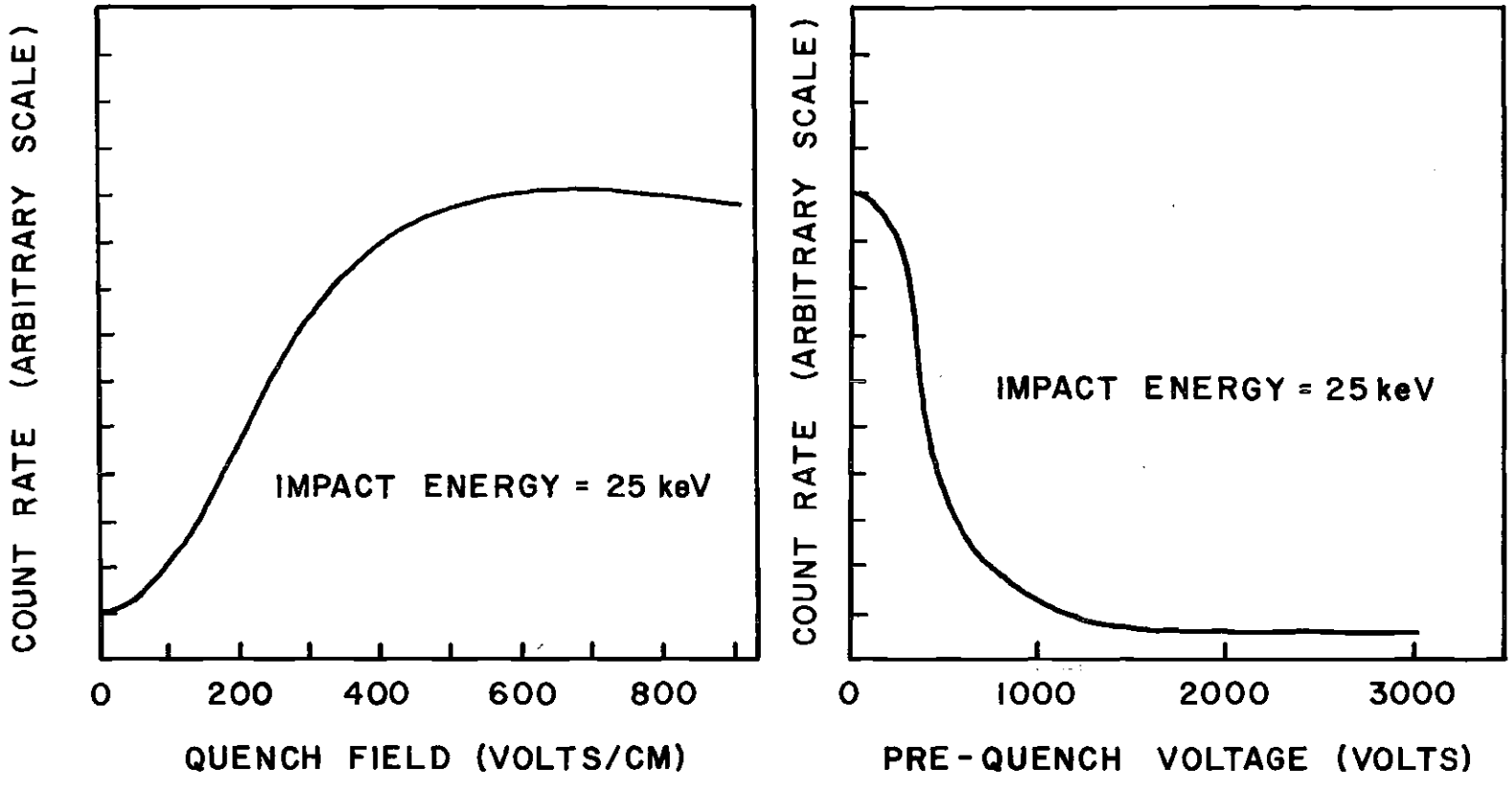

Figure 6 Representative Count Rate Saturation Curves showing Count Rate as a Function of Quench Field and as a Function of Pre-Quench Voltage.

field. Both the quench field and the prequench field were maintained slightly above the value which produced saturation. The difference between the signal with the prequench off and the signal with the prequench on was taken as the true signal from the quenching of metastables.

The possibility of an energy-dependent detection sensitivity is discussed in Appendix B, and a test to ascertain the magnitude of this effect is described. The result of the test indicated that the magnitude of the detection efficiency varied by no more than 10 percent over the energy range of 4 to 20 keV. This variation was not corrected in the data and will be considered as a contributing factor in the accuracy with which cross sections were determined.

Assignment of an absolute value to the H(2s) data was done by normalizing a total charge transfer cross section to absolute data previously published by Andreev et al.[14]; the total cross section for the reaction $H^+ + Ar \rightarrow H(2s) + Ar^+$ at 20 keV impact energy was taken at $3.0 \pm 0.6 \times 10^{-16}$ cm^2. Details concerning the normalization procedure are located in Appendix B. A summary of the possible errors involved is presented in Chapter V.

Two funneled electron multipliers were used during the course of the experiment. A Mullard type B 419 BL was used for all of the total cross section work; a Bendix type 4039 was used for most of the differential work. The detector was changed when the Mullard unit developed a rather high background count rate of one count per second.

In order to utilize the extremely low inherent background of this type of detector (0.03 count/sec), secondary electrons and ultraviolet

photons produced at the beam collimation apertures had to be suppressed. The electrons were collected by biased electrodes near each aperture and large baffles coated with soot. The reflectance of soot at 1216 Å was measured using a vacuum monochromator to be one percent. The detection module was completely shielded with stainless steel shim stock coated with soot. The presence of soot did not materially affect the 10^{-7} Torr background pressure in the vacuum chamber. These precautions reduced the photon detector background from 5 counts/sec to its limit of 0.03 count per sec with the beam on, no target gas in the collision cell, and the apparatus set to a large scattering angle.

Ion and Neutral Detector

Scattered ions and neutrals were detected by the last module on the rotating arm (see Figure 2). This module is a specially designed Faraday cup which may be operated as a neutral detector by measuring the secondary electrons formed when the atoms strike a plate in the back of the cup. Figure 7 shows the internal construction of this detector and the electrical connections used for the two modes of operation.

Scattered flux enters the module through an aperture 0.64 cm high and 6.4 cm wide. The extra width of the aperture is necessary because the ion flux is deflected by the H(2s) detector quench field and because it is desirable to be able to monitor this current with the quench field on. Three insulated plates (set at an angle of 60 degrees from normal with respect to the incoming flux) form the back of the module. The center plate is 0.65 cm wide, and the left and right plates are each 2.54 cm wide. Immediately above the plates is an electrode which may be biased

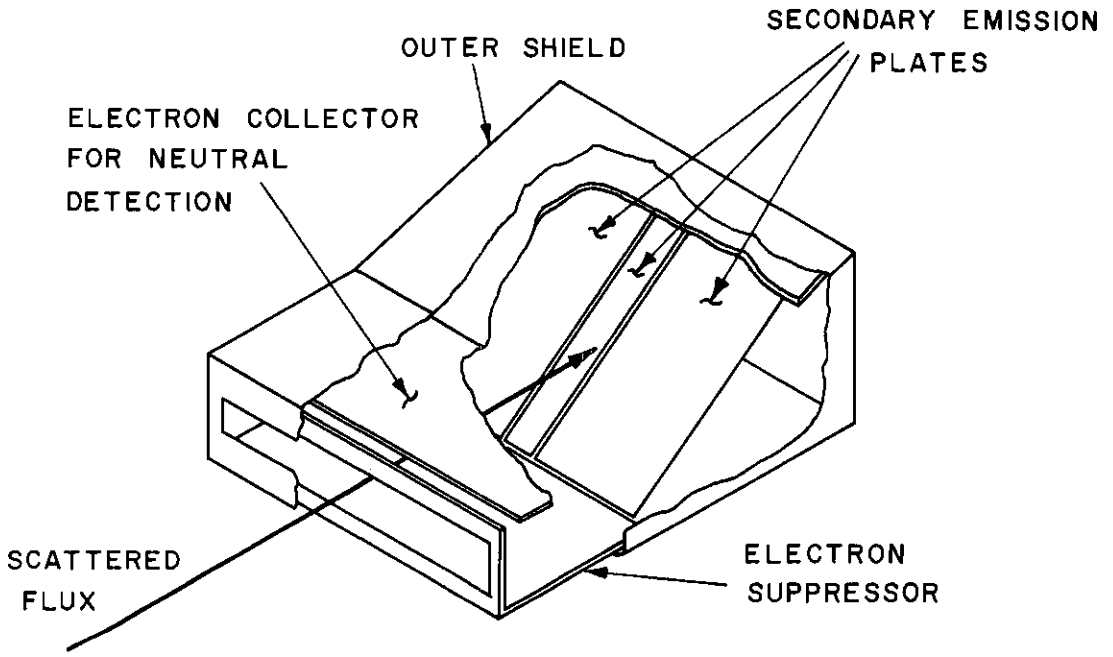

INTERNAL CONSTRUCTION

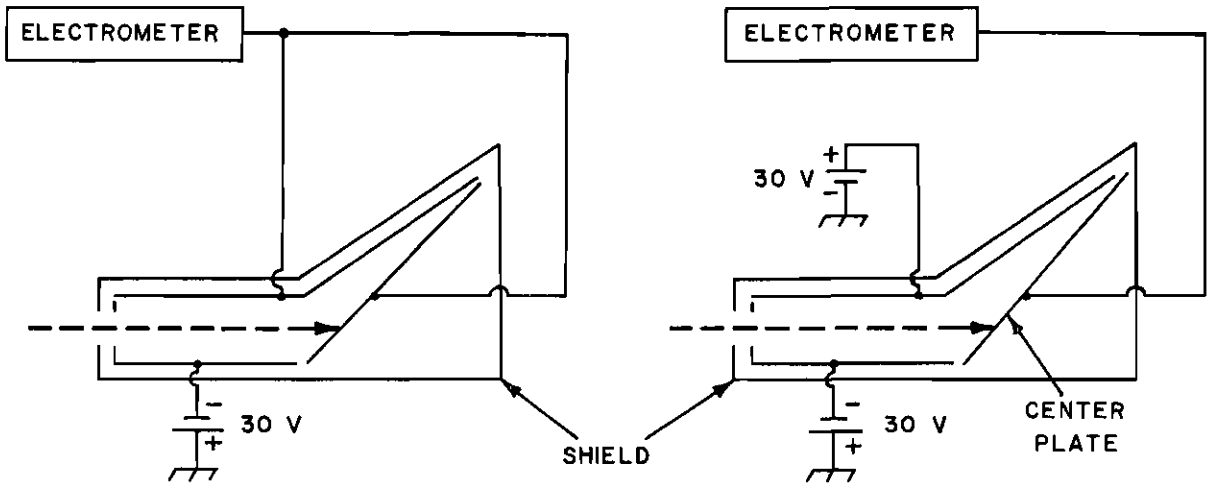

FARADAY CUP MODE

SECONDARY EMISSION MODE

BIASING CONNECTIONS

re 7 Faraday Cup Arrangement for Detection of Ions and Atoms. Shows Internal Construction and Operational Connections in Faraday Cup Mode and Secondary Emission Mode.

for secondary electron collection. Inside the module is an electrode biased to suppress secondary electrons and prevent their escaping. All biasing potentials in this unit demonstrated current saturation thus indicating correct operation.

To detect neutral flux, the quench field of the metastable detector was used to deflect the scattered ions from the central plate; secondary electrons leaving the plate were then collected by the electrode located overhead. An electrometer was used to measure the apparent positive current to the center plate caused by the loss of secondary electrons; thus, the current to the center plate was $I_o = \gamma_o i_o$, where γ_o is the average secondary emission coefficient for neutral atoms and i_o is the effective neutral "current."* A subsidiary experiment was performed to measure γ_o (see Appendix C). When the quench field was removed and both ions and neutrals were permitted to strike the center plate, the current measured was $I_T = [\gamma_+ + 1]\, i_+ + \gamma_o i_o$, where γ_+ is the average secondary emission coefficient for ions and i_+ is the true ion current. Thus, by first measuring i_+ using the detector in the Faraday cup mode and then measuring I_T and I_o using the secondary emission mode, γ_+ could be evaluated via $\gamma_+ = (I_T - I_o)/(\gamma_+ + 1)$. During the experiment, i_+ was measured either by the secondary emission current or directly by using the module as a Faraday cup; neutral current i_o was determined from the secondary emission current I_o.

A vibrating reed electrometer (Cary type 31) was used for measuring

---

*The effective neutral current is defined as $|e|$ times the neutral flux.

current from the ion/atom detector. The electrometer outputs when using the various scales and the three input resistors (10^{10}, 10^{11}, and 10^{12} ohms) were intercompared using a constant current source; small corrections were applied for differences in response observed when using the three input resistors. The overall absolute sensitivity was calibrated by the use of a standard current source composed of a standard voltage source (accurate to 0.01 percent) and a standard resistor (accurate to 1 percent).

Data Acquisition

The apparatus described in the preceding sections was operated in several different modes, depending on the particular data to be recorded. In this section these modes of operation are described, and techniques used for data acquisition are outlined.

In Chapter II the operational definition of a differential cross section was derived. The variables which must be measured to permit the calculation of the cross section are: (a) angle of scattering, (b) incident projectile current, (c) target number density, and (d) post-collision currents.

Measurement of the scattering angle was carried out simply by visually observing a graduated mechanical scale.

Two methods for monitoring the projectile current were used corresponding to whether differential or total cross sections were being measured. For differential scattering data, the projectile current was collected on the outer shell of the collision chamber after passing

through the target gas. The inner shell was biased to suppress secondary electrons formed when the beam struck the outer wall. For total cross sections, the ion beam was collected at the end of the rotating arm by the ion/atom detector which was operated in the Faraday cup mode.

The target number density n was evaluated from the measured pressure by the ideal gas law $P = nkT$, where k is Boltzmann's constant and T is the absolute temperature of the target gas. As previously outlined, the pressure was monitored by a capacitance manometer.

In general, both the target gas pressure and the incident projectile flux were recorded manually from the measuring instruments.

Data acquisition for the post-collision currents was semi-automatic. Pulses from the metastable detector were amplified with an ORTEC 113 preamplifier and a 410 amplifier, discriminated by a 421 discriminator and then scaled. A voltage-to-frequency converter was used to change the direct current from the electrometer measuring I_T or I_o to a series of pulses whose frequency was proportional to the magnitude of the signal. These pulses were then scaled. The contents of the scalers were periodically printed on a standard teletype unit and thus recorded.

Figure 8 shows the system flow charts used for measuring total and differential cross sections. Included in the figure are descriptions of operating modes for the measurement of the several types of post-collision flux.

While measuring the total neutral current, the primary beam could not be monitored. The neutral current was read as quickly as possible and the beam current checked before and after the measurement. The beam was stable to within one percent, and this technique was considered acceptable.

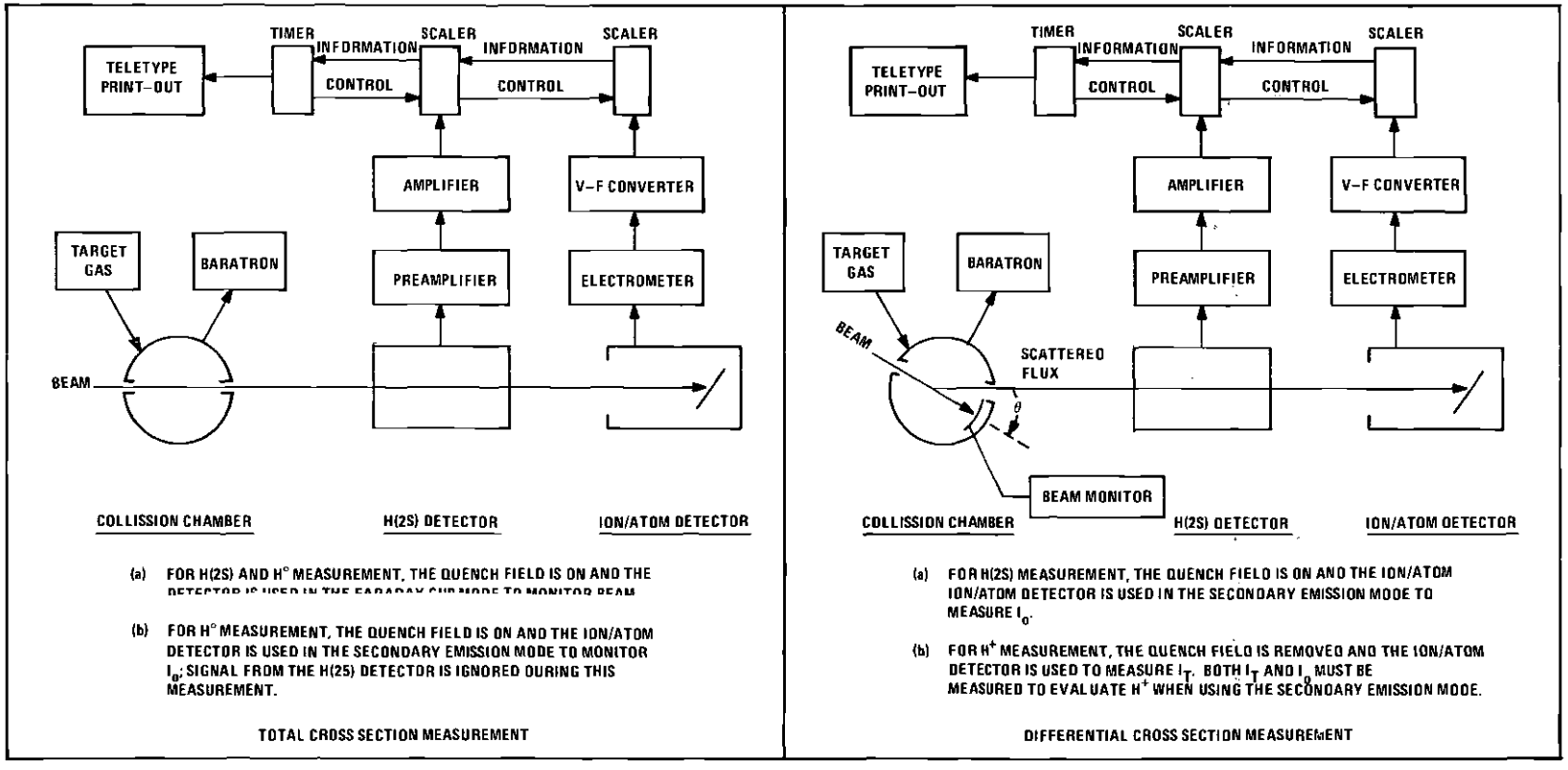

Figure 8 Flow Charts for Data Handling.

CHAPTER V

ERROR ANALYSIS

The relation between the quantities which are measurable in the laboratory and the microscopic differential cross section for the production of the i^{th} post-collision species was derived in Chapter II and is given by equation (20). There it was shown that the differential cross section could be written as the ratio of the i^{th} species detector current (or count rate) $N_i(\theta)$ to the incident beam current I_p, the target number density N_t, the detector sensitivity $(De)_i$, and the angular dependent geometrical factor $\int_{L(\theta)} \Delta\omega dx$. It is implicit that the scattering angle θ, the projectile energy E, and the purity of the target gas and projectile beam must also be determined.

The following analysis of possible systematic and random errors in the measured differential cross sections presented in Chapters VI and VII will consist of investigating separately each of the above mentioned factors.

Projectile Purity

The magnetic mass section and the high degree of beam collimation by the two apertures located on the fixed support arm provided adequate ionic species separation for all projectiles used in this experiment. Scans of the projectile current to the collision chamber as the magnetic field intensity was varied showed well resolved peaks for H^+, H_2^+, and

H_3^+.

It is concluded that there were no chemical impurities in any of the ion beams. However, there was no knowledge of the vibrational states of either the H_2^+ or H_3^+ projectiles.

Target Purity

As mentioned in Chapter IV, the target gas (stated to be 99.995 percent pure) was supplied from commercial high-pressure tanks and was passed through a solid carbon dioxide and acetone cold trap to remove condensable impurities.

It was concluded that there was no significant error due to target impurity.

Projectile Energy

An electrostatic energy analyzer was used to measure the beam energy at the start and end of each angular scan. A description of the analyzer and its operation is given in Chapter IV. There it is shown that the analyzer determined the beam energy to an accuracy of ± 2 percent.

Scattering Angle

The angular setting of the rotating arm was read from the mechanical scale at its end; the reading accuracy was ± 0.017 degree.

It was necessary to determine the setting for an effective angle of zero degrees, because the precise alignment of the primary beam would vary a small amount from one day to the next. Two methods were used. In the first and simplest approach, the detector was automatically scanned

through the primary beam and the center line of the beam distribution taken as the reference point for zero degrees. This technique was satisfactory for the study of dissociation where the scattered flux varied slowly with angle; however, for charge transfer, where the angular distribution was very steep, a more precise method was used. In this second method, the scattered H^{o} and H^{+} flux was monitored on both sides of the beam. The center line of the scattered particle distribution was taken as the zero-degree reference point. The distributions were always quite symmetric.

There was a considerable amount of difficulty due to small changes of beam orientation during data taking. The evidence for such changes was that the flux of scattered H^{o} and H^{+} would drift down (or up) by amounts which could not be correlated with changes in beam intensity. It was decided that changes of up to two percent were tolerable; when the change in flux exceeded that value, the run was abandoned, the beam recentered, and the effective value of the zero-degree setting redetermined. This problem was most severe for the charge transfer measurements because here the cross section varied very rapidly with angle.

Taking all the above points into consideration, it is estimated that the angle θ was determined to better than $\pm$ 0.026 degree for the electron capture experiment and $\pm$ 0.045 degree for the dissociation experiment.

Beam Current

The projectile beam current was collected on the outer shell of the collision cell after passing through the target region. The inner

shell was biased to suppress secondary electrons.

Systematic errors in measuring the beam current may be caused by the following:

(a) loss of current by interception of target exit aperture,

(b) inadequate suppression of secondary electrons,

(c) beam neutralization in the target cell, or

(d) calibration error of the electrometer measuring the beam current.

The exit aperture of the collision chamber was sufficiently large to pass the beam without interception. This was checked by monitoring the current to the inner shell. This current was proportional to target gas density and was attributable to target ions formed by the electron capture process (see Appendix C).

The current to the outer shell was measured as a function of the bias on the inner shell. The current was found to saturate for potential of -10 to -15 volts. Data were taken with -30 volts on the inner shell.

Because of the low target pressures used (usually less than 0.5 micron), beam neutralization was usually less than 2 percent for the electron capture study and 5 percent for the dissociation studies. Corrections were made for the dissociation work but not for the electron capture work.

The electrometer used to measure the beam current was calibrated using the same absolute standard described in Chapter IV. The electrometer was found to be accurate to within ± 3 percent over all ranges used.

The only random errors involved in measuring beam current were

scale reading and zero drift. The sum of these was estimated to be less than 2 percent.

It is estimated that the systematic error in measurement of I_b did not exceed +3 and -5 percent for electron capture data and ± 3 percent for dissociation data. The random errors were less than ± 2 percent for both studies.

Target Density

The ideal gas law was used to relate the target pressure to the target number density. The relation used was

$$N_t = 3.24 \times 10^{13} P \ , \qquad (41)$$

where a temperature of 298°K has been assumed. P is the target pressure in microns and N_t is the target number density (cm^{-3}). The target pressure was monitored with a capacitance manometer. It was shown that the systematic error in this device did not exceed ± 5 percent (see Chapter IV). Random errors due to changes of room temperature, zero drift, and pressure fluctuations caused an uncertainty of less than ± 2 percent.

Scattered H^+ and H^o Flux

Scattered H^+ and H^o were detected as currents, either directly with the Faraday cup (for H^+ only) or indirectly, using the secondary emission technique. The currents were measured by a Cary vibrating reed electrometer. The output of this device was digitized and scaled for periods of 10 to 100 seconds.

The only source of random errors was cable noise observed for very

low-current scales on the Cary. This was essentially removed by the method used to record currents. Random errors also occur due to drifts in pressure, primary beam current, and beam orientation (shift in beam center line). However, these sources of error are already included in the discussions of the preceding sections.

Systematic errors in measurements of scattered H^+ and H^o may be caused by the following:

(a) loss of flux between point of formation and point of detection,

(b) systematic errors in the measurement of $(D_e)_+$ and $(D_e)_o$ (the detection efficiencies for H^+ and H^o), or

(c) systematic error in the calibration of the Cary electrometer.

The only mechanism for loss of scattered H^+ or H^o is a second collision. This possibility was eliminated by operating in a pressure region where the detected signal was linear with target density (a second collision process would exhibit a square low dependence on target density).*

As was discussed in Chapter IV, scattered H^+ was monitored in one of two ways. The ion/atom detector could be operated as a conventional Faraday cup or as a secondary electron emission detector. When operated as a Faraday cup, $(D_e)_+$ was essentially unity. The various suppression potentials in the cup ensured that secondary electrons formed could not escape, thus giving an erroneously high current reading. When operated in the secondary emission mode, $(D_e)_+$ was $\gamma_+ + 1$, where γ_+ is the H^+ coefficient for electron emission. The measurement of γ_+ is discussed in Chapter IV and Appendix C. It is believed that the absolute value of

*For example, see the discussion in reference 67.

γ_+ is known to within ± 5 percent for all impact energies

Scattered H^o was monitored with the ion/atom detector operating in the secondary emission mode. The measurement of the secondary emission coefficient for neutrals, γ_o, is described in Appendix C. The ratio γ_o/γ_+ was measured to an accuracy of ± 5 percent and used in conjunction with measured values of γ_+ to evaluate γ_o through the experiment. Since the measurement errors involved in determining γ_o/γ_+ and γ_+ are independent, the possible error in the value of γ_o is estimated to be the square root of the sum of the squares of the two errors, that is, approximately ± 7 percent.

The calibration of the Cary electrometer was discussed in Chapter IV. There it was shown that, after minor corrections were applied, the systematic error in the calibration was less than one percent.

It is therefore concluded that the random errors are essentially zero, and the systematic errors do not exceed ± 5 percent for H^+ and ± 7 percent for H^o measurements.

Scattered H(2s) Flux

The field-quenched Lyman-alpha photons were counted individually by a continuous electron multiplier. The detector count rate was usually well below 100 c/s and never above 500 c/s for all differential data; thus no dead-time corrections to the count rate were necessary.[68]

The statistical nature of microscopic processes was quite evident at these low count rates. In principle, these inherent statistical fluctuations may be reduced to arbitrarily small values by counting for a sufficiently long period of time. However, in the case of the electron

capture data, time limitations imposed by the tendency for the accelerator to become unstable after 8 to 10 hours operation required the acceptance of a finite value for these fluctuations. For small and intermediate angles (where the count rate was highest), data were usually taken at each angle until approximately 1000 signal counts were accumulated. For the larger angles (greater than one degree) total signal counts of 200 to 400 were usually taken with a few of the 4 keV large-angle points consisting of 100 to 200 signal counts. The background signals (target gas removed from the collision cell) were 10 to 15 percent of the net signal for the higher impact energies and 20 to 30 percent at 4 keV. The net signal was always corrected for this background in the case of electron capture.

The dissociation data did not suffer from such low count rates, and at least 1000 signal counts were usually taken at each angle. In addition, the signal due to background gas in the collision chamber was always less than 3 percent of the net signal. The dissociation data were not corrected for this background.

Systematic error in the measurement of the H(2s) flux may be caused by the following:

(a) evaluation of the detection sensitivity $(D_e)_{2s}$,

(b) velocity dependence of $(D_e)_{2s}$,

(c) loss of H(2s) flux by collisional de-excitation or ionization,

(d) loss of H(2s) flux by electric fields other than the quench or pre-quench fields,

(e) loss of H(2s) flux by the fringing of the quench field, or

(f) insufficient quench or pre-quench fields.

Most of these possibilities are thoroughly discussed in Appendix B.

The detection efficiency was determined by the normalization of a measured total (in angle) electron capture cross section to a previously published absolute value. The quoted possible error of this cross section was ± 20 percent. Including possible polarization effects (see Appendix B), this possible error becomes +38 percent, -14 percent.

A test described in Appendix B was performed to ascertain the existence of a velocity dependence of $(D_e)_{2s}$. It was concluded that, to an accuracy of ± 10 percent, $(D_e)_{2s}$ was velocity independent.

Data were taken only for target pressures where the detected H(2s) flux was shown to be linear with target density, thus precluding H(2s) loss via a second collision.

The path from the center of the collision chamber to the H(2s) detector was well shielded from extraneous electric fields. Tests were conducted by applying potentials to nearby spare electrodes and observing the count rate. No change could be detected for potentials which were equal to any used in the system. However, the 30-volt bias on the inner shell of the collision chamber did cause a small fraction of the H(2s) to decay before reaching the detector. This effect was measured carefully by temporarily removing the bias and noting the increase in count rate. The loss varied from 6.4 percent at 4 keV to 2.5 percent at 20 keV. All 2s data were corrected for this effect.

The loss of H(2s) by the fringing of the quench field is shown in Appendix B to be negligible.

Finally, the effectiveness of the pre-quench and quench fields in

quenching the metastable atom is discussed in Chapter IV and Appendix B. It was found that the quench field was essentially 100 percent effective, while the pre-quench unit removed at least 97 percent of all H(2s).

Using a 96 percent confidence level, the estimated random errors for the measurement of the 2s flux are as follows:

(a) ± 6 percent for all dissociation data,

(b) ± 6 percent for low-angle electron capture data ($\theta < 1$ degree),

(c) ± 15 percent for most large-angle electron capture data, and

(d) ± 20 percent for large-angle electron capture data at 4 keV.

It is estimated that the total possible absolute error in the measurement of the 2s flux is less than +39 percent and -17 percent.

Geometrical Factor

The geometrical factor $\int_{L(\theta)} \Delta\omega dx$ is evaluated in Appendix F for the particular geometry employed in the present experiment. Errors in the calculated magnitude of the geometrical factor are due to uncertainty in the measurements of the dimensions of the collimating slits and their position. The effect of these errors on the value of the geometrical factor was determined by evaluating the geometrical factor using slit dimensions which were varied by the estimated possible error. The maximum change in $\int_{L(\theta)} \Delta\omega dx$ recorded was ± 6 percent. Since the errors for each slit should be independent, 6 percent is an upper bound on the possible error in the magnitude geometrical factor.

Also discussed in Appendix F is the fact that the finite acceptance angle causes the measured differential cross sections to be systematically

higher than the true cross section. The magnitude of this shift depends on the rate of change of the cross section with scattering angle (it is zero for an isotropic distribution and increases as the rate of fall increases). No attempt has been made to compensate for this effect in any of the data presented in Chapters VI and VII. The effect should be smaller in the dissociation data than in the electron capture data and should not be important for the probability data since these are ratios of cross sections.

It is concluded that the systematic error in the evaluation of the geometrical factor is less than ± 6 percent. The effect of the finite apparatus resolution on the measured differential cross sections is not directly accessible.

Cascade Effects

None of the 2s data presented in Chapters VI and VII have been corrected for population by cascade from higher $n\ell$ states. It is not possible to make such a correction due to the fact that no information is available on the absolute differential cross section for the formation of these higher states.

In the case of electron capture, Andreev et al.[69] show that the total cross section for formation of the 3p state is only 10 percent of that for the 2s level. Since the branching ratio for decay will ensure that only 10 percent of the 3p states will decay to the 2s level (the remainder go to the 1s ground state), cascade population of the 2s by the 3p level is approximately one percent. It can be shown that contributions from higher states are probably less than one percent. In the event that,

for large angle scattering the relative population of the 2s and 2p states is similar to that for totals, cascade effects may be neglected.

No measurements have been made of total dissociation reactions for the formation of the 3p or higher states for the energy range and targets used in this study. Therefore, no comparison of cascade effects may be made. However, it seems unlikely that the probability for formation of the 3p state would be as large as or greater than that for the formation of the 2s state. Even if it were equal, the cascade population of the 2s level would only be a 10 percent effect.

Although no quantitative predictions of cascade population of the 2s state for differential scattering are possible, it is thought that the effect is small.

Summary

A summary of the preceding error discussions is now presented in three sections. First, the possible systematic and random errors in the measurement of scattering angle are reviewed. Second, the possible systematic errors in the differential cross sections are presented; and finally, the possible random errors in the cross sections are discussed.

A possible systematic error in the measurement of scattering angle was in the location of the zero mark. For the electron capture work, this mark was located to within ± 0.017 degree, thus producing a possible systematic error which varied from 3.4 percent at 0.5 degree to 0.6 percent at 2.0 degrees. For the dissociation work, the zero mark was located to within ± 0.03 degree. This produced a possible systematic error which varied from 6.0 percent at 0.5 degree to 1.0 percent at 3.0 degrees. The

random error in reading each angle was less than 0.017 degree.

Data were taken as angular scans for a fixed impact energy. These scans were related for various energies, and finally absolute magnitudes were assigned. Thus, three separate types of possible systematic error must be considered.

The only constituents of the differential cross section which might contain angle-dependent systematic errors are the geometrical factor $\int \omega dx$ and the detection efficiency $(D_e)_i$. The geometrical factor was accurately evaluated as a function of scattering angle and should not contain an angle-dependent error. The detection efficiencies $(D_e)_+$ and $(D_e)_o$ were measured as a function of scattering angle and thus should also be free of angle-dependent errors. Finally, by its nature $(D_e)_{2s}$ does not depend on scattering angle and thus should not contain an angle-dependent error.

The only constituent of the differential cross section which may exhibit a dependence on impact energy is the detection efficiency $(D_e)_i$. The explicit energy dependence of $(D_e)_+$ and $(D_e)_o$ was measured to within $\pm$ 5 percent for all energies used. The variation in $(D_e)_{2s}$ with impact energy was found to be less than 10 percent for energies between 4 and 20 keV.

The evaluation of each differential cross section required the multiplication or division of a number of terms, each carrying a possible systematic error in its absolute value. The linear addition of these possible errors gives the absolute maximum possible error in the cross section. Since each possible error is independent of the rest, it is of interest to calculate the net possible error by adding the constituents

as orthogonal vectors. Both results will be quoted below.

The net possible systematic error in the absolute value of the differential cross sections for the formation of H^+ and H^o is found to be ± 20 and ± 24 percent, respectively, by linear addition and ± 11 and ± 12 percent by orthogonal addition.

The net possible systematic error in the absolute value of the differential cross section for the formation of H(2s) is found to be + 52 and - 30 percent by linear addition and + 39 and - 16 percent by orthogonal addition.

The net possible random error in the relative differential cross sections for the formation of H^+ and H^o at a single energy was evaluated to be ± 4 percent by linear addition (± 3 percent by orthogonal addition).

The net possible random error in the relative differential cross section for the formation of H(2s) at a single energy depends on the specific reaction, energy, and angle range under consideration. For low-angle electron capture data, random error was ± 10 percent by linear addition, ± 7 percent by orthogonal addition; for high-angle ($\theta > 1.0$ degree) electron capture data, random error was ± 19 percent linear, ± 15 percent orthogonal; for high-angle, 4 keV electron capture data, random error was ± 24 percent linear, ± 20 percent orthogonal; and for all dissociation data, random error was ± 10 percent linear, ± 7 percent orthogonal. If the uncertainty in scattering angle is included, the estimated possible random errors are in agreement with the scatter in the data shown in Chapters VI and VII.

As a final comment, it should be remembered that, due to the finite

system resolution, there may exist a systematic difference between the measured differential cross sections and the true microscopic cross sections. This effect should not be present in ratios of cross sections and should be minimal for the dissociation work.

CHAPTER VI

ELECTRON CAPTURE RESULTS AND DISCUSSION

The electron capture results will be discussed in four sections. In the first section, the differential cross section for the formation of H^+, H^o, and H(2s) will be presented as a function of laboratory scattering angle for impact energies between 4 and 20 keV. From these data, the total differential cross section will be derived and discussed. The third section will present the measured probabilities for electron capture into all states, P_o, and into the 2s state, P_{2s}. The last section will present measurements of the fractional content of the scattered neutral flux in the 2s state.

Measured Differential Cross Sections

Figure 9 shows the measured differential cross sections for the formation of H^+, H^o, and H(2s) during large-angle proton-helium collisions. The possible systematic and random errors in these data were discussed in Chapter V.

Data are not presented for angles less than 0.4 degree for two reasons. In the case of scattered H^+, the scattered current could not be distinguished from unscattered primary beam. In principle, electron capture collisions could be studied down to zero degrees. However, for angles less than 0.4 degree, the definition of the geometrical factor became unclear (see Appendix F), and thus differential cross sections could

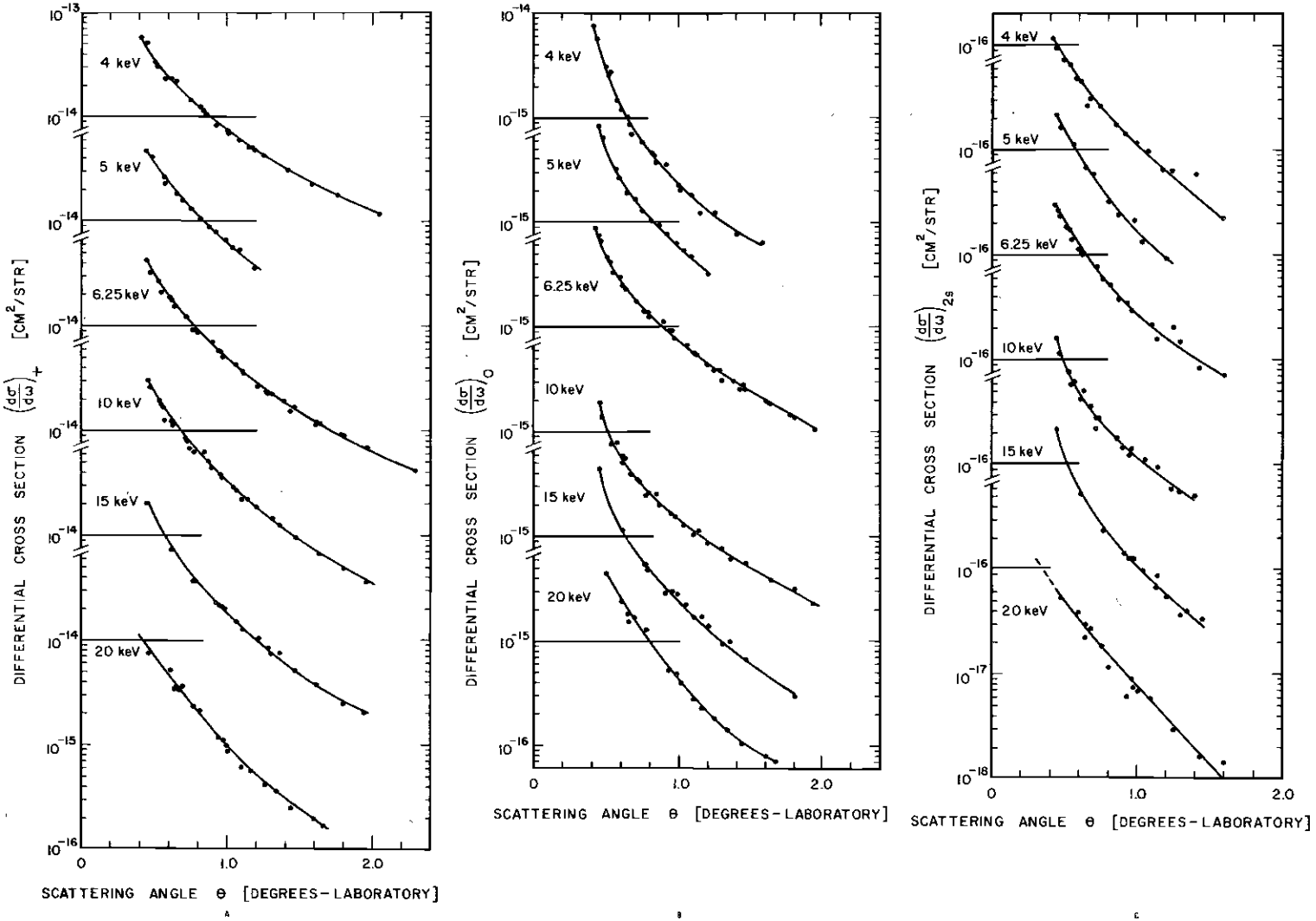

Figure 9 Differential Cross Sections for the Scattering of H^+ by He.
A. Formation of H^+, B. formation of H^0, C. formation of H(2s).
Note broken cross section scale.

not be calculated from the measured flux. However, the ratio of the H(2s) flux to the H^o flux is well defined and was measured for angles down to zero degrees.

As can be seen from Figure 9, all cross sections were smoothly varying functions of the scattering angle, showing no undulations or extraordinary behavior. In general, most sets of data fit curves of the form $k\theta^{-n}$, with n ranging from 2.5 to 3.2 depending on the energy and reaction.

The total differential cross sections and most of the electron capture probabilities presented in the remainder of this chapter were derived from the data presented in Figure 9 by either adding or dividing the appropriate differential cross sections.

It is interesting to consider the possibility of integrating the differential cross sections $(d\sigma/d\omega)_o$ and $(d\sigma/d\omega)_{2s}$ with respect to scattering angle, thus obtaining the total cross section for electron capture into the 2s state, σ_{2s}, and into all states, σ_o. These could then be compared with previously measured total cross sections (see Appendix E for σ_o and Appendix G for σ_{2s}). This procedure is outlined in Chapter II (see equation 25). Unfortunately, the vast majority of the electron capture collisions occurs for impact parameters so large that the laboratory scattering angle was less than 0.4 degree. In fact, usually less than one percent of the total cross section arose from flux scattered through an angle sufficient to be measured in the present apparatus.

Total Differential Cross Section

The total differential cross section, $(d\sigma/ d\omega)_T$, was derived from the data presented in Figure 9 (also Table 1 of Appendix A) by adding $(d\sigma/d\omega)_+$ to $(d\sigma/d\omega)_o$ for each energy and angle. Using this procedure, a system of curves similar to those in Figure 9 was generated. As would be expected from the shapes of $(d\sigma/d\omega)_+$ and $(d\sigma/d\omega)_o$, the total differential cross section curves were smoothly varying functions of angle at each impact energy.

Figure 10 shows $(d\sigma/d\omega)_T$ for the impact energies of 4.0 and 20 keV. Included are various theoretical predictions of classical scattering: the work of Bingham[40] employs a screened Coulomb potential; Smith[41] uses a screened Coulomb potential modified to include shell structure; and the most recent work of Bingham which is based on a static potential (discussed in Chapter III). It was found that, for all impact energies and angles studied in this investigation, the static potential results agreed best with experiment. It should be noted that no attempt has been made to deconvolve the experimental data presented in Figure 10, and any direct comparison of absolute values with theoretical predictions is subject to modification by the finite apparatus resolving power. However, the angular dependence of the differential cross section should be largely free of this effect. The angular dependence of the cross sections calculated with the static potential of Bingham agreed best with the experimental results.

For a fixed energy, the impact parameter and the distance of closest approach vary as the scattering angle is changed. The exact relation-

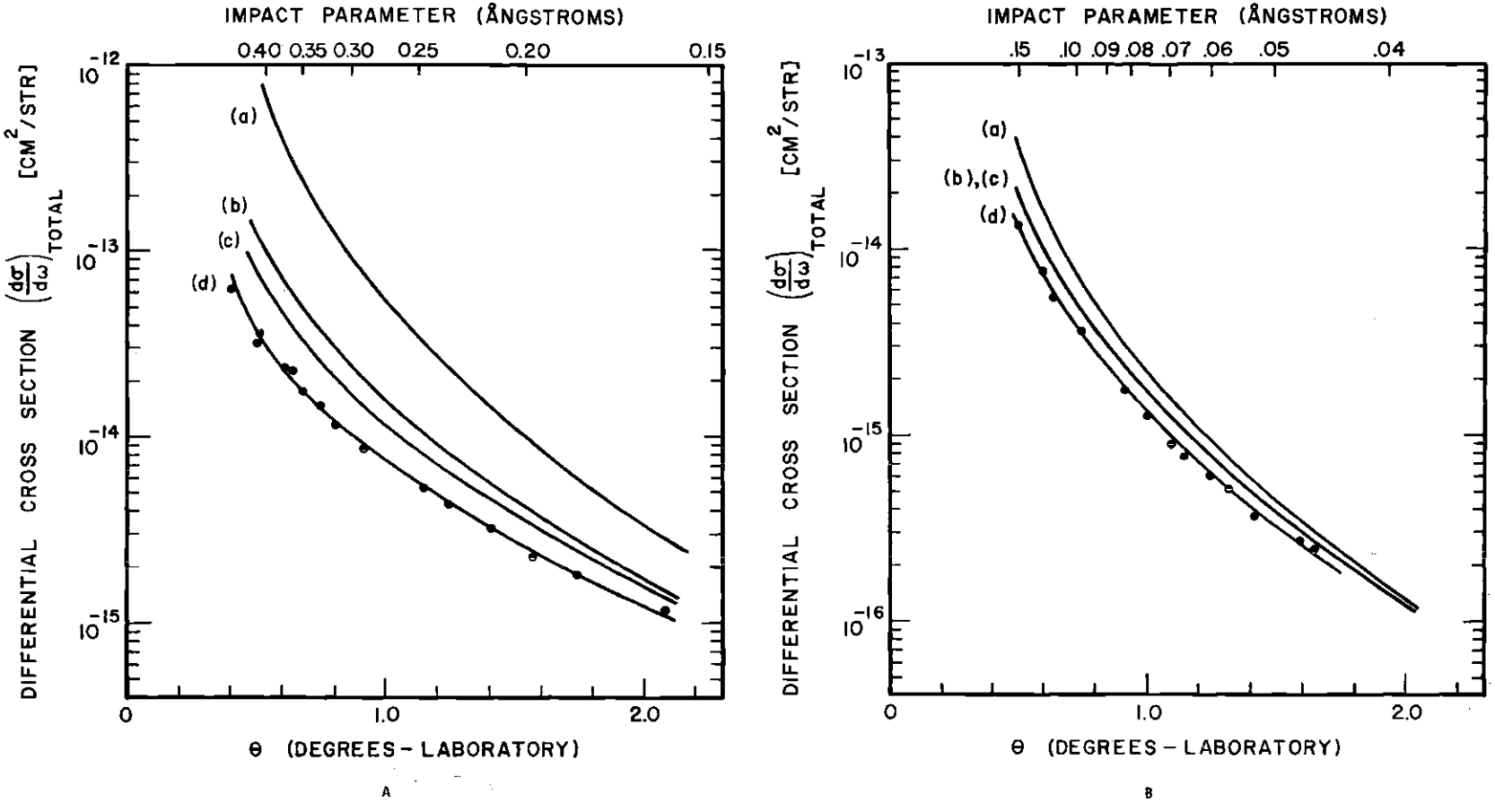

Figure 10 Total Differential Cross Sections for the Scattering of H^+ by He.
A. 4 keV Impact energy; B. 20 keV Impact energy.
Theoretical Calculation using (a) shell potential proposed by Smith [41], (b) screened coulomb potential[40], (c) "static" potential proposed by Bingham (private communication), (d) present experimental results. Impact parameter scale at the top of each graph was evaluated using the screened coulomb potential (see Figure 11).

ship between impact parameter and scattering angle depends on the form of the interaction potential chosen to represent the collision. The impact parameter scale included in Figure 10 and in other figures to be presented in the next section was evaluated using the screened Coulomb potential. For reference purposes, this relation is shown in Figure 11; here the product θE is plotted versus impact parameter.

The only previous measurements of $(d\sigma/d\omega)_T$ for impact energies and scattering angles investigated in this study are those of Crandall.[19] Crandall's data agree well in energy and angular dependence with the present work; however, there is a systematic difference of 40 percent in absolute magnitude (Crandall's data lay above the present data). Crandall estimates a possible systematic error of ± 30 percent for data near one degree. Since the present data are believed accurate to ± 10 percent, the two data sets are comparable.

Electron Capture Probability

Figures 12 and 13 present the measurements of the electron capture probabilities P_o and P_{2s}. The probabilities were defined in Chapter II to be the neutral fraction of the scattered flux (P_o) and the fraction of the scattered flux in the 2s state (P_{2s}).

The data are presented for the fixed scattering angle of one degree and plotted against the reciprocal of the projectile impact velocity. This form of presentation lends itself to comparisons with previous work and in the interpretation of the observed oscillations.

Both P_o and P_{2s} were initially measured as a function of scattering angle. Little variation with angle was observed for scattering

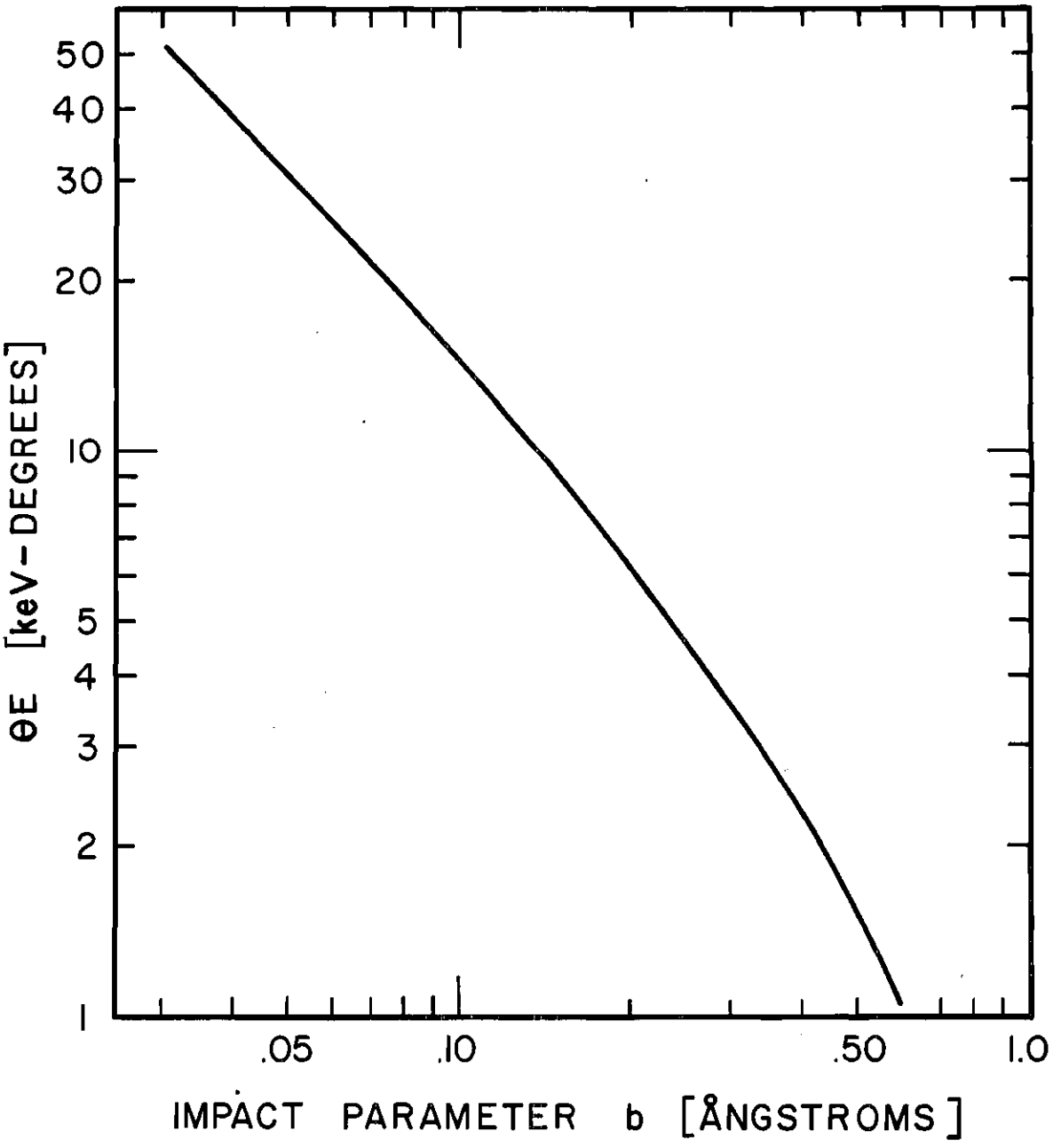

Figure 11 Relation Between θ E and the Impact Parameter for the Screened Coulomb Interaction Potential[40].

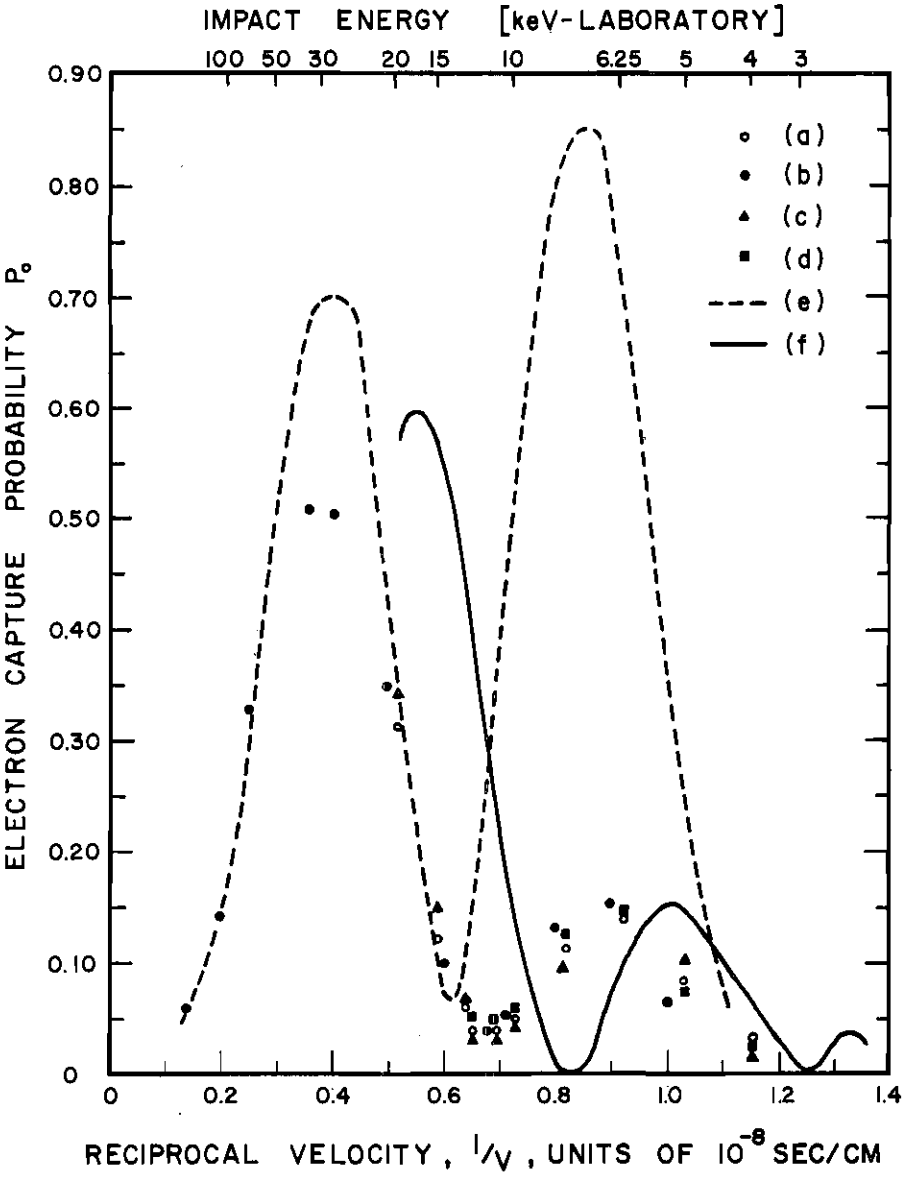

Figure 12 Energy Dependence of P_o. (a) Present Experimental Results for a Fixed Scattering Angle of 1 degree. (b) Experimental Results of Helbig et. al.[18] for a Fixed Value of θ E of 20 keV-degrees. (c) Helbig et. al.[18] for a Fixed Scattering Angle of 1.5 degrees. (d) Helbig et. al.[18] for a Fixed Scattering Angle of 0.7 degrees. (e) Theoretical Results of Sin Fai Lam[47]. (f) Theoretical Results of Colegrave and Stephens[46].

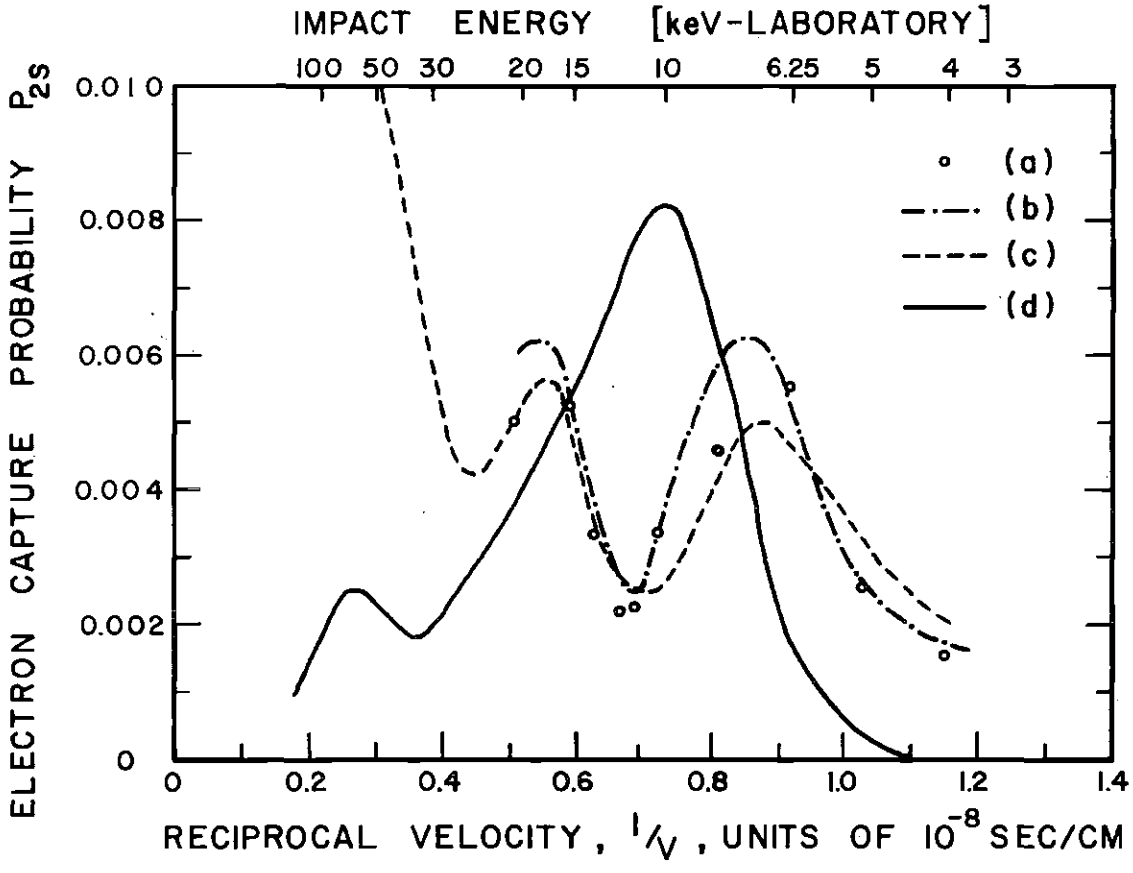

Figure 13 Energy Dependence of P_{2s}. (a) present experimental results for a fixed scattering angle of 1 degree. (b) experimental results of Crandall[19] for a fixed value of θ E of 20 keV-degrees. (c) experimental results of Dose et al.[22] for a fixed scattering angle of 2.2 degrees. (d) theoretical calculation by Sin Fai Lam[47] for a fixed value of θ E of 20 keV-degrees. The data of Dose[22] have been normalized to the present work at 20 keV. Sin Fai Lam[47] calculations have been divided by 10.

angles greater than 0.5 degree. This is in accordance with previous measurements of P_o[18,19] and P_{2s}.[19] Smooth curves were drawn through these data and were used to evaluate P_o and P_{2s} at one degree.* The scatter of data about these curves was approximately ± 10 percent for P_o and ± 20 percent for P_{2s}, becoming somewhat larger for low energies and large scattering angles in the case of P_{2s}.

Included in Figure 12 are previous measurements of P_o by Helbig and Everhart.[18] The present data agree quite well both in absolute magnitude and in the location of the peaks and valleys of the damped oscillation. Previous measurements of P_o have also been made by Crandall[19] but have been omitted for clarity. Crandall's results agree rather well with the present data with the exception of a small discrepancy near 10 keV where the data lay somewhat above both the present results and those of Helbig et al.[18]

The agreement between the data taken at a fixed scattering angle where the impact parameter varies with energy and the data taken for a fixed product of θE (where the impact parameter is essentially constant) is indicative of the fact that, for these angle and energy ranges, P_o is nearly independent of angle.

Two theoretical predictions of the energy dependence of P_o for large-angle scattering are included in Figure 12. The dashed line repre-

*Data for 8, 11, 12, and 13 keV were taken at the fixed scattering angle of one degree. Since only one angle was measured, it was possible to use long counting periods in measuring the 2s flux, and the random error is much less than for the individual points taken in the angle scans at other energies.

sents the results of the four-state impact parameter calculation by Sin Fai Lam.[47] Sin Fai Lam calculated P_o as a function of impact velocity and impact parameter and then employed the screened Coulomb interaction potential to relate impact parameter to scattering angle. The data shown were calculated for a fixed product θE of 20 keV degree which corresponds to a distance of closest approach of 0.076 Å (see Figure 11).

It should be noted that, whereas the experimentally measured P_o includes capture into all states as well as reactions involving target excitation and ionization, the calculated P_o includes only the 1s, 2s, and $2p$ states and does not allow for changes in the target structure.

The four-state calculation predicts the locations of the peaks and valleys in the P_o curve reasonably well but fails to show the strong damping for low energies. It is thought that perhaps the expansion of the total wave function in atomic orbitals may fail to adequately represent the collision at low velocities where the system begins to assume the characteristics of a quasi-molecule.

The solid curve represents the calculations of Colegrave and Stephens,[46] who used a two-state molecular orbital expansion. These states should represent the system more accurately as the impact energy is decreased. The results of the molecular expansion fail to accurately predict the location of the peaks and valleys, but the damped nature of the oscillation is clearly shown.

It is of interest to consider how the large angle P_o data can show such interesting oscillatory behavior when the total cross section σ_o is a smoothly varying function of energy (see Appendix D). The reason for

this is that only approximately one percent of the electron capture cross section is attributable to these large-angle collisions. Thus the energy dependence of σ_o will be similar to that of large impact parameter collisions and not directly relatable to large-angle cross sections.

The measurements of P_{2s} are presented in Figure 13 along with the previous experimental results of Dose[22] and Crandall.[19] The data of Dose[22] were taken for the fixed scattering angle of 2.2 degrees. Dose's data have been normalized to the present data at 20 keV because the technique used to evaluate the absolute detection efficiency of the 2s detector must be considered suspect (see Chapter III). The data were multiplied by a factor of 2.5 for this normalization. The energy dependence of P_{2s} agrees well with the present work.

Crandall[19] presents P_{2s} for a fixed θE value of 20 keV degrees. There is general agreement both in absolute value and energy dependence with the present work. Crandall[19] also presented data for other values of θE, but these have been excluded for purposes of clarity. There was little systematic difference between the several sets of data.

The solid curve in Figure 13 represents the calculations of P_{2s} by Sin Fai Lam.[47] This is the only theoretical prediction of P_{2s} known to the author. In general, the agreement with experiment is not good. First, the predicted P_{2s} is a factor of 10 too large. Second, the positions of the peaks and valleys are not located properly. Third, the relative spacing between the peaks does not agree with experiment.

Since P_{2s} shows oscillatory structure similar to that found in P_o, it is of interest to employ the quasi-molecular interpretation and the

semi-empirical equations discussed in Chapter III. The spacing of peaks is approximately 0.30×10^{-8} sec/cm. Using equation (37), an effective value of the product of the separation energy and the interaction length, <VR>, is 137 eV Angstroms. This is considerably higher than the 84 eV Angstrom value for the P_o curve. This might be expected since the separation energy for the 2s state is larger than that for the 1s state (see Figure 15). Using 137 eV Angstrom for <VR> in equation (40) and assuming a phase factor of $\pi/4$, as was found for the P_o data, one finds that the empirical formula predicts peaks at 89, 16, and 6.7 keV and valleys at 32 and 10 keV. These predictions are in agreement with the available experimental data.

It is interesting to note that the low-energy peak in P_{2s} occurs at the same impact energy (6.25 keV) as does the low-energy peak in P_o. It has been suggested[19] that the peak in the 2s data is the result of a two-step process as described by Polvektov and Presnyakov[48] (see equation (36)). A similar effect may be seen in the total cross section measurements of σ_o (Appendix D) and σ_{2s} (Appendix G). σ_{2s} shows a shoulder near 10 keV which has an energy dependence quite similar to that of σ_o.

Metastable Content of the Neutral Flux

The fractional metastable content of the scattered neutral flux was measured as a function of scattering angle for several impact energies. For angles outside the projectile beam this fraction was calculated by forming the ratio $(d\sigma/d\omega)_{2s}/(d\sigma/d\omega)_o$. For smaller angles, where the differential cross section was not meaningful, the fraction was calculated

from the ratio of scattered currents.

Figure 14 shows the results of these measurements. The solid lines represent lines of best fit to the data points (which have been omitted for clarity). The scatter of data about these lines ranged from about ± 10 percent for small angles, where the 2s statistical fluctuations were low, to ± 30 percent at the large angles. The dashed lines are the results of a test which is described below.

As the scattering angle was reduced, the fractional content was found to decrease by an amount which depended on the impact energy. This factor ranged from 12 at 4 keV to 1.25 at 20 keV.

The point where this decrease occurred moved toward smaller angles as the energy was increased until it coincided with the edge of the primary beam. It then ceased to move inward as the impact energy was increased further. This behavior created doubt concerning whether the fall in the fractional metastable content was real or merely an apparatus effect caused by admission of part of the primary beam through the scattered flux collimators.

To resolve this question, the beam diameter was reduced from approximately 0.1 cm to 0.03 cm and the low-angle data repeated. If the decrease were an apparatus effect, it should move inward in angle since the beam was now narrower. The dashed lines in Figure 14 indicate the result of this test. It was found that the fall in the fractional content at 4 keV was not an apparatus effect. For 6.25 keV and above, the angle at which the fall occurred changed by an amount correlatable with the decrease in beam size.

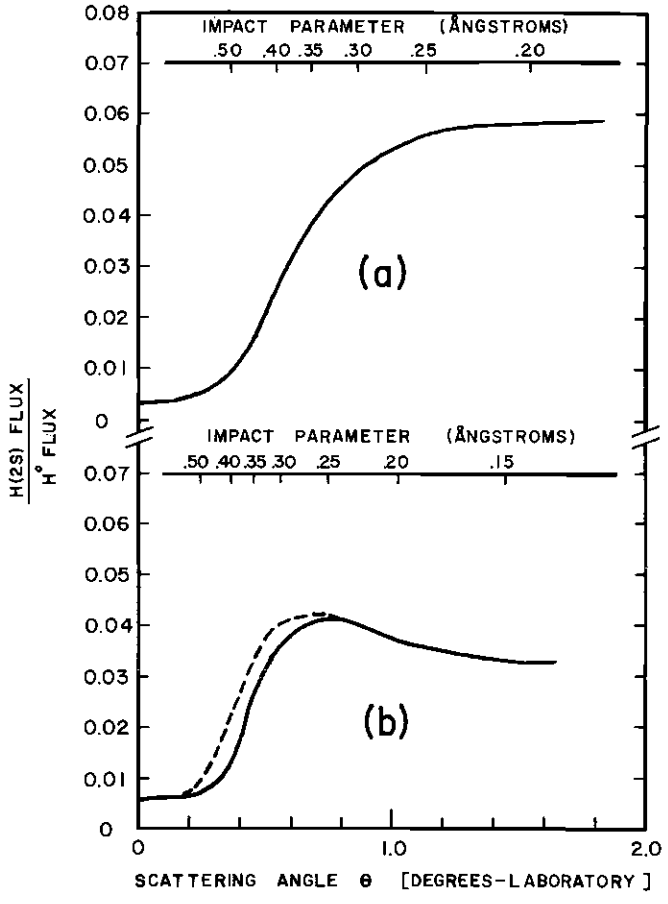

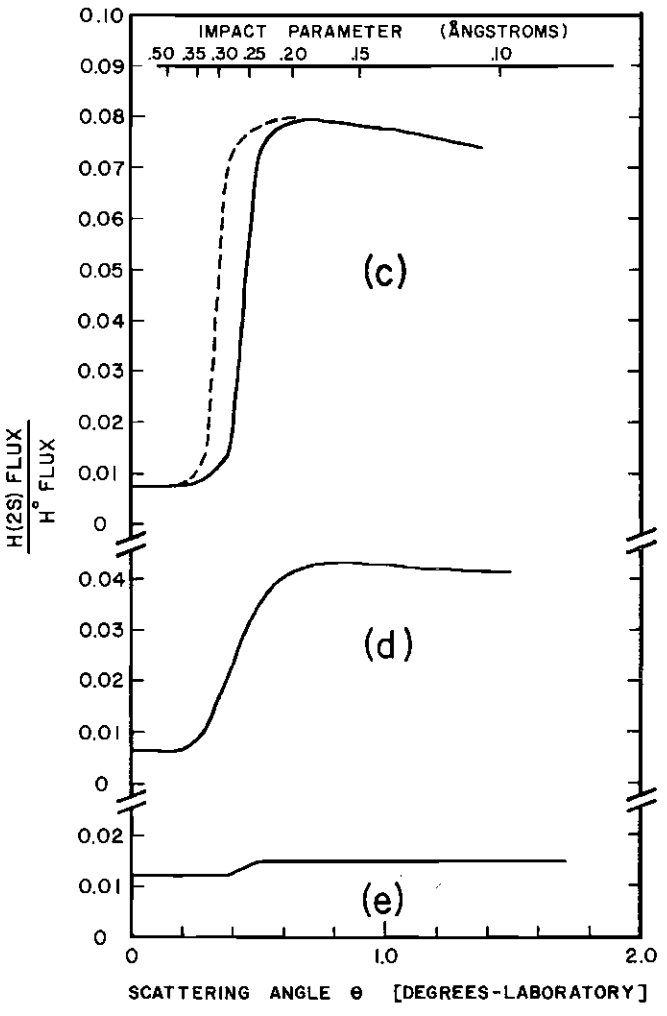

Figure 14 Fractional Metastable Content of the Scattered Neutral Flux. Angular dependence is shown for Impact Energies of (a) 4 keV, (b) 6.25 keV, (c) 10 keV, (d) 15 keV and (e) 20 keV. The solid lines are smooth curves through data taken with the 0.10 diameter beam. The dashed lines are smooth curves through data taken with a 0.03 cm wide beam. For 4 keV impact energy, the two curves coincided and are shown as a single solid curve.

This effect may be understood by considering the following. First, it may be assumed that if the fractional content at large angles is much greater that the ratio of the total cross section σ_{2s} and σ_{o} (which it is for energies between 4 and 15 keV), then there must be some angle at which the fraction decreases. If this were not the case, the ratio of the total cross sections could not be different from this fraction. Next, assume that the angle for which this break occurs is small. Now as the scattering angle is reduced and a portion of the primary beam is admitted through the collimators, some flux which has been scattered through the angles between zero and the break angle will be admitted. Since the differential cross section for scattering is a very rapidly increasing function of angle, this flux overwhelms that which has been scattered at the angle set on the rotating arm. Thus as soon as a portion of the beam is admitted, the fractional content quickly assumes the characteristics of the straight-ahead or zero-degree position.

One interpretation of the fall as measured for 4 keV is based on the molecular energy levels for the HeH^{+} molecule as calculated by H. H. Michels.[51] These curves are presented in Figure 15.

For large impact parameters (and thus small scattering angles) the energy difference between the $He(1s^2) + H^{+}$ curve and the $He^{+}(1s) + H(2s)$ curve (A) is approximately twice that between the $He(1s^2) + H^{+}$ curve and the $He^{+}(1s) + H(1s)$ curve (B). It would be expected that electron capture into the 1s state would predominate for small-angle collisions. However, as the impact parameter is reduced, the energy difference between the curves A and B decreases. For large-angle scattering, the energy

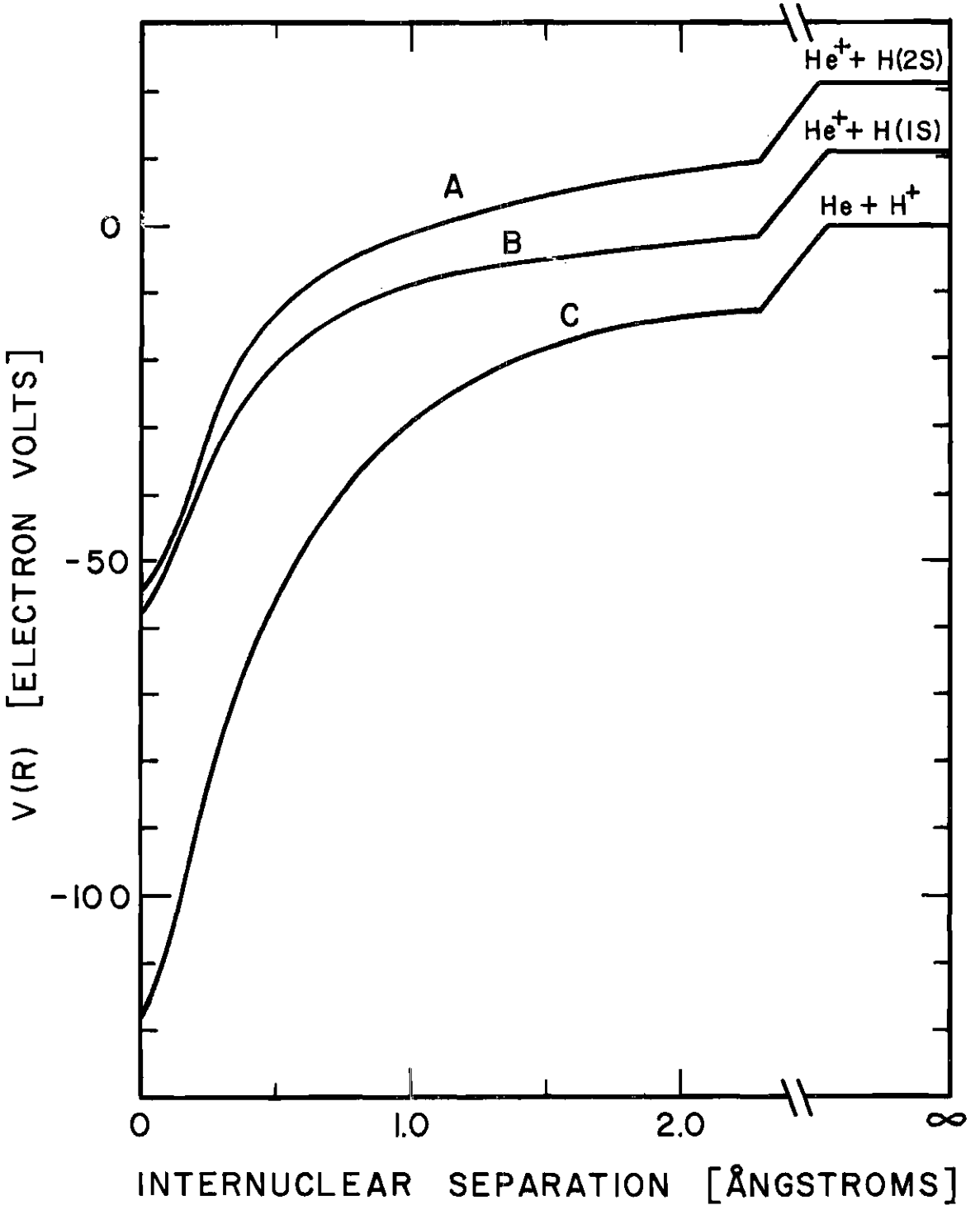

Figure 15 Potential Energy Curves for the He H^+ Molecular Ion. These curves were drawn from the calculations of H. H. Michels.(51)

difference is sufficiently small that it might be expected that the capture probability for the 2s state would become comparable to that for the 1s state. The data presented in Figure 14 indicate that the fractional content of metastables increases with a reduction in impact parameter, to as much as 10 percent of the neutral flux.

An impact parameter scale has been included on the 4-keV graph of Figure 14. Although the break in the curve is not very well defined, it appears to occur for the range of impact parameter between 0.3 and 0.35 Å From Figure 15 it is seen that the difference between the curves A and B becomes small in this same region.

The calculations of Sin Fai Lam[47] were presented in such a manner that the impact parameter dependence of the ratio $P_{2s}/(P_{1s} + P_{2s} + P_{2p})$ could be evaluated for the impact energy of 6.25 keV. Figure 11 was then used to assign a scattering angle to each impact parameter value. Figure 16 shows the results of this calculation compared to the present data. Here the small-angle data were taken with the narrow beam. The narrow spike in the theoretical curve would not be observable in the experimental data due to the finite apparatus resolution.

The agreement with experiment in both shape and magnitude is somewhat striking and unexpected since neither P_o nor P_{2s} individually agrees with experiment at this energy.

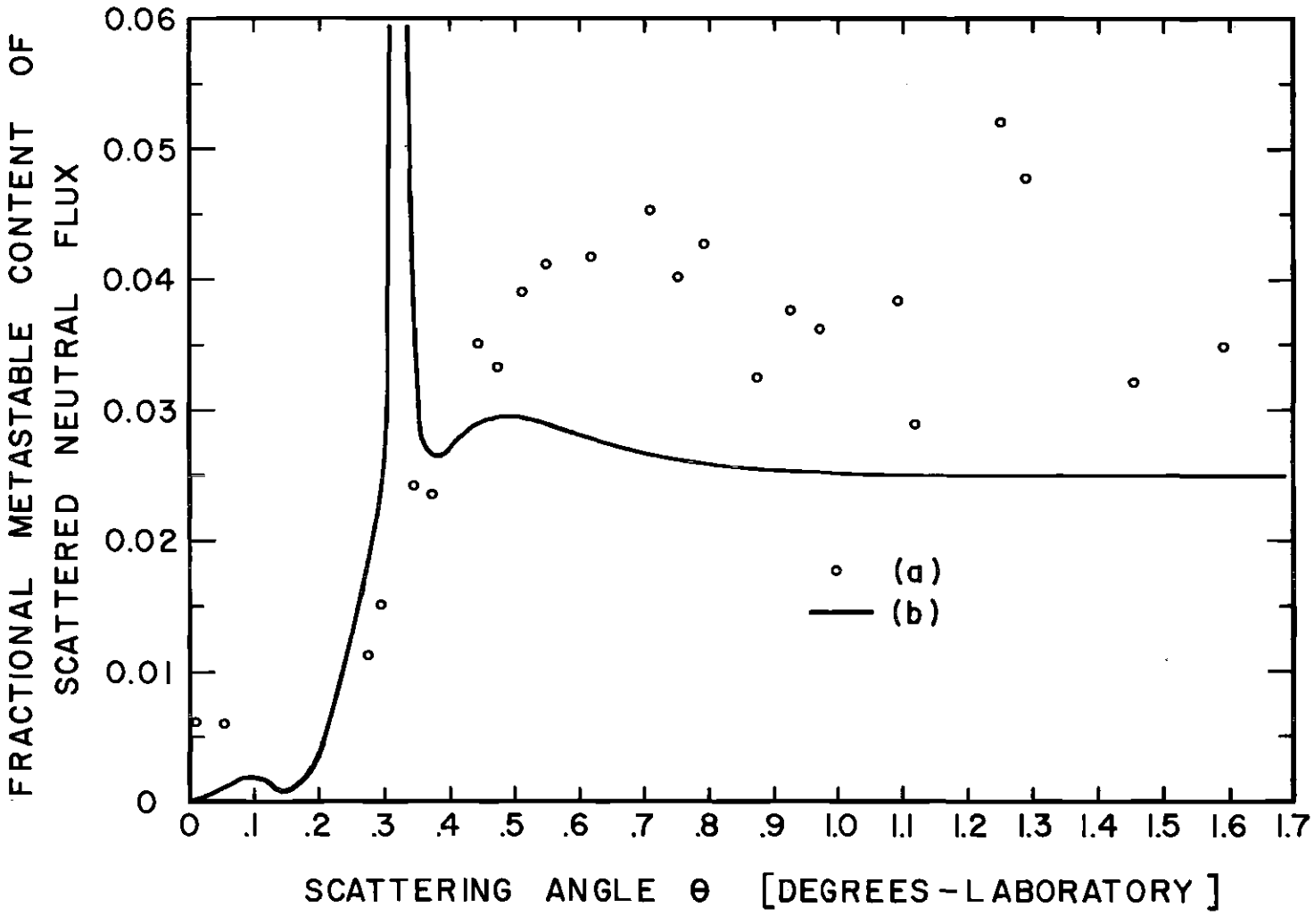

Figure 16 Metastable Fractional Content of Scattered Neutral Flux for 6.25 keV Impact Energy. (a) Present Data. (b) Calculation by Sin Fai Lam[47]. Theoretical Calculation Represents the Ratio $P_{2s}/(P_{1s} + P_{2s} + P_{2p})$.

CHAPTER VII

DISSOCIATION RESULTS AND DISCUSSION

The results of the dissociation experiment are presented in Figures 17, 18, and 19. Figure 17 presents the angle and energy dependence of the differential cross sections for the formation of H^+, H^o, and H(2s) via a collision between H_2^+ and He. Figures 18 and 19 present similar cross sections for the single energy of 10 keV for collisions between H_2^+ and H_2 (Figure 18) and H_3^+ and H_2 (Figure 19).

Although the identification of the scattered H(2s) flux was unambiguous, the identification of the scattered ion flux as H^+ and the scattered neutral flux as H^o is based on previously published results. Using mass-sensitive detectors, the angular dependence of scattered H_2^+ and H_2 has been measured by McClure[54] (H_2) and Fedorenko et al.[58] (H_2^+). These studies indicate that the scattered H_2^+ flux and the H_2 flux are confined to angles of less than approximately 0.1 degree. Flux scattered by angles greater than this consisted entirely of protons and hydrogen atoms.

No similar studies of the angular distribution of scattered H_2^+, H_2, and H_3^+ for H_3^+ projectiles have been performed for small scattering angles*. Ziemba et al.[2] found that, at 5 degrees, the scattered flux was composed entirely of H^+ and H^o. In the analysis of the data presented in

*There is no evidence for the existence of H_3.[61]

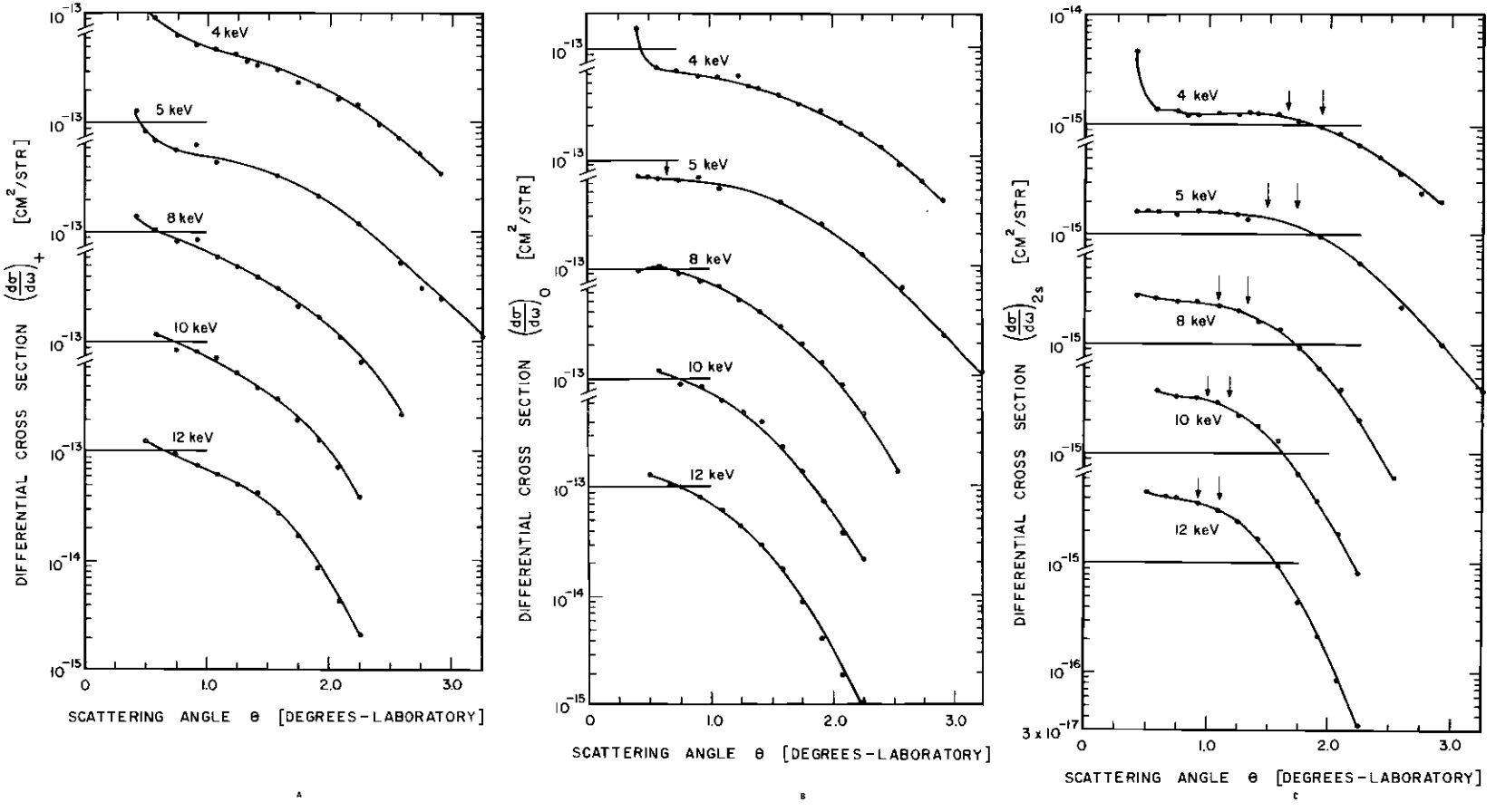

Figure 17 Differential Cross Sections for the Scattering of H_2^+ by He. A. formation of H^+, B. formation of H^O, C. formation of H(2s). (Note broken cross section scale).

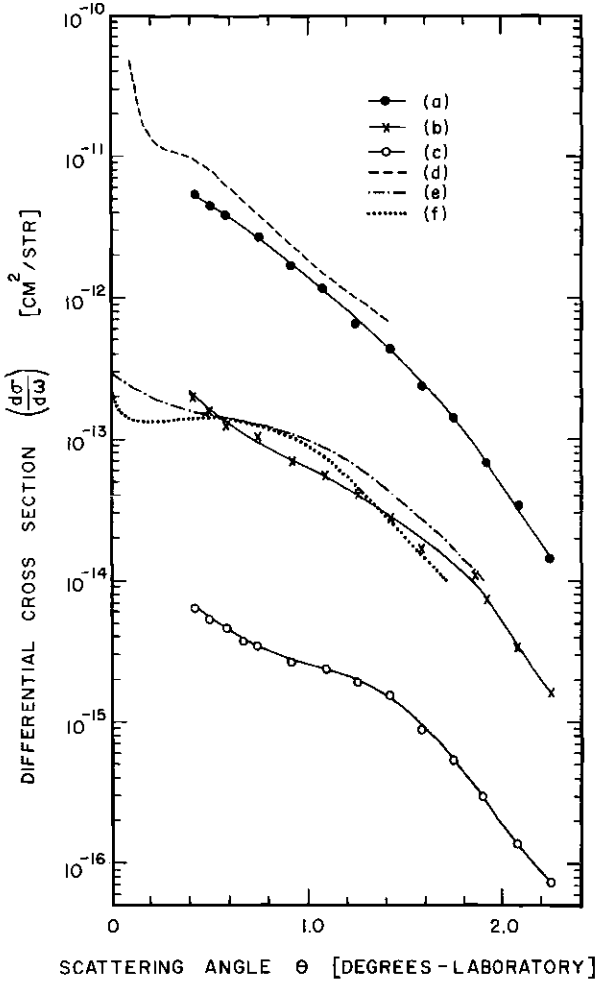

Figure 18 Differential Cross Sections for the Scattering of H_2^+ by H_2. (a) present results for the formation of H(x10), (b) present results for the formation of H^+, (c) present results for the formation of H(2s), (d) results of McClure[54] for the formation of H(x10), (e) results of McClure[54] for the formation of H^+, (f) theoretical results of McClure[54] for the formation of H^+.

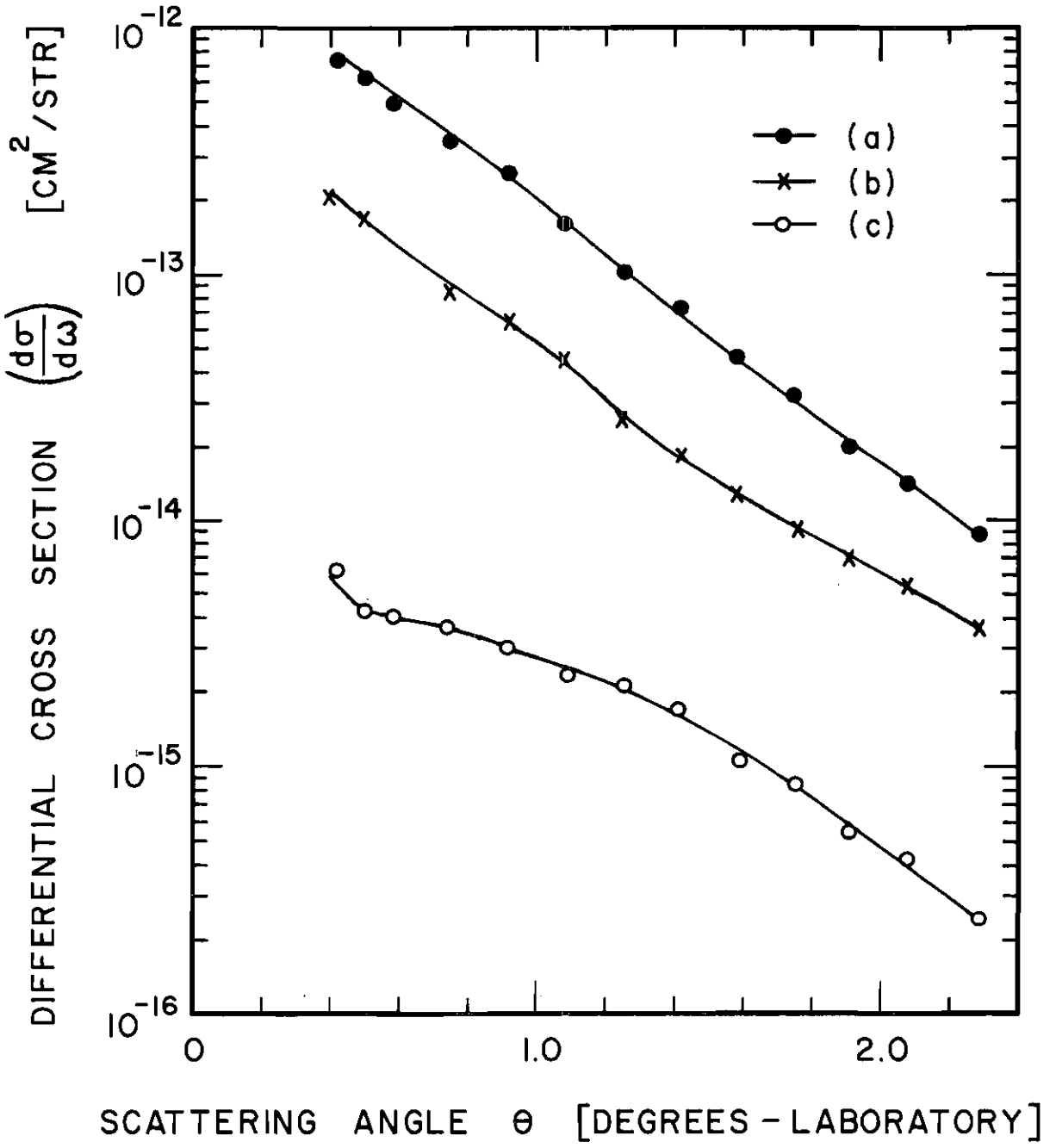

Figure 19 Differential Cross Sections for the Scattering of H_3^+ by He. (a) formation of H^o, (b) formation of H^+, (c) formation of H(2s).

Figure 19, it has been assumed that this result is true for angles down to 0.4 degree. If this assumption is invalid, the $(d\sigma/d\omega)_+$ and $(d\sigma/d\omega)_o$ data would have to be re-evaluated accordingly. However, as was the case for H_2^+ projectiles, the identification of the scattered H(2s) flux is unambiguous.

In the evaluation of the scattered H^+ and H^o currents, the secondary emission coefficient appropriate to the energy of the scattered particle was employed. This meant that flux scattered from a 10-keV H_2^+ beam was analyzed using the values of γ_+ and γ_o corresponding to an impact energy of 5 keV. Similarly, for a 10-keV H_3^+ beam, values of γ_+ and γ_o corresponding to an impact energy of 3.33 keV were used.

The following discussion of the H_2^+ data will be based on the dissociation interpretation discussed in Chapter III. There it was pointed out that McClure[54] has suggested that, when the H_2^+ ion passes the target atom (or molecule), it is excited to an anti-bonding state, and the two nuclei move apart with a certain relative velocity. The magnitude of this velocity depends on (a) the particular anti-bonding state involved and (b) the internuclear separation at the time of excitation.

It was also pointed out in Chapter III that one result of this dissociation interpretation is the fact that the dissociation products cannot appear at scattering angles larger than $\sqrt{Q/E}$, where Q is the energy gained by each nucleus due to the dissociation and E is the H_2^+ energy. However, the differential cross section need not show a marked change at one particular angle for four reasons. First, several anti-bonding states may participate, each with its own maximum angle. This would tend to smear

out any sharp break in the data. Second, the cross section for excitation may be severely peaked in the forward direction. Third, other collision processes may have comparable differential cross sections (for example, quasi-elastic or electron capture scattering). Fourth, the existence of an appreciable fraction of vibrationally excited primary projectiles would yield a distribution of Q values.

To aid in interpreting the data presented in this chapter, the potential energy curves[70] and correlation diagram[63] for H_2^+ are presented in Figure 20.

The data of Figure 17 indicate that, for collisions between H_2^+ and He, all three differential cross sections demonstrate a change in slope which may be interpreted as the cut-off angle above which dissociation products cannot appear.

The data presented in the previous chapter showed that the quasi-elastic and charge transfer differential cross sections are to two orders of magnitude below these data; thus these reactions should not interfere with the interpretation of the dissociation data.

The break in the 2s data is better defined than in the H^+ and H^o data. This may be due to a difference in the dependence of the cross sections on the H_2^+ orientation angle Φ. It could also be due to the fact that there are only two anti-bonding states leading to the 2s state ($2s\ \sigma_g$ and $3p\ \sigma_u$), while there are many anti-bonding states which lead to the production of H^+ or H^o.

The arrows shown in the 2s graph of Figure 17 indicate the position of the calculated break angle for the $2s\ \sigma_g$ and $3p\ \sigma_u$ states. In order

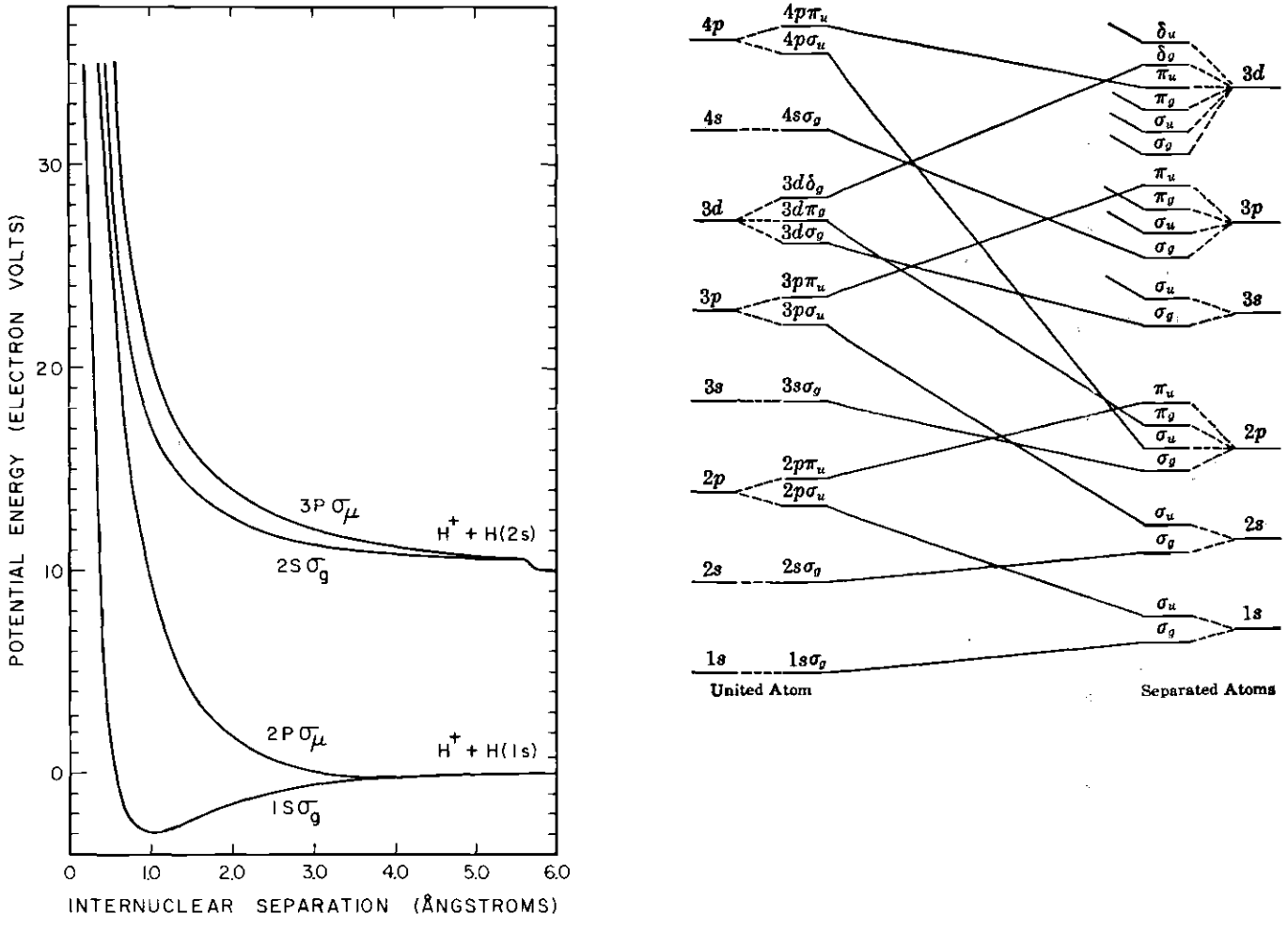

Figure 20 Potential Energy Curves and Correlation Diagram For H_2^+.

to evaluate Q, it was assumed that the transition occurred for the internuclear separation which corresponded to the minimum in the H_2^+ $1s\sigma_g$ curve. The break in the 2s data is seen to move toward smaller scattering angles approximately as $1/\sqrt{E}$.

The data shown in Figures 18 and 19 have been included primarily for the purpose of comparison to the H_2^+ + He data and to the only other published angular scans of dissociation products.

The agreement in absolute value with the H^+ and H^o data of McClure[54] is reasonable considering the very different means of detector calibration employed. The agreement in angular dependence is also good, with some difference in the low-angle H^+ data. Since a theoretical prediction of a dissociation cross section requires the knowledge of the population of the vibrational states and this distribution was unknown for the present data, the theoretical curve presented in Figure 18 must be considered as qualitative. This curve was in fact normalized to the data of McClure[54] at 0.8 degree.

For the H_2^+ + H_2 data, it is seen that the H^o differential cross section exhibits little or no break; the H^+ cross section shows some break; while the H(2s) data are quite similar both in magnitude and in the location of a well defined break to the H(2s) data of Figure 17.

From Figure 19 it is seen that, although the magnitudes of the three cross sections are similar to the H_2^+ + H_2 data, none of the H_3^+ data show a well defined break. This may be due to a dissociation process that is different from that described for the H_2^+ ion.

The probabilities P_o, P_{2s}, and P_{2s}/P_o were formed for the data

shown in Figures 17, 18, and 19.

P^o was found to be fairly independent of angle and had the value 0.5 for $H_2^+ + He$, 0.75 for $H_2^+ + H_2$, and 0.8 for $H_3^+ + H_2$. P_{2s} and P_{2s}/P_o increased as the scattering angle was increased. P_{2s}/P_o varied from 1 to 5 percent, while P_{2s} was between 1 and 3 percent. Although the dissociation differential cross section for production of H(2s) was much larger than that for electron capture, the metastable fractional constant was not as large.

Gibson and Los[60] discuss the problem of which anti-bonding states participate in the dissociation process. They point out that the assumption made by McClure[54] that the number of excitations to the 2p σ_u state overshadows the number to all higher states may not be correct. Measurements of the total cross section (using an He target) for excitation to the six states leading to the production of L_α radiation by Van Zyl et al.[71] indicate that, at 10 keV, these higher states may account for 30 percent of the total dissociation cross section.[84]

The present results are a direct measurement of the importance of the two levels leading to the 2s state. The metastable fraction of the neutral flux produced in the dissociation of 10 keV H_2^+ by an He target was found to vary from 3 percent at 0.5 degree to a maximum of 5 percent at 1.6 degrees. For larger angles the fraction decreased.

Since the 2s state represents only one third of the possible n = 2 levels and there are 12 n = 3 levels, it is quite possible that anti-bonding states other than 2p σ_u play an important part in the H_2^+ dissociation process.

APPENDIX A

DATA TABLES

Data Table 1. Differential Cross Sections for Formation of H^+, H^o, and H(2s) by Charge Transfer

Projectile: H^+

Target: He

θ: Angle in Degrees (Laboratory)

$\left(\frac{d\sigma}{d\omega}\right)_+$: Cross Section for H^+ Production in cm^2/steradian

$\left(\frac{d\sigma}{d\omega}\right)_o$: Cross Section for H^o Production in cm^2/steradian

$\left(\frac{d\sigma}{d\omega}\right)_{2s}$: Cross Section for H(2s) Production in cm^2/steradian

θ	$\left(\frac{d\sigma}{d\omega}\right)_+$ (10^{-13})	$\left(\frac{d\sigma}{d\omega}\right)_o$ (10^{-13})	$\left(\frac{d\sigma}{d\omega}\right)_{2s}$ (10^{-15})	θ	$\left(\frac{d\sigma}{d\omega}\right)_+$ (10^{-13})	$\left(\frac{d\sigma}{d\omega}\right)_o$ (10^{-13})	$\left(\frac{d\sigma}{d\omega}\right)_{2s}$ (10^{-15})
	E = 4.00 keV						
0.417	0.564	0.077	0.114	0.817	0.127	0.00453	---
0.456	0.513	0.0579	0.0927	0.833	0.115	0.00443	---
0.500	0.334	0.0309	0.0737	0.850	0.108	0.00365	0.0178
0.517	0.304	0.0257	---	0.917	0.083	0.00350	0.0144
0.533	0.326	0.0269	0.0641	1.00	0.0731	0.00223	---
0.583	0.233	0.0152	0.0466	1.01	0.0697	0.00200	0.0115
0.617	0.232	0.0121	0.0457	1.08	0.0595	0.00186	0.00973
0.65	0.223	0.0105	---	1.15	0.0510	0.00121	---
0.667	0.183	0.00882	0.0263	1.16	0.0510	0.00122	---
0.683	0.166	0.00711	0.0304	1.18	0.0493	---	0.00640
0.75	0.143	0.00586	0.0269	1.25	0.0435	0.00123	0.00641

continued in next column

continued on next page

θ	$\left(\frac{d\sigma}{d\omega}\right)_+$	$\left(\frac{d\sigma}{d\omega}\right)_o$	$\left(\frac{d\sigma}{d\omega}\right)_{2s}$	θ	$\left(\frac{d\sigma}{d\omega}\right)_+$	$\left(\frac{d\sigma}{d\omega}\right)_o$	$\left(\frac{d\sigma}{d\omega}\right)_{2s}$
	(10^{-13})	(10^{-13})	(10^{-15})		(10^{-13})	(10^{-13})	(10^{-15})
1.41	0.0308	0.000760	0.00604	0.450	0.424	0.0748	0.264
1.58	0.0222	0.000640	0.00224	0.467	0.320	0.0664	0.231
1.75	0.0179	---	---	0.517	---	0.0455	0.181
2.08	0.0119	---	---	0.533	0.264	0.0417	0.176
	E = 5.00 keV			0.550	0.209	0.0336	0.138
0.450	0.451	0.0856	0.213	0.600	0.186	0.0306	0.115
0.483	0.416	0.0647	0.163	0.617	0.174	0.0249	0.109
0.567	0.263	0.0328	0.115	0.633	0.151	0.0237	0.100
0.583	0.225	0.0273	---	0.717	0.110	0.0174	0.0795
0.650	0.178	0.0197	0.0688	0.767	0.0958	0.0140	0.0568
0.700	0.157	0.0172	0.0595	0.783	0.0938	0.0139	---
0.750	0.130	0.0132	---	0.800	0.0861	0.0125	0.0540
0.817	0.109	0.0105	0.0319	0.883	0.0702	0.0112	0.0365
0.867	0.0867	0.00944	0.0244	0.933	0.0587	0.00906	0.0344
0.917	0.0789	0.00779	---	0.950	0.0573	0.00908	---
0.983	0.0654	0.00642	0.0217	0.967	0.0511	0.00793	0.0289
1.03	0.0563	0.00535	0.0134	1.05	0.0421	0.00676	---
1.08	0.0522	0.00467	---	1.10	0.0362	0.00570	0.0220
1.20	0.0357	0.00323	0.00930	1.11	0.0350	0.00574	---
	E = 6.25 keV			1.13	0.0365	0.00557	0.0160
0.433	0.433	0.0898	0.303	1.21	0.0262	0.00430	---

continued in next column

continued on next page

θ	$\left(\frac{d\sigma}{d\omega}\right)_+$	$\left(\frac{d\sigma}{d\omega}\right)_o$	$\left(\frac{d\sigma}{d\omega}\right)_{2s}$	θ	$\left(\frac{d\sigma}{d\omega}\right)_+$	$\left(\frac{d\sigma}{d\omega}\right)_o$	$\left(\frac{d\sigma}{d\omega}\right)_{2s}$
	(10^{-13})	(10^{-13})	(10^{-15})		(10^{-13})	(10^{-13})	(10^{-15})
1.26	0.0238	0.00387	0.0203	0.550	0.171	---	---
1.28	0.0233	0.00381	---	0.567	0.124	0.00796	0.0605
1.30	0.0222	0.00307	0.0147	0.608	0.123	0.00583	---
1.38	0.0191	0.00305	---	0.617	0.112	0.00512	0.0428
1.43	0.0154	0.00255	0.00824	0.633	---	0.00571	0.0504
1.45	0.0165	0.00277	---	0.675	0.103	0.00381	0.0369
1.46	0.0166	0.00253	---	0.708	0.0845	0.00360	0.0217
1.60	0.0113	0.00199	0.00703	0.717	0.793	0.00358	0.0285
1.61	0.0119	0.00198	---	0.733	0.0665	0.00350	0.0277
1.63	0.0118	0.00183	---	0.775	0.0621	0.00243	---
1.78	0.00918	0.00142	---	0.800	0.0674	0.00258	---
1.80	0.00902	0.00136	---	0.842	0.0620	0.00252	0.0179
1.96	0.00694	0.00106	---	0.867	0.0507	0.00200	---
2.30	0.00428	0.000620	---	0.883	0.0440	---	---
	E = 8.00 keV			0.900	---	---	0.0146
1.00	0.0384	0.00470	0.0196	0.950	0.0378	0.00168	0.0121
	E = 10.0 keV			0.967	0.0352	0.00162	0.0137
0.450	0.303	0.0197	0.161	1.03	0.0282	0.00131	---
0.467	0.258	0.0140	0.114	1.06	0.0262	---	0.0111
0.533	0.195	0.00777	0.0761	1.10	0.0220	0.00105	---
0.542	0.171	0.00791	0.9578	1.13	0.0221	0.00113	0.00943

continued in next column

continued on next page

θ	$\left(\frac{d\sigma}{d\omega}\right)_+$	$\left(\frac{d\sigma}{d\omega}\right)_o$	$\left(\frac{d\sigma}{d\omega}\right)_{2s}$	θ	$\left(\frac{d\sigma}{d\omega}\right)_+$	$\left(\frac{d\sigma}{d\omega}\right)_o$	$\left(\frac{d\sigma}{d\omega}\right)_{2s}$
	(10^{-13})	(10^{-13})	(10^{-15})		(10^{-13})	(10^{-13})	(10^{-15})
1.20	0.0187	0.000892	---	0.950	0.0210	---	0.0124
1.23	---	---	0.00581	0.967	0.0207	0.00287	0.0125
1.30	0.0148	0.000760	0.00545	0.983	0.0202	0.00285	0.0128
1.36	0.0122	0.000625	---	1.05	0.0150	0.00220	0.00959
1.40	---	---	0.00514	1.11	0.0127	---	---
1.46	0.00969	0.000558	---	1.13	0.0127	0.00169	0.00659
1.63	0.00676	0.000388	---	1.15	0.0111	0.00164	0.00806
1.80	0.00487	0.000317	---	1.20	0.0103	0.00139	0.00538
1.96	0.00360	0.000227	---	1.28	0.00849	---	---
	E = 11.0 keV			1.31	0.00747	0.000977	0.00360
1.00	0.0285	0.00113	0.00670	1.36	0.00756	0.000986	0.00396
	E = 12.0 keV			1.46	0.00522	0.000667	0.00336
1.00	0.0276	0.00111	0.00630	1.61	0.00379	---	---
	E = 13.0 keV			1.80	0.00248	0.000305	0.000536
1.00	0.0239	0.00151	0.00845	1.95	0.00205	---	---
	E = 15.0 keV				E = 20.0 keV		
0.450	0.198	0.0460	0.220	0.475	0.0758	---	0.0533
0.617	0.0730	0.0119	0.0520	0.500	0.0887	0.0430	---
0.767	0.0363	0.00540	0.0226	0.600	0.0514	0.0247	0.0386
0.783	0.0362	0.00467	---	0.642	0.0351	---	0.0222
0.917	0.0226	0.00289	0.0137	0.650	0.0363	0.0185	0.0296

continued in next column

continued on next page

θ	$\left(\frac{d\sigma}{d\omega}\right)_+$	$\left(\frac{d\sigma}{d\omega}\right)_o$	$\left(\frac{d\sigma}{d\omega}\right)_{2s}$
	(10^{-13})	(10^{-13})	(10^{-15})
0.667	0.0347	0.0157	---
0.683	0.0355	0.0170	0.0267
0.767	0.0233	0.0131	0.0180
0.808	0.0214	---	0.0117
0.933	0.0120	0.00521	0.00601
0.975	0.0110	---	0.00870
0.983	0.00962	0.00482	0.00728
1.01	0.00854	0.00396	0.00678
1.10	0.00606	0.00293	0.00582
1.16	0.00558	0.00226	---
1.26	0.00419	0.00179	0.00292
1.33	0.00361	0.00148	---
1.43	0.00254	0.00107	0.00161
1.60	0.00197	0.000785	0.00143
1.66	0.00176	0.000746	---

Data Table 2. Differential Cross Sections for Formation of H^+, H^o, and H(2s) by Dissociation

Projectile: H_2^+

Target: He

θ: Angle in Degrees (Laboratory)

$\left(\frac{d\sigma}{d\omega}\right)_+$: Cross Section for H^+ Production in cm^2/steradian

$\left(\frac{d\sigma}{d\omega}\right)_o$: Cross Section for H^o Production in cm^2/steradian

$\left(\frac{d\sigma}{d\omega}\right)_{2s}$: Cross Section for H(2s) Production in cm^2/steradian

θ	$\left(\frac{d\sigma}{d\omega}\right)_+$	$\left(\frac{d\sigma}{d\omega}\right)_o$	$\left(\frac{d\sigma}{d\omega}\right)_{2s}$	θ	$\left(\frac{d\sigma}{d\omega}\right)_+$	$\left(\frac{d\sigma}{d\omega}\right)_o$	$\left(\frac{d\sigma}{d\omega}\right)_{2s}$
	(10^{-13})	(10^{-13})	(10^{-15})		(10^{-13})	(10^{-13})	(10^{-15})
	E = 4.00 keV			1.58	0.291	0.379	1.22
0.417	---	1.54	4.63	1.75	0.233	0.301	1.04
0.583	0.914	0.694	1.37	1.92	0.215	0.266	0.999
0.750	0.640	0.636	1.31	2.08	0.161	0.208	0.822
0.833	---	---	1.22	2.25	0.140	0.161	0.638
0.917	0.501	0.568	1.21	2.42	0.0969	0.124	0.506
1.08	0.469	0.556	1.25	2.58	0.0703	0.0840	0.361
1.25	0.414	0.500	1.23	2.75	0.0515	0.0601	0.233
1.33	0.363	0.453	1.28	2.92	0.0347	0.0400	0.199
1.42	0.334	0.421	1.25		E = 5 keV		

continued in next column

continued on next page

θ	$\left(\frac{d\sigma}{d\omega}\right)_+$	$\left(\frac{d\sigma}{d\omega}\right)_o$	$\left(\frac{d\sigma}{d\omega}\right)_{2s}$	θ	$\left(\frac{d\sigma}{d\omega}\right)_+$	$\left(\frac{d\sigma}{d\omega}\right)_o$	$\left(\frac{d\sigma}{d\omega}\right)_{2s}$
	(10^{-13})	(10^{-13})	(10^{-15})		(10^{-13})	(10^{-13})	(10^{-15})
0.417	1.294	0.694	1.564	1.75	0.212	0.206	0.927
0.500	0.823	0.662	1.597	1.91	0.165	0.138	0.598
0.583	0.683	0.650	1.564	2.08	0.113	0.0830	0.384
0.750	0.572	0.628	1.474	2.25	0.0650	0.0446	0.201
0.917	0.622	0.675	1.620	2.58	0.0222	0.0138	0.0588
1.08	0.428	0.525	1.541		E = 10.0 keV		
1.25	---	---	1.508	0.583	1.138	1.148	3.688
1.58	0.319	0.404	1.307	0.750	0.858	0.889	3.259
1.91	0.206	0.254	0.937	0.917	0.806	0.828	3.248
2.25	0.113	0.133	0.552	1.08	0.701	0.627	2.874
2.58	0.0521	0.0645	0.216	1.25	0.523	0.492	2.389
2.91	0.0246	0.0230	0.101	1.41	0.382	0.378	1.751
3.25	0.0112	0.0108	0.0386	1.58	0.304	0.235	1.299
	E = 8.00 keV			1.75	0.189	0.135	0.651
0.417	1.367	0.971	2.689	1.91	0.128	0.0717	0.374
0.583	1.006	1.027	2.555	2.08	0.0717	0.0382	0.183
0.750	0.807	0.889	2.366	2.25	0.0382	0.0220	0.0830
0.917	0.850	0.755	2.411		E = 12.0 keV		
1.08	0.590	0.667	2.178	0.500	1.211	1.305	4.450
1.25	0.476	0.496	2.000	0.667	1.011	1.065	4.033
1.41	0.387	0.396	1.600	0.750	0.938	0.990	4.011
1.58	0.307	0.284	1.355	0.917	0.743	0.794	3.606

continued in next column

continued on next page

θ	$\left(\frac{d\sigma}{d\omega}\right)_+$	$\left(\frac{d\sigma}{d\omega}\right)_o$	$\left(\frac{d\sigma}{d\omega}\right)_{2s}$
	(10^{-13})	(10^{-13})	(10^{-15})
1.08	0.609	0.591	3.014
1.25	0.508	0.423	2.378
1.41	0.419	0.285	1.666
1.58	0.275	0.177	0.920
1.75	0.168	0.0866	0.436
1.91	0.0860	0.0398	0.217
2.08	0.0425	0.0192	0.0865
2.25	0.0212	0.0103	0.0336

Data Table 3. Differential Cross Sections for Formation of H^+, H^o, and H(2s) by Dissociation

Projectile: H_2^+

Target: H_2

Energy: 10.0 keV

θ: Angle in Degrees [laboratory]

$\left(\frac{d\sigma}{d\omega}\right)_+$: Cross Section for H^+ Production in cm^2/steradian

$\left(\frac{d\sigma}{d\omega}\right)_o$: Cross Section for H^o Production in cm^2/steradian

$\left(\frac{d\sigma}{d\omega}\right)_{2s}$: Cross Section for H(2s) Production in cm^2/steradian

θ	$\left(\frac{d\sigma}{d\omega}\right)_+$ (10^{-13})	$\left(\frac{d\sigma}{d\omega}\right)_o$ (10^{-13})	$\left(\frac{d\sigma}{d\omega}\right)_{2s}$ (10^{-15})	θ	$\left(\frac{d\sigma}{d\omega}\right)_+$ (10^{-13})	$\left(\frac{d\sigma}{d\omega}\right)_o$ (10^{-13})	$\left(\frac{d\sigma}{d\omega}\right)_{2s}$ (10^{-15})
0.417	2.056	5.261	6.331	1.75	0.110	0.140	0.543
0.500	1.503	4.509	5.252	1.91	0.0630	0.0680	0.302
0.583	1.263	3.883	4.536	2.08	0.0342	0.0331	0.149
0.667	---	---	3.831	2.25	0.0163	0.0146	0.0787
0.750	1.042	2.850	3.523				
0.917	0.701	1.722	2.797				
1.08	0.564	1.148	2.422				
1.25	0.407	0.657	1.916				
1.41	0.285	0.423	1.618				
1.58	0.171	0.237	0.909				

continued in next column

Data Table 4. Differential Cross Sections for Formation of H^+, H^o, and H(2s) by Dissociation

Projectile: H_3^+

Target: H_2

Energy: 10.0 keV

θ: Angle in Degrees (Laboratory)

$\left(\frac{d\sigma}{d\omega}\right)_+$: Cross Section for H^+ Production in cm^2/steradian

$\left(\frac{d\sigma}{d\omega}\right)_o$: Cross Section for H^o Production in cm^2/steradian

$\left(\frac{d\sigma}{d\omega}\right)_{2s}$: Cross Section for H(2s) Production in cm^2/steradian

θ	$\left(\frac{d\sigma}{d\omega}\right)_+$	$\left(\frac{d\sigma}{d\omega}\right)_o$	$\left(\frac{d\sigma}{d\omega}\right)_{2s}$	θ	$\left(\frac{d\sigma}{d\omega}\right)_+$	$\left(\frac{d\sigma}{d\omega}\right)_o$	$\left(\frac{d\sigma}{d\omega}\right)_{2s}$
	(10^{-13})	(10^{-13})	(10^{-15})		(10^{-13})	(10^{-13})	(10^{-15})
0.417	2.108	7.380	6.400	1.91	0.0713	0.200	0.552
0.500	1.649	6.472	4.349	2.08	0.0562	0.136	0.410
0.583	---	4.979	4.114	2.255	0.0386	0.0850	0.246
0.750	0.883	3.518	3.668				
0.917	0.651	2.555	3.022				
1.08	0.408	1.607	2.364				
1.25	0.260	1.002	2.141				
1.41	0.187	0.709	1.706				
1.58	0.127	0.454	1.035				
1.75	0.0916	0.312	0.828				

continued in next column

Data Table 5. Fractional Content of Scattered Neutral Flux That Is in the 2s State (Charge Transfer Reaction)

This table includes only data at low scattering angles where it was impossible to carry out meaningful measurements of differential cross sections. The fractional metastable content for higher angles may be obtained by taking the ratios of $\left(\frac{d\sigma}{d\omega}\right)_{2s}$ and $\left(\frac{d\sigma}{d\omega}\right)_{o}$ from the tables of differential scattering cross sections.

Included here are data for two different sizes of the primary beam; the objective was to study influence of beam size on the data at low angles.

Projectile: H^+

Target: He

B_1: Data for a primary beam collimated by a circular aperture of 0.040" dia.

B_2: Data for a primary beam collimated by a rectangular aperture 0.040" high and 0.012" wide.

θ: Angle in Degrees (Laboratory).

$\frac{P_{2s}}{P_o}$: Fractional content of scattered neutrals that are in the 2s state (%).

E: Energy in keV.

E = 4.00 keV

θ	P_{2s}/P_o	
	B_1	B_2
0.000	---	0.417
0.067	0.435	---
0.083	---	0.444
0.100	0.466	0.475
0.234	0.476	---
0.250	---	0.585
0.333	---	0.915
0.400	1.11	---

continued in next column

continued on next page

θ	P_{2s}/P_o	
	B_1	B_2
0.566	2.72	---
	E = 5 keV	
0.050	---	0.532
0.116	---	0.434
0.300	---	1.02
	E = 6.25 keV	
0.033	0.742	0.645
0.067	---	0.622
0.283	---	1.13
0.300	0.858	1.50
0.384	1.35	2.34
0.466	2.84	---
0.517	---	3.94
0.636	3.95	---
0.800	4.29	---
0.966	3.63	---
1.13	2.88	---
1.30	4.80	---
	E = 10.0 keV	
0.017	---	0.850
0.033	0.979	---
0.050	0.832	0.791
0.117	---	0.723
0.133	0.780	0.692
0.200	0.750	0.790
0.283	0.911	1.30
0.300	0.988	---
0.367	1.11	6.21
0.467	5.68	---
0.633	8.81	---
0.783	7.17	---
	E = 15 keV	
0.050	0.627	---
0.117	0.660	---
0.283	0.724	---
0.450	4.58	---
0.617	4.37	---
0.783	4.19	---
	E = 20 keV	
0.067	1.10	---
0.100	1.22	---
0.267	1.16	---
0.350	1.32	---

continued in next column

Data Table 6. Total Cross Sections for Formation of H(2s)

A

Projectile: H^+

Target: He

Impact Energy keV	Cross Section 10^{-18} cm^2
3.92	0.070
5.80	0.330
8.60	0.703
8.70	0.650
10.3	0.907
10.7	0.922
12.2	1.03
12.8	1.05
14.6	1.13
14.9	1.08
16.7	1.29
17.9	1.47
18.6	1.58
19.1	1.80
20.0	2.08
22.2	3.12
23.9	3.83
26.2	4.89

B

Projectile: H^+

Target: Ar

Impact Energy keV	Cross Section 10^{-17} cm^2
4.2	.590
4.4	.549
4.48	.498
5.66	.500
8.72	1.20
8.88	.993
10.00	1.32
12.00	1.89
12.7	2.08
16.7	2.76
20.0	2.90
21.6	2.90
25.0	2.90
25.6	2.87
25.8	2.88

C

Projectile: H^+

Target: N_2

Impact Energy keV	Cross Section 10^{-17} cm^2
4.48	0.953
4.80	1.07
8.60	1.78
12.00	2.08
12.7	2.16
15.0	2.45
18.0	3.02
20.0	3.21
21.8	3.38
24.5	3.44
25.8	3.32

D

Projectile: H^+

Target: O_2

Impact Energy keV	Cross Section 10^{-17} cm^2
4.48	1.17
6.84	2.19
10.5	2.69
12.7	2.55
13.7	2.61
18.6	2.66
20.0	2.78
22.2	2.69
25.8	2.66

Data Table 7. Total Cross Section for Formation of H^o

Projectile: H^+

Target: He

Impact Energy keV	Cross Section 10^{-16} cm^2
4.00	0.177
6.25	0.410
10.0	0.940
15.0	1.50
20.0	1.70
25.0	1.73

APPENDIX B

METASTABLE FLUX DETECTION EFFICIENCY

The purpose of the experiments described in this study was to measure relative values of H(2s) production cross section; no direct measurement of an absolute cross section was carried out. In order to ensure that the relative values be valid, it is necessary to prove that the detection efficiency is invariant with projectile energy and constant in time. It is also desirable that some absolute magnitude be assigned to the data to facilitate their use in practical applications. To this end, a technique was developed for normalizing all cross sections to previous measurements of total cross sections by other research groups.

The next section contains a detailed discussion of the parameters that influence the detection efficiency. There follows a description of the method by which the absolute efficiency was established and how the variation in time of that efficiency was monitored. Finally, tests are described that ensure that the detection efficiency is independent of impact energy and independent of quenching fields.

Definition of Metastable Detection Efficiency

The detection efficiency of the metastable atom detector, D_e,* is defined as the ratio of the detector count rate N (counts/sec) to the flux

*The subscript 2s will be dropped for the remainder of this appendix.

of H(2s) atoms leaving the collision region R(0).

To evaluate the detector count rate in terms of R(0), consider a rectangular coordinate system fixed to the center of the collision chamber with the x axis extending through the center of the metastable detector. The count rate registered by the photon detector due to decay of H(2s) atoms emitting in a region dx at x is given by

$$dN = H(x)\ \varepsilon(x)\ dR(x) \tag{42}$$

where H(x) is the probability that a photon emitted at x will reach the cathode of the photon detector, $\varepsilon(x)$ is the probability that a photon that reaches the cathode will be detected, and dR(x) is the change in the flux of H(2s) while traveling a distance dx.

The change in metastable flux while traversing a distance dx is dependent on the flux at that point, R(x), the transition probability W(x), and the speed v. It is given by

$$dR(x) = \frac{W(x)R(x)}{v}\ dx\ . \tag{43}$$

Thus

$$R(x) = R(0)\ \exp\left[-\frac{1}{v}\int_0^x W(x')\ dx'\right]\ . \tag{44}$$

Substituting equations (43) and (44) into (42) and integrating, the net count rate, N(counts/sec), of the metastable detector is found to be

$$N = \frac{R(0)}{v}\int_0^\infty H(x)\ \varepsilon(x)\ W(x)\ \exp\left[-\frac{1}{v}\int_0^x W(x')\ dx'\right]\ . \tag{45}$$

Thus the detection efficiency D_e is given by

$$D_e = \frac{1}{v}\int_0^{\infty} H(x)\ \varepsilon(x)\ W(x)\ \exp\left[-\frac{1}{v}\int_0^{x} W(x')\ dx'\right] . \qquad (46)$$

Considerable simplification in equation (46) may be had by the application of the results of several tests described later in this appendix.

The transition probability W(x) is composed of contributions from natural decay, collision-induced decay, and electric field quenching. Natural decay may be ignored because, for the velocities and distances used in this experiment, the natural probability of 7 sec^{-1} [72] will not materially deplete the H(2s) flux before it reaches the detector. Collisional decay may be ignored because tests showed a linear relationship between H(2s) signal and target pressure. It follows that the decay probability is equal to that induced by electric fields. Lüders[72] has calculated the field dependence of the induced transition probability W and found it to vary from 7 sec^{-1} for zero fields to 6.25×10^8 sec^{-1} for electric fields greater than 1000 v/cm. For this experiment, the scattered H(2s) flux was well shielded from all electric fields except for the region of length L between the quench field plates of the H(2s) detector. In this region, the electric field was approximately uniform and of sufficient magnitude to ensure signal saturation. Using the approximation that W is zero outside the quench field region and constant within it, equation (46) may be written

$$D_e = \frac{1}{v} \int_0^L H(x)\ \epsilon(x)\ \exp\left[-W(x)/v\right] dx\ , \tag{47}$$

where the origin has been shifted from the center of the collision chamber to the leading edge of the exposed portion of the quench field plates.

The probability $H(x)$ that a photon emitted at x will reach the detector may be written

$$H(x) = \frac{1}{4\pi}\,\Omega(x)\ T_1\ T_2\ T_3(x)\ P(x)\ . \tag{48}$$

Here $\Omega(x)$ is the solid angle subtended by the cathode of the detector. T_1 and T_2 are the transmission of the wire grids in front of the MgF_2 window and the detector cathode, respectively. $T_3(x)$ is the transmission of the MgF_2 window. $P(x)$ is a correction factor necessary to account for anisotropic photon emission when the radiation is polarized.

If the x dependence of H and ϵ are temporarily neglected, D_e assumes the rather simple form

$$D_e = H\epsilon\left[1 - \exp\left(-(WL)/v\right)\right]\ , \tag{49}$$

which reduces to

$$D_e = H\epsilon \tag{50}$$

to within 0.1 percent for electric fields and speeds used in this apparatus.

The validity of neglecting the x dependence of the product $H\epsilon$ may be alluded to by considering the following two tests. First, for low and intermediate fields, equation (49) quite accurately represents the measured field dependence of the H(2s) signal. Second, for saturation fields, the

detection efficiency was found to be independent of the atom energy to within ± 10 percent; since changing the energy must invariably change the distribution of the emitters beneath the detector, independence of efficiency from energy indicates that $H\varepsilon$ is independent of x. It was concluded that the x dependence of $H\varepsilon$ may be neglected.

Calibration of the H(2s) Detection Efficiency

An absolute value was assigned to all 2s cross sections by normalizing a measured total electron-capture cross section to previously published measurements. Three independent and reasonably accurate absolute measurements of electron capture into the 2s state have been made by Jaecks et al.,[11] Andreev et al.,[14] and Bayfield.[73] It was decided to use the H^+ + Ar collision at 20 keV for a standard because all three measurements are in good agreement as to both magnitude and energy dependence. Normalization was made to the work of Andreev et al.[14] because this has the smallest estimated possible error (± 20 percent) and is the only direct measurement of cross section. For the photon detector, Andreev used a photo-ionization chamber whose efficiency is known quite accurately from fundamental measurements. A further reason for choosing Andreev's data is that the quenching field was uniform and unambiguously defined; consequently, it is possible to estimate an error limit caused by neglect of polarization effects.

Specifically, the 2s data of this study were normalized to the total H(2s) formation cross section for H^+ + Ar at 20 keV impact energy. Andreev et al.[14] measured this cross section to be $3.0 \pm 0.6 \times 10^{-16}$ cm^2.

The normalization was carried out as follows. The scattered flux

apertures were removed and the rotating arm set to zero degrees scattering angle. Argon gas was introduced into the collision chamber and the H(2s) flux produced by collisions between 20 keV protons and the target argon atoms was measured by the detector. Using the operational definition of a total cross section as given by equation (24), the value of the product $D_e L$ was evaluated. The operational definition of a differential cross section (see equation (20)) requires the knowledge of D_e alone. The effective value of L was expected to be somewhat larger than the geometrical distance between the entrance and exit apertures due to pressure gradients near the apertures and due to background gas in the vacuum chamber. H(2s) signal due to electron capture on the background gas was subtracted from the net signal, and the pressure gradients were accounted for by adding the sum of the two aperture diameters to the geometrical length.[74] The calculated length of the gas cell was 5.8 ± 0.3 cm.

Once the detection efficiency had been established, the monitoring technique described in the next section was used to interrelate and assign absolute values to all H(2s) data.

There is one aspect of the work of Andreev and co-workers that is subject to uncertainty. Their detection efficiency was evaluated on the assumption that field-quenched Lyman-alpha radiation was unpolarized and therefore isotropic. Recently it has been shown theoretically[75,19] and experimentally[75] that this is incorrect. The theoretical predictions by Sellin[75] are based on the assumptions that the metastable atom enters the quenching field slowly (i.e., adiabatically), while the predictions by Crandall[19] are based on a zero time of field entry. In Andreev's work,

the H(2s) atoms were created in the quenching field. It follows that Sellin's predictions are inappropriate for this case and the work of Crandall is more likely to give a correct value of polarization. No attempt will be made to correct the data of Andreev for polarization effects, but rather the limiting predictions of polarization by Sellin and Crandall will be used to calculate a maximum possible error due to the neglect of polarization.

When polarized radiation is sampled only over a narrow angular range at an angle θ with respect to the defining axis (in this case, the electric field), it is well known[76] that the true cross section is related to the measured cross section by

$$\sigma_{true} = \frac{3 - \pi}{3(1 - \pi \cos^2\theta)} \sigma_{measured} , \qquad (51)$$

where π is the polarization fraction of the emitted radiation and is defined to be $(I_{\parallel} - I_{\perp})/(I_{\parallel} + I_{\perp})$. $I_{\parallel}$ and $I_{\perp}$ are the intensity of radiation polarized parallel and perpendicular to the direction of the electric field, respectively, when $\theta = 90^{\circ}$. Using the prediction of Sellin, the true cross section would be 18 percent higher than that measured. Using Crandall's prediction, the true cross section would be 6 percent higher. Thus it is concluded that the data of Andreev are correct to within +38 percent and -14 percent when both experimental accuracies and neglect of polarization are taken into account. These are the absolute error limits that must be assigned to all measured 2s cross sections given in this study. Chapter V contains a complete analysis of possible errors in all 2s cross section measurements.

Routine Monitor of Efficiency

There is ample evidence that the detection efficiency of the electron multiplier D_e changes as a function of time, presumably due to changes in the surface condition of the photoemissive cathode. To take these changes into account, the following method is used.

The absolute efficiency was first evaluated as described previously with the collimating slits removed. Then the quench and pre-quench fields were removed and the target chamber evacuated. The remaining count rate of the funneled electron multiplier was primarily due to countable ultraviolet radiation produced by the impact of the 20 keV protons on the background gas in the vacuum chamber. The beam current to the Faraday cup and the pressure in the chamber (5×10^{-7} Torr) were recorded. Argon gas was then leaked into the large chamber until a pressure of between 1 and 3.10^{-6} Torr was recorded by an ionization gauge attached to the baseplate; at this pressure, less than 3 percent of the primary beam was neutralized. The increase in count rate was attributable to countable ultraviolet radiation produced by proton-argon collisions occurring in the field of view of the multiplier. The count rate per unit beam intensity per unit argon density, K_1, was a measure of the efficiency of the detector.

During operation of the experiment for differential cross section measurements, the collimating slits were replaced. In order to check the detection efficiency, the whole apparatus was again filled with argon and the countable ultraviolet signal per unit beam current to the Faraday cup per unit pressure, K_2, was measured. This quantity, K_2, is again a measure of efficiency and should be the same as K_1 measured by the same

method with the slits removed. In the event that K_1 and K_2 are not equal, then a change of efficiency is indicated, and a correction can be made simply by the ratio of these quantities.

This technique for monitoring changes of detection efficiency was used throughout the data-taking program. Changes of up to 60 percent were recorded over long periods of time. Changes during the course of a single day's operation were negligible. Tests showed that the MgF_2 window transmission did not change with time; it follows that variations of efficiency must be assigned to the changes in the secondary emitting properties of the Lyman-alpha detector.

Energy Dependence of the Detection Efficiency

Under high quenching fields sufficient to ensure complete mixing of the 2s and 2p levels, the effective lifetime of the metastable state is $\sim 1.6 \times 10^{-9}$ sec.[41] The decay length (product of impact velocity and lifetime) in the quenching electric field is comparable with the field of view of the detector. Consequently, as the velocity changes, the distribution of emitters in the quench region will also be altered. In the event that either ϵ or H as previously defined vary significantly with the angle of incidence of the photon, then the detector sensitivity D_e might exhibit a dependence of impact velocity. Tests were required to assess the magnitude of this effect. The lifetime of the H(2s) state is dependent on the strength of the quenching electric field and may be predicted theoretically.[41] It would be possible to guarantee velocity independent detection efficiency by varying the quenching field with velocity to maintain a constant decay length. This does have the disadvantage,

however, that quenching fields will be less than for an optimum efficiency, and therefore signal-to-noise ratios would be degraded. Data for this study were taken using high saturation fields, and thus optimum detection efficiency was achieved.

A test of the velocity dependence of the efficiency was carried out by measuring the ratio of signal at a low field where decay length was kept constant to the signal under optimum quench field; the variation of this ratio with impact velocity reflects changes in detection sensitivity. This test indicated that D_e varied by no more than 10 percent over the impact energy range of 4 to 20 keV.

It has been shown[44] that the field-induced Lyman-alpha emission will be polarized by an amount which varies with field strength. As mentioned above, polarization is related to anisotropy of emission. An experiment which detects photons emitted into a limited solid angle will therefore experience a change in effective detection sensitivity with electric field, and this factor is included in the definition of H. The test described above depends upon the detection efficiency at a series of selected low fields being independent of atom velocity. Using either the theoretical prediction of polarization by Sellin et al.[44] or those by Crandall,[19] it is readily shown that, over the range of low fields used to maintain constant decay length (30 to 40 v/cm), D_e varied by a negligible amount (less than 0.25 percent). The high quench field used during the experiment was not maintained constant; various values were employed between 300 and 600 v/cm, depending on projectile energy. The changing polarization contributes to the variation of detection efficiency

with projectile energy that is identified by the test described above. In conclusion, the existence of the field-dependent polarization does not invalidate the result that the detection efficiency changes by less than 10 percent over the impact energy range used.

H(2s) Signal Saturation

The metastable detector count rate was found to saturate as the electric field intensity was increased. The field dependence of the detected H(2s) signal may be calculated using equation (49) where the detector count rate was found to be

$$N = R(0)\ H\epsilon \left[1 - e^{-\frac{WL}{v}}\right] . \tag{52}$$

If it is assumed that the polarization of field quenched radiation is field independent, equation (52) may be written as

$$\frac{N}{R(0)\ H\ \epsilon} = f(F) = 1 - e^{-\frac{W(F)L}{v}} , \tag{53}$$

where F is the electric field intensity in v/cm.

Figure 21 shows the H(2s) count rate as a function of quench field for 4.4 keV and 25 keV impact energy. The data have been normalized to equation (53) at 275 v/cm for 4.4 keV and 350 v/cm for 25 keV.

The field dependence of the quenching transition probability W may be calculated theoretically[72] by considering the mixing effect of a uniform electric field on the $2s_{1/2}$ state with its neighboring $2p_{1/2}$ and $2p_{3/2}$ states. The calculated transition probability is presented in

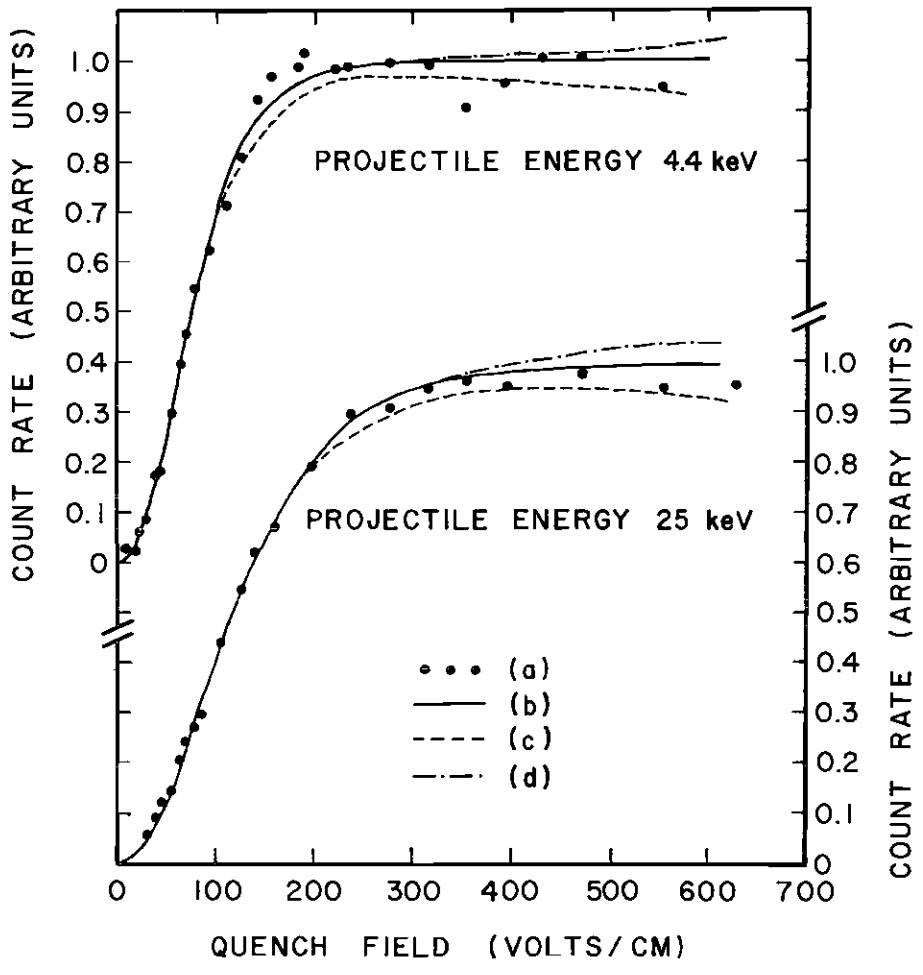

Figure 21 H(2s) Detector Saturation Curves. (a) H(2s) detector count rate. (b) theoretical predictions, no polarization. (c) theoretical prediction with polarization corresponding to adiabatic entry into electric field.[44] (d) theoretical prediction with polarization corresponding to sudden entry into electric field.[19]

Figure 22. Since the evaluation of this transition probability involves the solution of a cubic equation, no relatively simple expression for it exists for arbitrary field intensity. However, if one performs the calculation excluding the $2p_{3/2}$ state, such an expression may be derived[77] and is given by

$$W_{2s}(F) = 3.12 \times 10^8 \left[1 + \frac{\delta^2}{[1 - (1 + \delta^2)^{1/2}]^2}\right]^{-1} \text{ sec}^{-1} , \qquad (54)$$

where $\delta = F/237$. This two-state transition probability is found to agree to within 5 percent with the three-state calculation for fields below 200 v/cm but as may be seen from Figure 22, the two calculations approach different high field limits.

For small fields ($F \leqq 100$ v/cm), both calculations approach the function

$$W = 2720\ F^2 \text{ sec}^{-1} . \qquad (55)$$

This quadric dependence on quenching field is evident in both saturation curves of Figure 21. That the detector count rate should have this quadric dependence is clear when the exponential in equation (53) is expanded for small W.

If a field-dependent polarization such as calculated by Sellin or Crandall is assumed, f(F) must take the form

$$f(F) = \frac{3}{3-\pi}\left[1 - e^{-\frac{WL}{v}}\right] , \qquad (56)$$

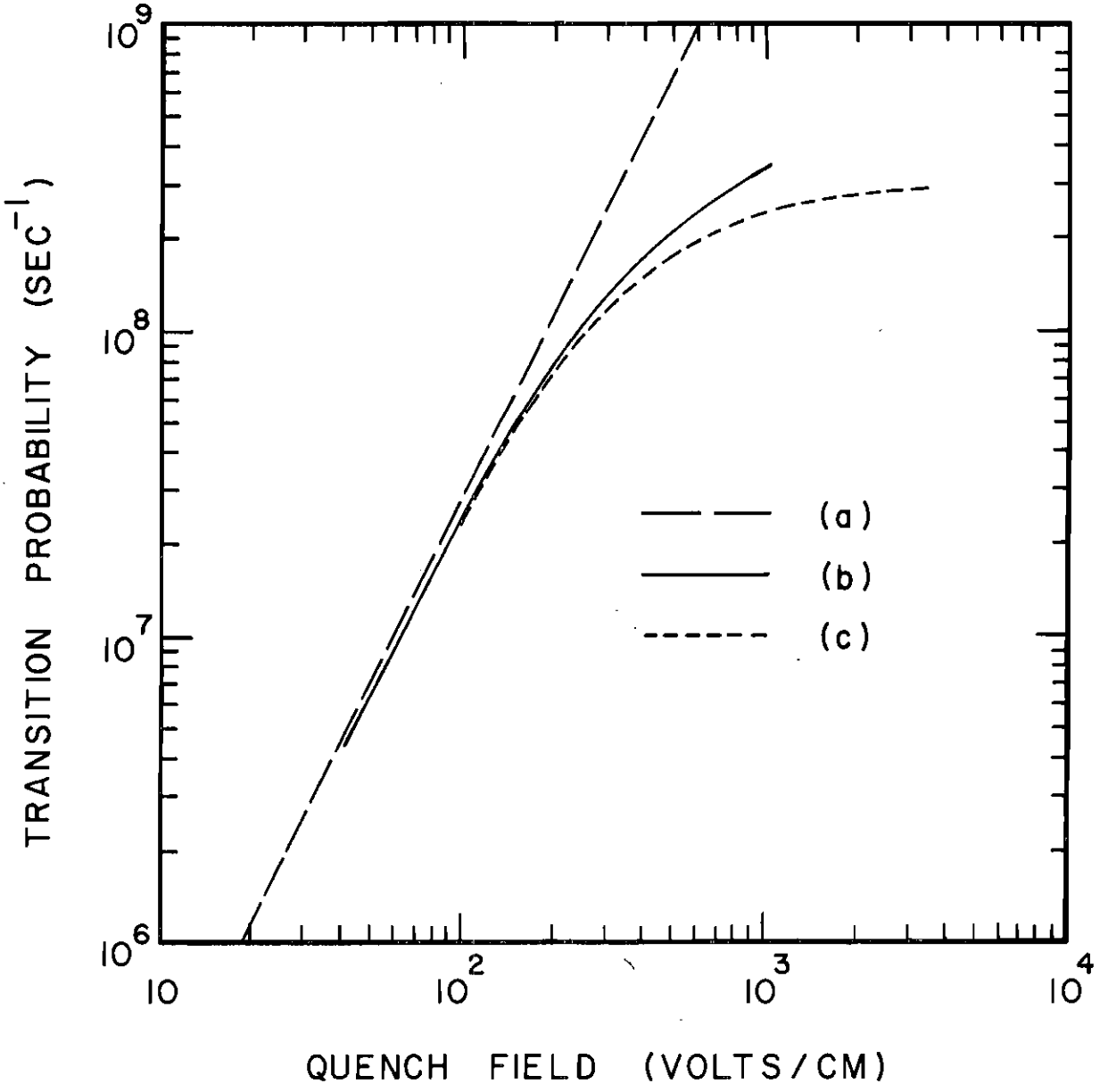

Figure 22 Electric Field Dependence of the Metastable Transition Probability, (a) $W(F) = 2727\ F^2\ sec^{-1}$, (b) three-state calculation[72], (c) two-state calculation[77].

where π is the polarization fraction. Equation (56) is included in Figure 21 for the two extreme cases of infinite entry time (Sellin) and zero entry time (Crandall). Although the data seem to fall between these extremes, indicating an intermediate functional form for the field dependence of π, the test is too insensitive to make a quantitative prediction. However, the overall agreement between experiment and theory is gratifying and indicates proper operation of the detector.

It should be noted that, for the metastable detector used in this experiment, the achievement of signal saturation with increasing electric field is not a result of transition-rate saturation. Saturation occurred when essentially all the metastables were quenched within view of the funneled electron multiplier, i.e., when $\exp [- WL/v]$ was small compared to one. The three-state calculation of W by Lüders[72] indicates that, for the fields used in this experiment (300 to 600 v/cm), W was between 1.4×10^8 sec^{-1} and 2.5×10^8 sec^{-1}, far from its saturation value of 6.25×10^8 sec^{-1}.

APPENDIX C

EVALUATION OF THE SECONDARY EMISSION COEFFICIENT FOR H^o

Assignment of absolute values to the neutral data presented in this thesis required the evaluation of the secondary electron emission coefficient γ_o. Since secondary emission coefficients are known to depend on the surface condition and nature of the bombarded material, this quantity must be experimentally measured in situe.

The primary difficulty in evaluating γ_o is that an independent method of measuring the neutral current must be found. Once this is done, γ_o may be evaluated as the ratio I_o/i_o where I_o is the current of secondary electrons produced by the neutral current i_o.* The method chosen to independently measure i_o is simple and in fact is the method used by many experimentalists to measure total electron-capture cross sections. The technique is based on the fact that for each neutral atom formed by electron capture within the target cell, there is left behind a singly charged target ion. If these ions are collected to the inner shell of the collision chamber, they produce a current i_c which is numerically equal to i_o. Ionization events produce equal positive and negative currents and do not contribute to the net i_c. Thus γ_o may be evaluated via the ratio I_o/i_c.

---

*See page 66 for a definition of the neutral "current" i_o.

To perform this experiment, the scattered flux collimating slits were removed and the rotating arm set to zero degrees scattering angle. Target gas (helium) was introduced into the collision chamber to neutralize a small fraction of the H^+ primary beam. The ion/atom detector was operated in the secondary emission mode, and the primary beam was deflected from the central plate of the detector by the electrostatic H(2s) quench field. The inner shell of the collision chamber was biased at -30 volts to collect target ions, and the outer shell was grounded. A slender rod was inserted into the inner shell from the pressure measuring region below. The rod was biased positive to collect electrons resulting from ionizing collisions. Figure 23 shows the electrical connections used to measure i_c and I_o. A correction of approximately 10 percent to I_o was made for neutrals formed by electron capture-collisions external to the target cell, which of course would not contribute to i_c.

Using the above technique, γ_o was measured as a function of impact energy from 4 to 25 keV. In addition γ_+ was measured at the same time for reasons that are presented below.

While data were being taken for the differential cross sections, γ_+ was found to decrease slowly due to a cumulative effect of heavy bombardment of the secondary emission surface by the ion beam. Although γ_+ could be measured with the scattered flux collimator slits in place, the technique used to measure γ_o required their removal. Thus it was necessary to find a secondary means of monitoring γ_o while differential data were being taken. It has been proposed that the ratio γ_o/γ_+ should be nearly independent of surface composition or condition.[73] To check this

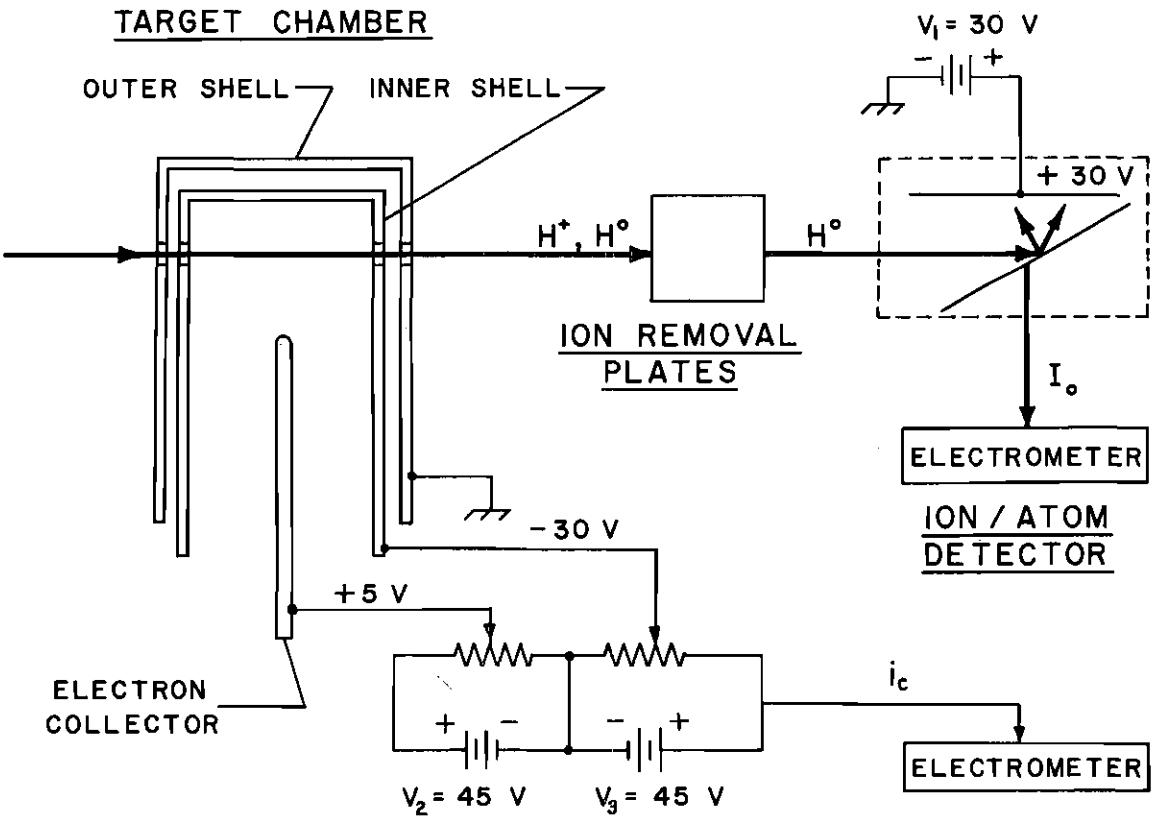

Figure 23 Flow Chart for Measuring the Neutral Secondary Emission Coefficient.

proposition, this ratio was measured for the particular surface used in this experiment and compared with results of three other investigations[78, 79, 80] for a variety of materials and surface conditions. The results, shown in Figure 24, indicate that, at least for surfaces that have not undergone special cleaning procedures, this ratio is fairly independent of surface parameters. It was concluded that γ_o/γ_+ should remain constant in time even though γ_+ and γ_o may be changing as the surface condition changes.

The neutral secondary emission coefficient could now be monitored with the slits in place in the following manner: γ_o/γ_+ was measured once with slits removed; then γ_+ was continually monitored and γ_o evaluated using the measured ratio.

With the slits in place, γ_+ was checked for variation as the apparatus was set for different scattering angles. For all angles where differential cross sections were measured (θ larger than approximately 0.5 degree), γ_+ was found to be independent of angle. However, as the rotating arm was brought to the zero-degree position, γ_+ was found to decrease. This behavior may be explained on the following grounds. At large angle settings, scattered H^+ flux reaching the detector through the collimating slits is disturbed over a large fraction of the center plate. Most regions of this plate had not been exposed to the primary beam and thus had a relatively high value of γ_+. At small angles ($\theta < 0.5$ degree), a portion of the unscattered beam could pass through the slit system and reach this central region of the plate. Because of the intensity of the beam, the secondary electron current produced by this flux far outweighed

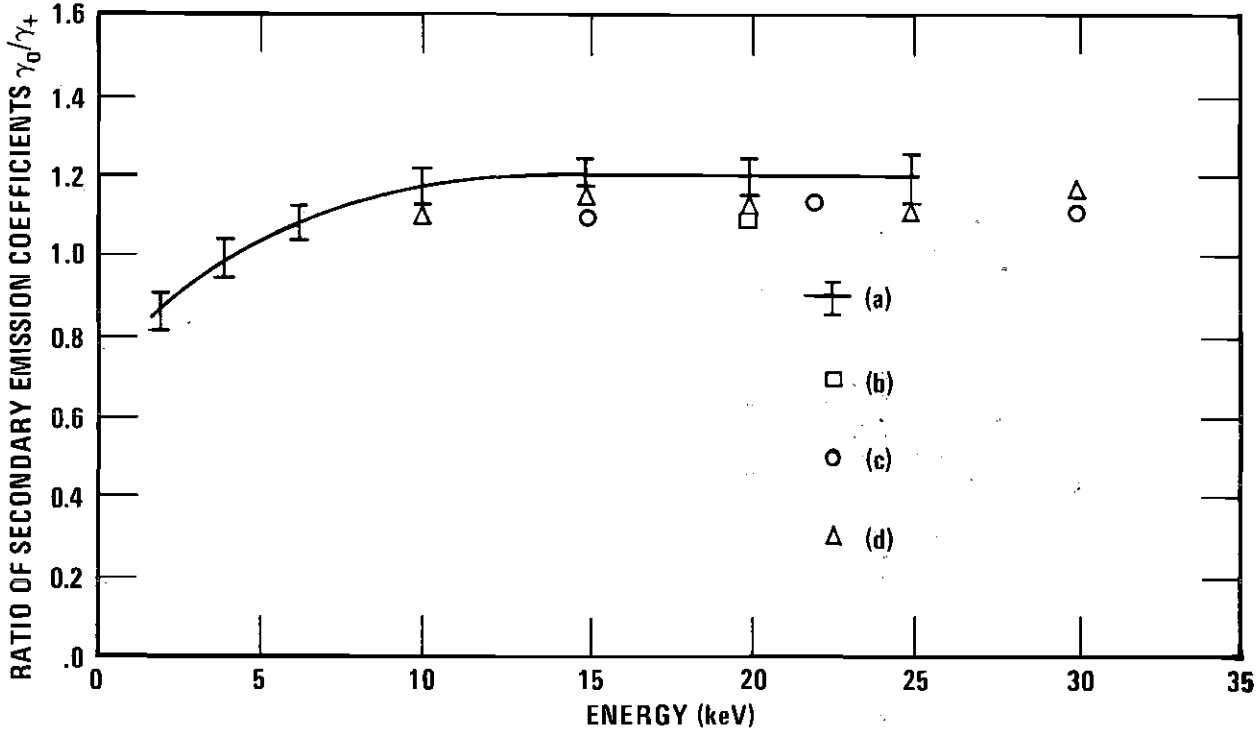

Figure 24 The Ratio of the Secondary Emission Coefficient for H^+ to the Secondary Emission Coefficient for H^o. (a) present work, (b) Stier et. al.(79), (c) Dagnac et. al.(80), (d) Chambers(78).

that produced by scattered flux incident on other portions of the plate. Thus for small angles, γ_+ was essentially being measured for the small "burnt" region of the central plate, whereas at large θ, almost all of the plate was being sampled.

Based on the arguments and data presented above, it was assumed that γ_o/γ_+ was independent of the condition of the surface. The value of γ_+ was always measured directly and the ratio γ_o/γ_+ taken from the data in Figure 24. In practice, γ_+ changed slowly for a period of two months and then became constant.

Figure 25 shows the energy dependence of γ_+ for both the central "burnt" spot (angular setting of 0 degrees) and a mean value over the "unburnt" region (for all angular settings greater than 0.5 degree).

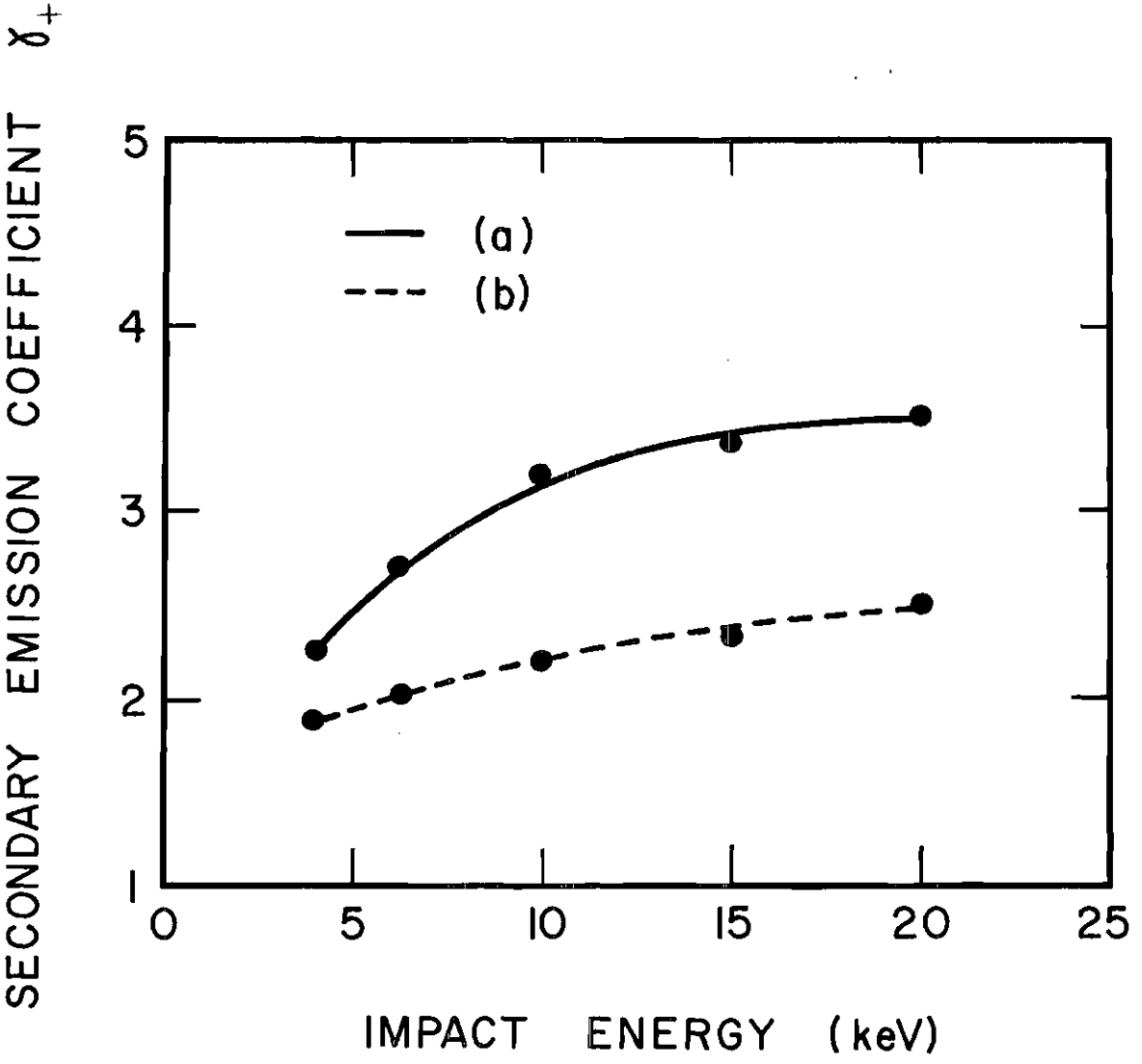

Figure 25 Energy Dependence of Secondary Emission Coefficient for H^+. (a) Large angle data, (b) zero degree data.

APPENDIX D

MEASUREMENT OF THE TOTAL ELECTRON CAPTURE CROSS SECTION σ_o

While performing the calibration experiment for γ_o, the total cross section for the reaction

$$H^+ + He \rightarrow H^o + [He^+] \tag{57}$$

was measured. The cross section was evaluated by the equation

$$\sigma_o = \frac{i_c}{N_t I_p L} \tag{58}$$

which is a slightly modified form of equation 24. Here i_c is the net positive current formed in the target cell by electron capture collisions; I_p is the beam current; N_t is the target density; and L is the effective length of the target region. The measurement of i_c was described in the preceding appendix. The evaluation of the effective gas cell length was discussed in Appendix B. The magnitude of L was found to be 5.8 ± 0.3 cm. Standard tests were performed to show that σ_o was independent of N_t.

Figure 26 presents the results of this measurement. The cross section was found to rise monotonically with impact energy from 0.177×10^{-16} cm^2 at 4 keV to 1.73×10^{-16} cm^2 at 25 keV. It is estimated that the possible absolute error did not exceed ± 10 percent. The reproducibility was better than ± 5 percent.

The present data are in good agreement with previous determinations.[81,82,83,84]

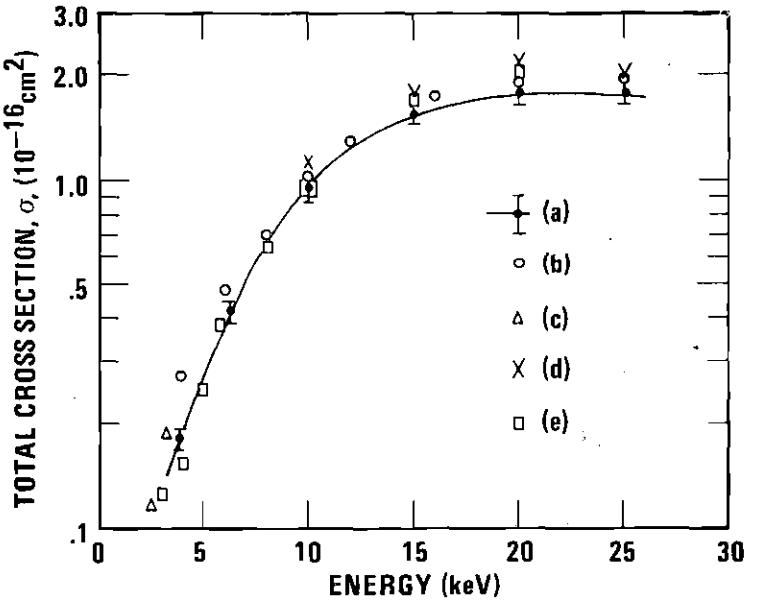

Figure 26 Total Electron Capture Cross Section for Protons Incident on Helium. (a) present work, (b) Stier and Barnett[81], (c) Stedeford and Hasted[82], (d) DeHeer et. al.[85], (e) Williams and Dunbar[84]. Error bars indicate limits of reproducibility.

APPENDIX E

ALIGNMENT PROCEDURES

Alignment of the apparatus was a two-step program. First, the module support system was aligned with the accelerator; and second, the modules were aligned with respect to the support system.

Before alignment with the accelerator, the module support system was adjusted so that its rails were parallel to the plane defined by the base of the hub to within ± 0.0013 cm over their entire length. The support system and hub were placed on an optical flat, and the height of the rails was measured with a traveling dial indicator. The fixed rail was adjusted by means of the support rod attached to its end while the rotating rail was adjusted by means of the single support leg located at the end. The support system was then transferred to the vacuum chamber, and the hub bolted to a mating surface in the baseplate. The baseplate was then moved to align the rail system with the accelerator. This alignment was not critical and was done with little trouble by use of a laser beam.

A precise module alignment procedure was developed which used the machined accuracy of the rail support system; the modules were mechanically aligned with respect to a test section of rail and then transferred to the support system in the vacuum chamber. The procedure for aligning the module with respect to the rail was as follows. The alignment rail

carrying the module was mounted on the bed of a Bridgeport milling machine, and a telescope was clamped in the spindle. The mill bed was moved perpendicular to the rail and traversed the module across the telescope's field of view. The positions of the edges of the module's aperture were recorded from the feed dial, and the center of the aperture was calculated as the average of these two readings. The module was then rotated 180 degrees, and the measurement was repeated. If the two center lines coincided, the aperture was centered on the rail. If the center lines did not coincide, the module was shifted slightly and the procedure repeated. The height of the aperture above the rails was measured by vertical movement of the mill bed. Alignment accuracies of $\pm$ 0.001 cm were readily obtainable with this procedure.

APPENDIX F

APPARATUS FUNCTION

In Chapter II the operational definition of a differential cross section was derived. There it was shown that, although the true differential cross section was defined as the ratio of differential elements, the measured cross section was defined in terms of a ratio of the two averaged quantities $N_i(\theta)$ and $G(\theta)$. This averaging process is inherent in any practical experimental measurement of a differential cross section because of the necessity of finite collimation apertures.

In this appendix the geometrical factor $G(\theta)$ will be evaluated for the particular aperture system used for the present work. In addition, comments will be made regarding systematic errors introduced due to the averaging process.

Evaluation of $G(\theta)$

The geometrical factor $G(\theta)$, defined by equation (17), is the integral of the solid angle $\Delta\omega$ over the region defined by ΔV. Writing $\Delta\omega$ as $\omega(x,y,z)$ and ΔV as $V(\theta)$, the integral which must be evaluated is

$$G(\theta) = \int_{V(\theta)} \omega(x,y,z)\, d^3\tau \ . \tag{59}$$

Here $V(\theta)$ is that region of space where (a) the target density is not zero, (b) the projectile density is not zero, and (c) the solid angle

$\omega(x,y,z)$ is not zero. The x axis defines the direction of the primary beam, and the angle θ lies in the x-y plane.

Equation (59) will be evaluated first for a beam of small width and height. The results will then be shown to be applicable to the finite beam case for the particular geometry used in this experiment. The following derivation is based on the work of Skalskaya,[85] Kaminker and Fedorenko,[86] and Filippenko.[87]

Consider a very thin projectile beam of cross sectional area A* directed along the x axis as shown in Figure 27. Two rectangular apertures, the center line of which defines the set scattering angle θ, are positioned a distance ℓ and $H + \ell$ from the point of intersection of their center line and the x axis (this point is in fact the center of the collision chamber). The width of the first slit is represented by a. The height of the first slit does not enter the calculation of σ as long as it is greater than or equal to the height of the second slit. This was the case for the present geometry. The width and height of the second slit are b and h, respectively.

The solid angle $\omega(x)$ is defined to be the solid angle "seen" by each point x along the x axis and is determined by the edges of slits 1 and 2. The points C_4 and C_2 define the extreme positions along the x-axis beyond which ω is identically zero. The portion of the x axis for which ω is not zero has been labeled $L(\theta)$. For a very thin beam, ω will not depend on y or z, and equation (59) may be written as follows:

---

*By thin it is meant that the y and z dimensions of the beam are very small compared to all slit widths.

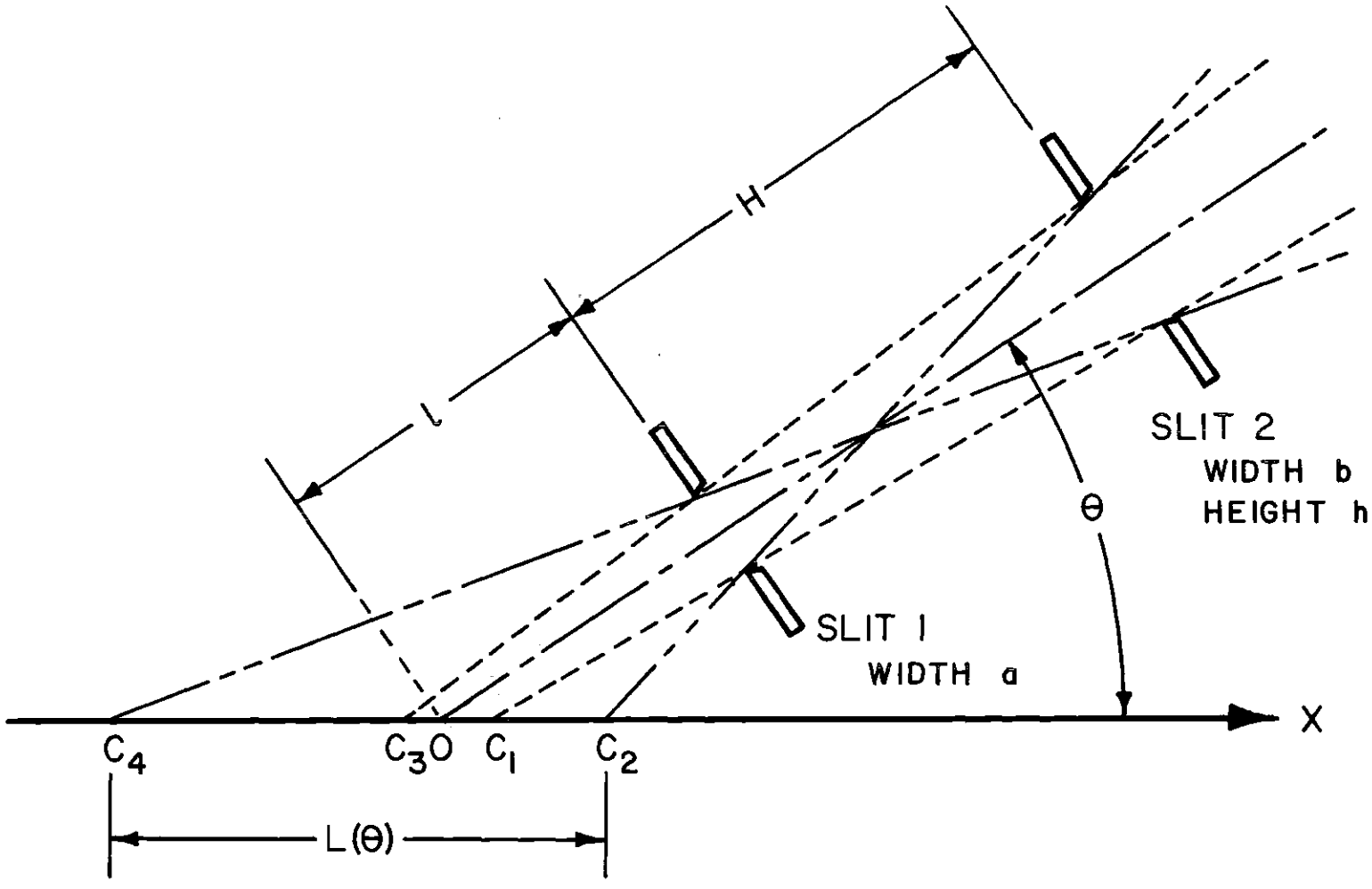

Figure 27 Scattered Flux Collimation Apertures Slit width a: 0.0324 ± 0.0013 cm. Slit width b: 0.1085 ± 0.0013 cm. Slit height h: 0.310 ± 0.003 cm. Distance ℓ: 4.17 ± 0.08 cm. Distance H: 10.16 ± 0.10 cm.

$$G(\theta) = A \int_{L(\theta)} \omega(x)\, dx \ . \tag{60}$$

The details of the evaluation of equation (60) have been given by Taylor[88] and will not be repeated here. Basically, the procedure is to derive the analytic form of $\omega(x)$ for each of the four regions of the x axis defined by the points C_1, C_2, C_3, C_4, and the origin O, and then perform the following integration:

$$\int_{L(\theta)} \omega(x)dx = \int_{C_4}^{C_3} \omega_1(x)dx + \int_{C_3}^{0} \omega_2(x)dx + \int_{0}^{C_1} \omega_3(x)dx + \int_{C_1}^{C_2} \omega_4(x)dx \ . \tag{61}$$

The result of this calculation is

$$\int_{L(\theta)} \omega(x)dx = \frac{bh}{[H+\ell]} \left\{ \frac{C_1}{H+\ell - C_1 \cos\theta} - \frac{C_3}{H+\ell - C_3 \cos\theta} \right\} \tag{62}$$

$$+ \frac{h}{2} \left\{ \frac{[2(H+\ell)\tan\theta + 6]\,[C_2 - C_1]}{[H+\ell - C_2 \cos\theta][H+\ell - C_1 \cos\theta]} \right\}$$

$$+ \frac{h}{2} \left\{ \frac{[2(H+\ell)\tan\theta + b]\,[C_4 - C_3]}{[H+\ell - C_3 \cos\theta][H+\ell - C_4 \cos\theta]} \right\}$$

$$+ \frac{h[2\ell\tan\theta - a]}{2H\cos\theta} \left\{ \ell n \left[\frac{(\ell - C_2\cos\theta)(H+\ell - C_1\cos\theta)}{(\ell - C_1\cos\theta)(H+\ell - C_2\cos\theta)} \right] \right\}$$

$$+ \frac{h[2\ell\tan\theta + a]}{2H\cos\theta} \left\{ \ell n \left[\frac{(\ell - C_4\cos\theta)(H+\ell - C_3\cos\theta)}{(\ell - C_3\cos\theta)(H+\ell - C_4\cos\theta)} \right] \right\} \ .$$

Here

$$C_1 = \frac{aH + \ell\,(a-b)}{2H\sin\theta + (a-b)\cos\theta} \ , \tag{63}$$

$$C_2 = \frac{aH + \ell\,(a+b)}{2H\,\sin\theta + (a+b)\,\cos\theta}\ ,$$

$$C_3 = -\frac{aH + \ell\,(a-b)}{2H\,\sin\theta - (a-b)\,\cos\theta}\ ,$$

and

$$C_4 = -\frac{aH + \ell\,(a+b)}{2H\,\sin\theta - (a+b)\,\cos\theta}\ .$$

Equation (62) is similar to the expression derived by Fillipenko[87] with one small exception. Fillipenko found the coefficients of the two logarithms to be identical and thus combined tham into a single term. It is believed that equations (62) and (63) are correct.

As the angle θ is decreased, the point C_4 moves away from the origin (center of the scattering cell) and for sufficiently small angles moves out of the target chamber. Since the target density N_t is negligible past this point, a systematic error in the value of $G(\theta)$ would result if this region were included in the integration. To account for this error, C_4 was replaced in equation (62) by the distance to the target cell entrance aperture for those angles where C_4 lies outside the collision chamber.

For angles where C_4 lay within the target region, equation (62) may be considerably simplified by the insertion of C_1, C_2, C_3, and C_4. The result may be written

$$\int_{L(\theta)} \omega(x)dx = \frac{ah}{H\,\cos\theta}\ \ell n\left[\frac{2(H+\ell)\,\sin\theta + b\,\cos\theta}{2(H+\ell)\,\sin\theta - b\,\cos\theta}\right]\ . \qquad (64)$$

This is the expression given by Skalskaya.[85] If the ℓn term is expanded,

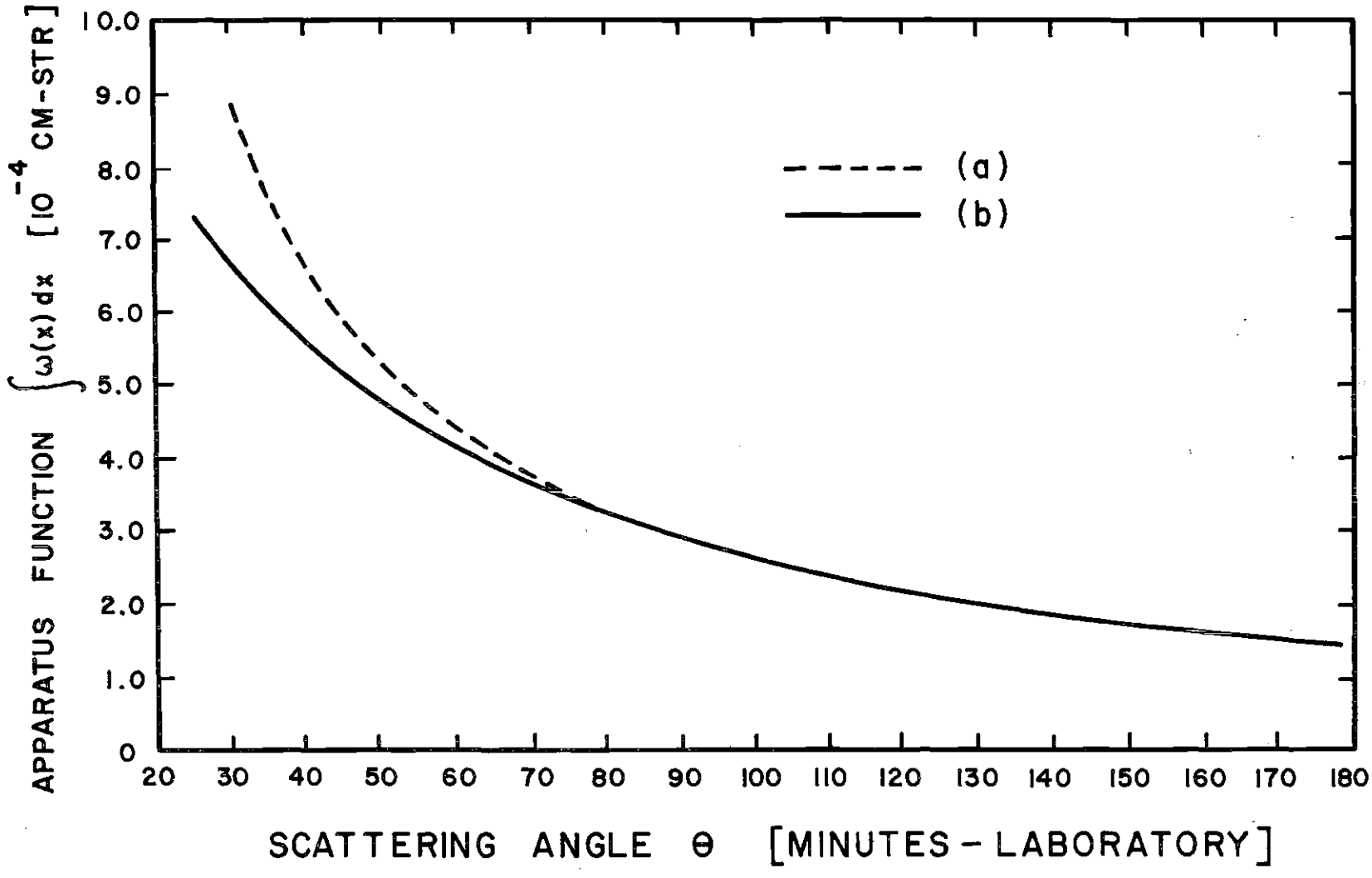

Figure 28 Geometrical Factor $\int\omega dx$. (a) Jordan and Brode[89]. (b) Present calculation.

one obtains

$$\int_{L(\theta)} \omega(x)dx = \frac{abh}{H(H+\ell)\ \sin\theta}\left[1 + \frac{1}{3}\xi^2 + \ldots\right], \qquad (65)$$

where $\xi = \frac{b\ \cos\theta}{2(H+\ell)\ \sin\theta}$. The first term in this expansion is the result obtained by Jordan and Brode.[89]

If the second term of the expansion is small compared to 1, the Jordan-Brode result may be used. This requires that

$$1/3\ \frac{b^2\ \cos^2\theta}{4(H+\ell)^2\ \sin^2\theta} \ll 1\ . \qquad (66)$$

This inequality is well satisfied for the experimental arrangement used in the present study for those angles where C_4 was inside the target region.

Figure 28 shows the calculated values of $\int_{L(\theta)} \omega(x)dx$ for equation (62) and for the Jordan-Brode equation. The angle at which C_4 moves out of the target cell for the present system of apertures was approximately 1.5 degrees.

Finite Beam Considerations

The applicability of equation (62) to the realistic situation of a beam with finite width and height has been investigated in two ways.

First, a computer program provided by Menendez[90] was employed to calculate equation (59) for a finite beam size. The program uses a Monte Carlo technique to perform the integration to an accuracy of ± 5 percent. The results agreed with those of equation (62) to within five percent for

all angles.

Second, an experimental test of the effect of beam diameter was made by reducing the beam size from approximately 0.10 cm to 0.03 cm and comparing the low-angle differential cross sections with those previously measured. No systematic change was observed for any energy or angular range.

Based on these two results, it was concluded that, at least for the particular geometry employed in the present study, equation (62) could be used in the evaluation of the geometrical factor.

Apparatus Resolution

When an apparatus with finite collimating apertures is set to an angle θ_o, flux scattered through a range of angles $\Delta\theta$ may pass through the slits and be detected. It is somewhat misleading to quote the full $\Delta\theta$ as the angular resolution because flux scattered by an angle near the extremes of $\Delta\theta$ "sees" a small solid angle and should be weighted less than flux scattered near θ. The computer program provided by Menendez[90] subdivided $\Delta\theta$ into thirty ranges $\delta\theta_i$. A plot of this weighting factor against θ showed a narrow peaked distribution centered on θ_o which decreased to zero at the extremes of $\Delta\theta$. The resolution quoted in this thesis will be defined as the full width at half maximum of this distribution. The resolution was found to be $\pm$ 0.2 degree.

Effects of Finite Resolution

The effect of the finite resolution is twofold. First, oscillation in the differential cross section with periods much less than 0.4

degree should not be observable. Second, for differential cross sections which vary rapidly with angle (such as the electron capture data), the measured cross section may be shifted in value from the true cross section. This is because flux scattered into the angular range $\theta_o - \frac{\Delta\theta}{2}$ is more intense than that scattered into $\theta_o + \frac{\Delta\theta}{2}$. The total differential cross section calculated using the screened Coulomb potential as described in Chapter III was convolved with the weighting factor given by Menendez's program for the impact energy of 20 keV. The convolved cross section was shifted up by approximately 25 percent. This effect is not so important for the dissociation data since the distributions fall less precipitously with angle than those for electron capture. Also, the derived probabilities should be free of this effect since they are ratios of cross sections.

APPENDIX G

MEASUREMENT OF TOTAL CROSS SECTIONS FOR THE FORMATION OF H(2s)

[Copy of paper published in the Physical Review]

HYSICAL REVIEW A VOLUME 3, NUMBER 4 APRIL 1971

Formation of Metastable Hydrogen Atoms by Charge Transfer*

R. L. Fitzwilson and E. W. Thomas
Georgia Institute of Technology, Atlanta, Georgia 30332
(Received 16 June 1970)

Measurements are presented of the total cross sections for formation of metastable hydrogen atoms by charge transfer as protons traverse targets of helium, argon, nitrogen, and oxygen. Projectile energies range from 4 to 26 keV. An H^+ projectile beam was directed into a cell containing the target gas and emerged into an evacuated region where the metastable-state content was determined. The H(2s) flux was monitored by electric field mixing of this state with the 2p level and detection of the resulting Lyman-α photon. The relative variation of cross section with projectile energy for targets of He and Ar is in agreement with previous work. For oxygen the cross section increases with energy from 4 to 10 keV and remains constant from 10 to 26 keV; for nitrogen the cross section increases monotonically with increasing energy.

I. INTRODUCTION

The objective was to study the formation of metastable H by the process of charge transfer as a beam of H^+ ions traverses a gaseous target. The reaction is given by

$$H^+ + X \rightarrow H(2s) + [X^+] \,. \tag{1}$$

The experiment detects the formation of the metastable hydrogen and gives no information on the state of ionization or excitation of the postcollision target system shown within the square brackets. There has been much previous work on processes of the type described by Eq. (1), and the techniques are well established. Jaecks *et al.*,[1] Andreev *et al.*,[2] and Bayfield[3] have made detailed studies of this type of process but confined their work primarily to targets of the rare gases. The present work was undertaken with the primary aim of studying the charge-transfer process on targets of O_2 and N_2, mechanisms that have obvious importance to the understanding of auroral phenomena.

II. APPARATUS

The apparatus for this work was of conventional design and is shown diagramatically in Fig. 1. Hydrogen ions were produced in a rf source, accelerated to energies of between 4 and 26 keV, and mass analyzed to produce an H^+ beam. Two circular apertures of 2.54- and 1.02-mm diam separated by a distance of 36 cm were used to collimate the beam. The target was contained in a cell of 6.7-cm length, the beam entered through a circular aperture of 2.54-mm diam and exited through a circular aperture of 3.2-mm diam. After traversing the cell, the beam emerged into an evacuated region where the excited-state fraction and beam current were monitored. An electric field was applied transverse to the beam to induce mixing between the 2s and 2p states, causing emission of a Lyman-α photon. The photons were detected by a funneled electron multiplier (Mullard type B 419 BL) which was operated in a counting mode; it was arranged to view perpendicularly to the particle trajectory and to the electric field. A LiF plate was placed over the cathode of the detector so that it was sensitive to photons of wavelengths from the LiF transmission cutoff at 1100 Å to the sensitivity cutoff of the channel multiplier at 2000 Å. The metastable detector was placed 14.2 cm from the exit of the gas cell; at this point spontaneous emission from the 2p state had decayed to negligible proportions. Beyond the detector was a Faraday cup which monitored the total flux of ions in the projectile beam. Suitable potentials were provided to inhibit the loss of secondary electrons.

Projectile energy was determined directly by a precision 90° cylindrical electrostatic analyzer, located between the collimating apertures on the path of the incoming H^+ beam. Energies were determined to an accuracy of ±1%.

The target gases, stated by the manufacturer to be 99.99% pure, were supplied from high-pressure cylinders and leaked into the scattering chamber through a needle valve. A dry-ice and acetone cold trap was used to remove condensable impurities. Target pressures were generally maintained at or below 10^{-4} Torr; it was demonstrated that at these pressures the measured cross sections were independent of target density. Target pressures were monitored with a capacitance manometer whose response was independent of the nature of the gas. Linearity of response was checked against a trapped McLeod gauge, using H_2 as the test gas, and shown to be linear within ±4%. Since the data from this experiment were in the form of relative cross sections, it was unnecessary to determine an absolute value of target pressure.

The beam preparation system, collimator, energy analyzer, and detection systems were located in a

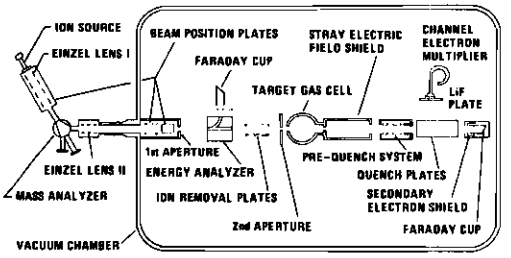

FIG. 1. Schematic diagram of the apparatus.

large tank evacuated with trapped oil diffusion pumps to a base pressure of better than 10^{-7} Torr. The target gas occupied a small cell within the main tank; flow of gas from the target to the main tank was minimized by the small apertures through which the beam entered and exited. The pressure differential between the cell and tank was a factor of 100 or more.

III. EFFICIENCY OF METASTABLE DETECTOR

The objective of the experiment was to determine relative cross sections as a function of impact energy. No attempt was made to directly determine the absolute sensitivity of the system. Particular attention was directed to ensuring that detection sensitivity remained invariant with projectile energy; an empirical test was devised to test this invariance.

The quenching electric field was provided by a parallel plate assembly consisting of two rectangular plates 3.2 cm high by 7.6 cm long and spaced 2.54 cm apart. Two grounded shields were incorporated to reduce the spatial extent of the fringe field; the U-shaped shields wrap around the front of each quench plate and protrude into the space between the plates approximately 2.6 cm leaving 5 cm of the quench plate exposed. Between the quench plates, the shields were spaced 0.508 cm apart and were centered on the axis of the particle beam. Care was taken to ensure that no appreciable fraction of the metastables were quenched outside the detector's field of view by fringe fields from the quench plates.

The intensity of the electric field along the beam axis was calculated to an accuracy of $\pm 10\%$ by the use of a mapping function. The intensity rises from 0.1 to 90% of its asymptotic value in a distance of 1 cm; it is approximately 50% at the edge of the grounded shield. Thus the fringe field was negligible at distances greater than 0.5 cm from the edge of the grounded shield. The detector viewed a region extending from 2 cm in front of this edge to 7 cm past this edge; consequently, the small fraction of the metastables quenched by the fringe field (0.5%) did contribute to the measured signal. It was concluded that there was no significant loss of signal due to quenching by fringe fields.

It was demonstrated that the signal saturated as the applied field was increased and the effective lifetime of the $2s$ state became essentially twice that of the $2p$ state. The difference between the signal with the quench field on and with it off should represent the field-quenched emission from the $2s$ state. It was observed that when the quench field was turned off there was an appreciable background signal. The sources were not completely identified, but the signal included components caused by impact of the beam on surfaces and excitation of background gas. There was concern that when the quench field was turned on this background might change, particularly due to the alteration in trajectory of the projectile ions and acceleration of stray electrons onto metal surfaces. This problem was obviated by placing before the detection region a "prequench" electric field parallel to the beam axis. The prequench field had the function of removing the metastables from the beam before it entered the observation region; tests indicated that removal was 97% efficient. Background signals observed by the photon detector will be unaffected by whether the prequench field is on or off. The quench field in the detection region was maintained slightly above the value which produced saturation in the signal; the difference between the signal with the prequench off and the signal with the prequench on was taken as the true signal from quenching of metastables.

Under high-quenching fields sufficient to ensure complete mixing of the $2s$ and $2p$ levels, the effective lifetime of the metastable state is 3×10^{-9} sec, twice that of the $2p$ level. The decay length (product of impact velocity and lifetime) in the quenching electric field is comparable with the field of view of the detector. Consequently as velocity changes, the distribution of emitters in the quench region will also be altered. In the event that the efficiency of the photon detector varies with the angle of incidence of the photon, the detector sensitivity might exhibit a dependence on impact velocity. Tests are required to assess the magnitude of this effect. The lifetime of the H($2s$) state is dependent on the strength of the quenching electric field and may be predicted theoretically, following the work of Bethe.[4] It would be possible to guarantee velocity-independent detection efficiency by varying quenching field with velocity to maintain a constant decay length. This does have the disadvantage, however, that quenching fields will be less than that for an optimum efficiency; and therefore signal-to-noise ratios are degraded. In the present experiment the detection efficiency was maintained at its optimum value using saturation fields. A test of the velocity independence of this efficiency

was carried out by measuring the ratio of the signal under optimum quench field to the signal at a lower field where decay length was kept constant; the variation of this ratio with impact velocity reflects changes in detection sensitivity. This test indicated that the magnitude of the optimum detection efficiency varied by no more than 10% over the impact energy range 4–26 keV. Rather than make a correction for this change, we choose to regard it as a contributing factor to the limitation of accuracy with which the cross sections were determined.

It has recently been shown[5] that the field-induced Lyman-α emission will be polarized by an amount which varies with field strength. Polarization is related to anisotropy of emission. An experiment which detects photons emitted into a limited solid angle will therefore experience a change in effective detection sensitivity with electric field. The test described above depends upon the detection efficiency at a series of selected low fields being independent of impact velocity. Using the theoretical prediction of polarization of Sellin *et al.*[5] it is readily shown that over the range of low fields used to maintain constant decay length (30–40 V/cm) the detection efficiency of the system varied by a negligible amount[6] (less than $\frac{1}{4}$%). The high-quench field used during cross-section measurements was not maintained constant; various values were employed between 300 and 600 V/cm, depending on projectile energy; the changing polarization contributes to the variation of detection efficiency with projectile energy that is identified by the tests described above. In conclusion, the existence of the field-dependent polarization does not invalidate the result that detection efficiency changes by less than 10% over the impact energy range of this experiment.

Care was taken to ensure that no appreciable fraction of the flux of metastable atoms was lost before the projectile beam entered the detection region. Loss due to interception by the exit aperture of the gas cell was assessed from a study of the angular distribution of the metastables to be less than 1%. The possibility that metastables were destroyed by collisions with background gas was shown to be negligible by demonstrating independence of signal from background pressure. Destruction due to stray-field quenching was prevented by complete shielding of the beam from high-voltage leads and insulating surfaces; the fringing of fields from the quenching regions was minimized by grounded shielding. It was estimated that with the precautions described above, the loss of metastables did not amount to more than 1% of the flux.

There is a possibility of a spurious contribution to the signal from metastable atoms formed by neutralization of protons traversing the region outside the target cell. Formation of metastables by charge transfer on background gas was evaluated by measuring the metastable signal with the target cell evacuated; this was subtracted from the signal observed with gas in the cell, so arriving at a true signal due to charge transfer on the target medium. In most cases the correction was negligible. The true signal included a contribution due to metastables formed by neutralization on target gas that leaked from the target cell into the main vacuum chamber. This contribution is estimated to be less than 10% of the metastable flux produced in traversing the target cell and has the effect of introducing an uncertainty in the effective thickness of the target. Its presence does not, however, materially influence the present experiment since the data are relative and no attempt was made to determine the true target thickness.

IV. NORMALIZATION OF DATA

It was not the purpose of this present work to measure absolute cross sections. However, recognizing the utility of absolute values in practical situations, the data were assigned absolute values by normalization to previous experiments.

Bayfield[3] noted that there are three independent determinations[1–3] of the cross section for the process

$$H^+ + Ar \rightarrow H(2s) + Ar^+ . \qquad (2)$$

He suggested that since the data agree within 12%, one might normalize future measurements of metastable production to these previous determinations. The apparent agreement of the three independent determinations is somewhat illusory. All three experiments assumed that the field-induced emission was isotropic; Sellin *et al.*[5] showed this assumption to be incorrect; the emission is polarized with respect to the direction of the quenching field. Moreover the degree of polarization is dependent upon the strength of the electric field. Sellin *et al.*[5] calculated the relationship of polarization to the quenching field and confirmed these predictions by experimental measurement. It is not clear whether the polarizations predicted and measured by Sellin *et al.*[5] may legitimately be employed to correct for the polarization-related anisotropy in the published experiments. None of the previous experiments utilize conditions that are similar to those employed by Sellin *et al.*[5] In two of the experiments[1,3] the quenching field is nonuniform; for two of the experiments[1,2] the excited atoms are formed within the quenching field itself. We therefore conclude that all the existing data may be in error due to neglect of anisotropy; moreover, the magnitude of the error cannot be reliably estimated in retrospect. Consequently, there are no reliable data to which the present experiment may

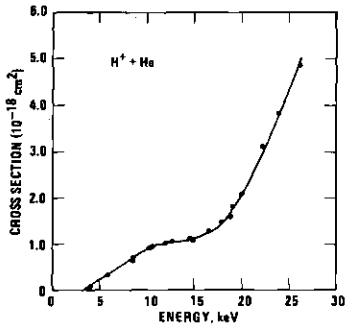

FIG. 2. Cross sections for the formation of H(2s) by impact of H^+ on He.

be normalized.

In order to provide absolute magnitudes we choose to normalize the present results to a cross section of 2.90×10^{-17} cm^2 for the formation of metastable hydrogen by impact of 20-keV protons or argon; this cross section is the mean of the values published in the literature.[1-3] In view of the confusion concerning polarization, no estimate is made of the reliability of these absolute magnitudes.

V. RESULTS

Figures 2–4 show the results of the present experiments; the cross sections are expressed in units of cm^2 per molecule. It is emphasized that the relative values of cross sections for the different targets are obtained directly from the present measurements; the absolute values of the whole set of data are established by normalization to a value of 2.9×10^{-17} cm^2 for the cross section in H^+ + Ar at 20-keV impact energy. Reproducibility of the present data was within ± 5%. Systematic errors in the energy dependence of the data should not distort the ratio of the values of a cross section measured at the extreme energies of the available range by more than 10%. The ratios evaluated for smaller differences in energy will be of higher accuracy. The data represent the cross section for formation of the 2s state by charge transfer and include cascade from higher levels.

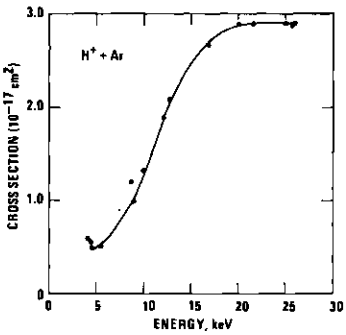

FIG. 3. Cross sections for the formation of H(2s) by impact of H^+ on Ar.

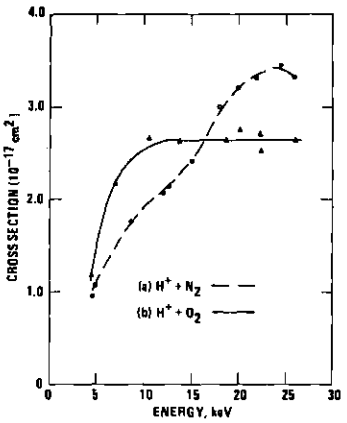

FIG. 4. Cross sections for the formation of H(2s) by impact of H^+ on (a) N_2 and (b) O_2.

The present results may be compared with previous experiments using targets of He and Ar. There is considerable disagreement between the absolute values in the previous data, reflecting the difficulty of carrying out accurate absolute determinations of emitted light intensity. Since the present data are relative rather than absolute, the most valuable comparisons may be carried out in terms of the relative variations of cross section with impact energy. Such a comparison is shown in Figs. 5 and 6, which include all available data for targets of He and Ar normalized together at

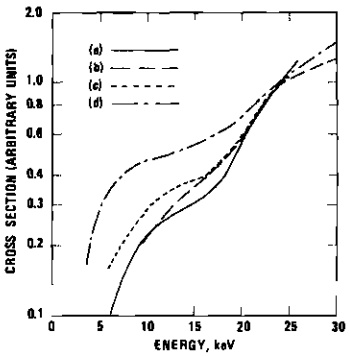

FIG. 5. Comparisons of data for formation of H(2s) by impact of H^+ on a He target. All data are shown normalized at an energy of 24 keV. (a) Present work, (b) Andreev *et al.* (Ref. 2), (c) Jaecks *et al.* (Ref. 1), (d) Dose (Ref. 7).

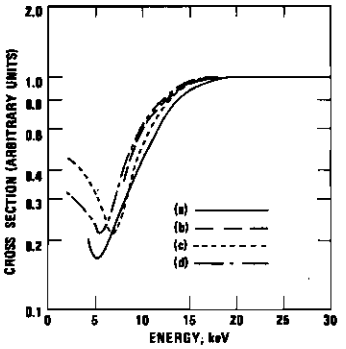

FIG. 6. Comparisons of data for formation of H(2s) by impact of H^+ on an Ar target. All data are shown normalized at an energy of 24 keV. (a) Present work, (b) Andreev *et al.* (Ref. 2), (c) Jaecks *et al.* (Ref. 1), (d) Bayfield (Ref. 3).

an energy of 24 keV. It is clear that appreciable disagreement exists among the various authors. In the case of the helium target, if one neglects the work of Dose,[7] the remaining values diverge by up to 12% from the mean. For argon all data lie within 15% of the mean down to an energy of 6 keV; below this point the divergence is more serious. The various apparatus used in these measurements are of different design; thus instrumental errors in the data may differ from one experiment to another. The contribution of cascade, coming primarily from the $3p - 2s$ transitions, will vary from one experiment to another due to the different geometrical configurations. However, the direct measurements by Andreev *et al.*[8] of the $3p$ cross section at energies above 10 keV indicate that cascade cannot exceed 4% for any of these determinations; thus cascade is a small contribution to the measured cross sections and cannot contribute significantly to the discrepancies. In all experiments there is a danger that the detection sensitivity will vary with energy; the work of Jaecks *et al.*[1] contains such an error amounting to 10% or more due to Doppler shift of emission[9]; the techniques of Andreev *et al.*[2] inherently exclude this type of error; the present work has assessed such errors to be less than 10%; the remaining experiments ignore the problem.

It is not possible to make a definite identification of sources of error to explain the discrepancies between measurements. Consequently, one cannot use objective criteria to select one set of data as being more accurate than the others. Excluding the work of Dose, which exhibits a considerable disagreement with the other determinations, one may conclude that the available data establish the energy dependence of the cross sections to an accuracy of ± 15%. Within this uncertainty the results of the present experiment are consistent with previous work.

Gaily[10] carried out a comparison with theory of the cross-section data for a helium target. It was shown that a coupled-state calculation[11] provides the best description of the process at energies below 30 keV, but there remains a considerable discrepancy between theory and experiment.

There are no previous data for N_2 and O_2 targets with which the present measurements may be compared. It is interesting that these two cross sections are of about the same magnitude but exhibit different dependence on energy; this indicates perhaps that the charge-transfer mechanism is sensitive to the detailed electron structure of the target. Mapleton[12] has calculated capture into the 2s state for targets of O and N using the orthogonalized Brinkman-Kramers (OBK) approximation. It might be expected that the cross section for atomic O or N will be roughly equal to half that for the O_2 and N_2. In fact the theory lies as much as one order of magnitude higher than experiment and exhibits a greatly different dependence on energy. This is not too surprising since the OBK approximation is designed for use at higher impact energies than the present experiment.

---

*Work partially supported by NASA and by the Controlled Thermonuclear Division of the AEC.

[1]D. Jaecks, B. van Zyl, and R. Geballe, Phys. Rev. 137, A340 (1965).

[2]E. P. Andreev, V. A. Ankudinov, and S. V. Bobashev, Zh. Eksperim. i Teor. Fiz. 50, 565 (1966) [Soviet Phys. JETP 23, 375 (1966)].

[3]J. E. Bayfield, Phys. Rev. 182, 115 (1969).

[4]H. A. Bethe and E. E. Salpeter, *Quantum Mechanics of One- and Two-Electron Atoms* (Academic, New York, 1951).

[5]I. A. Sellin, J. A. Biggerstaff, and P. M. Griffin, Phys. Rev. A 2, 423 (1970).

[6]The theoretical predictions by Sellin *et al.* (Ref. 5) were confirmed experimentally using a quench-field configuration that exhibits no significant difference from that used in the present experiments. A small error in either the predicted or measured polarizations will not significantly affect the validity of the present tests.

[7]V. Dose, Helv. Phys. Acta 39, 683 (1966).

[8]E. P. Andreev, V. A. Ankudinov, S. V. Bobashev, and V. B. Matveev, Zh. Eksperim. i Teor. Fiz. 52, 357 (1967) [Soviet Phys. JETP 25, 232 (1967)].

[9]B. van Zyl, Phys. Rev. 136, A1561 (1964).

[10]T. D. Gaily, Phys. Rev. 178, 207 (1969).

[11]L. T. Sin Fai Lam, Proc. Phys. Soc. (London) 92, 67 (1967).

[12]R. A. Mapleton, Proc. Phys. Soc. (London) 85, 1109 (1965).

REFERENCES*

1. G. J. Lockwood and E. Everhart, Phys. Rev. 125, 567 (1962).

2. F. P. Ziemba, G. J. Lockwood, G. H. Morgan, and E. Everhart, Phys. Rev. 118, 1552 (1960).

3. D. H. Jaecks, D. H. Crandall, and R. H. McKnight, Phys. Rev. Letters 25, 491 (1970).

4. M. C. Johnson, Rev. Sci. Instr. 40, 311 (1969).

5. S. K. Allison and M. Garcia-Munoz, Atomic and Molecular Processes, edited by P. R. Bates (Academic Press, New York and London), Chapter 19.

6. J. B. H. Stedeford and J. B. Hasted, Proc. Roy. Soc. (London) A227, 466 (1955).

7. F. J. DeHeer, J. Schutten, and H. Maustafa, Physica 32, 1766 (1966).

8. P. M. Stier and C. F. Barnett, Phys. Rev. 103, 896 (1956).

9. J. F. Williams and D. N. F. Dunbar, Phys. Rev. 149, 62 (1966).

10. L. Colli, F. Cristofori, G. E. Frigerio, and P. G. Sona, Phys. Letters 3, 62 (1962).

11. D. Jaecks, B. Van Zyl, and R. Geballe, Phys. Rev. 137, A340 (1965).

12. V. Dose, Helv. Phys. Acta, 39, 683 (1966).

13. G. Ryding, A. B. Wittkower, and H. G. Gilbody, Proc. Phys. Soc. 89, 547 (1966).

14. E. P. Andreev, V. A. Ankudinov, and S. V. Bobashev, Soviet Phys. - JETP 23, 375 (1966).

15. R. L. Fitzwilson and E. W. Thomas, Phys. Rev. A3, 1305 (1971).

*Abbreviations used herein follow the form outlined in the Style Manual of the American Institute of Physics

16. W. L. Fite and R. T. Brackmann, Phys. Rev. 112, 1151 (1958).

17. J. A. R. Samson, J. Opt. Soc. Am. 54, 6 (1964).

18. H. F. Helbig and E. Everhart, Phys. Rev. 136, A674 (1964).

19. D. H. Crandall, Thesis, University of Nebraska, August 1970.

20. F. Christofori, P. Fenici, G. E. Frigerio, N. Molho, and P. G. Sona, Physics Letters 6, 171 (1963).

21. V. Dose, Helv. Phys. Acta, 41, 261 (1968).

22. V. Dose and V. Meyer, Physics Letters 23, 69 (1966).

23. D. H. Jaecks, R. H. McKnight, and D. H. Crandall, Sixth International Conference on the Physics of Electronic and Atomic Collisions, Cambridge, Massachusetts, (M.I.T. Press, Cambridge, 1969) p. 862.

24. T. Dean Gaily, Phys. Rev. 178, 207 (1969).

25. N. F. Mott and H. S. W. Massey, The Theory of Atomic Collisions, (Oxford University Press, London, 1965), third edition.

26. J. P. Coleman and S. Trelease, J. Phys. B. (Proc. Phys. Soc.), 1, 172 (1968).

27. B. H. Bransden, Advances in Atomic and Molecular Physics, edited by D. R. Bates and Immanuel Estermann (Academic Press, Inc., New York, London, 1965), p. 85.

28. M. R. C. McDowell and J. P. Coleman, Introduction to the Theory of Ion-Atom Collisions, (North-Holland Publishing Company, Amsterdam, London, 1970), chapter 8.

29. D. R. Bates, Atomic and Molecular Processes, edited by D. R. Bates (Academic Press, New York and London, 1962), chapter 14, Sec. 1.13.

30. A. Salin, J. Phys. B.: Atom. Molec. Phys. 3, 937 (1970).

31. J. P. Coleman, Case Studies in Atomic Collision Physics, edited by E. W. McDaniel and M. R. C. McDowell (North-Holland Publishing Company, Amsterdam-London, John Wiley & Sons, Inc. -- New York, 1969), chapter 3.

32. B. M. Smirnor, High Temp. 4, 407 (1966).

33. N. F. Mott and H. S. W. Massey, The Theory of Atomic Collisions (Oxford University Press, London, 1965), third edition, Chapt. XV, Sec. 2.

34. N. F. Mott and H. S. W. Massey, The Theory of Atomic Collisions (Oxford University Press, London, 1965), third edition, Chapt. V, Sec. 5.

35. H. Goldstein, Classical Mechanics, (Addison-Wesley Publishing Company, Inc., 1965), Chapt. 3.

36. E. W. McDaniel, Collision Phenomena in Ionized Gases (John Wiley & Sons, Inc., New York, 1964), Sections 3-10 and 4-10.

37. E. H. S. Burhop, Quantum Theory I. Elements, edited by D. R. Bates (Academic Press, Inc., New York, 1961), Chapt. 9.

38. N. Bohr, Kgl. Danske Videnskab. Selskab, Mat.-fys. Medd. 18, No. 8 (1948).

39. E. Everhart, G. Stone, and R. J. Carbone, Phys. Rev. 99, 1287 (1955).

40. Felton W. Bingham, J. Chem. Phys. 46, 2003 (1967).

41. F. T. Smith, V. International Conference on the Physics of Electronic and Atomic Collisions, Leningrad, U.S.S.R., July 17-23, 1967, Abstracts of Papers, page 181.

42. E. H. Kennard, Kinetic Theory of Gases (McGraw-Hill, 1937).

43. F. T. Smith, R. P. Marchi, and K. G. Dedrick, Phys. Rev. 150, 79 (1966).

44. T. A. Green, H. E. Stanley, and You-Chien Chiang, Helv. Phys. Acta 38, 109 (1965).

45. B. H. Bransden and L. T. Sin Fai Lam, Proc. Phys. Soc., 87, 653 (1966).

46. R. K. Colegrave and D. B. L. Stephens, J. Phys. B. (Proc. Phys. Soc.) (GB), 1, 856 (1968).

47. L. T. Sin Fai Lam, Proc. Phys. Soc. (GB) 92, 67 (1967).

48. I. A. Polvektov and L. P. Presnyakov, Soviet Phys.-JETP, 27, 67 (1968).

49. W. Lichten, Phys. Rev. 131, 229 (1963).

50. W. Lichten, Phys. Rev. 139, A27 (1965).

51. H. H. Michels, J. Chem. Phys. 44, 3834 (1966).

52. J. Durup, P. Fournier, and P. Dông, J. Mass Spectrometry and Ion Physics, 2, 311 (1969).

53. T. A. Green and James M. Peek, Phys. Rev. 183, 166 (1969).

54. G. W. McClure, Phys. Rev. 140, A769 (1965).

55. D. R. Sweetman, Proc. Roy. Soc. (London), A256, 416 (1960).

56. D. K. Gibson, J. Los, and J. Schopman, Physica 40, 385 (1968).

57. K. K. Damodaran, Proc. Roy. Soc. (London), 239, A769 (1957).

58. N. V. Fedorenko, V. V. Afrosimov, R. N. Il'in, and D. M. Kaminker, Soviet Phys.-JETP, 9, 267 (1959).

59. C. F. Barnett, M. Rankin, and J. A. Ray, Proceedings of the Sixth International Conference on Ionization Phenomena in Gases (Paris 1963), Vol. I, page 63.

60. D. K. Gibson and J. Los, Physica, 35, 258 (1967).

61. G. W. McClure, Phys. Rev. 130, 1852 (1963).

62. J. M. Peek, Phys. Rev. 140, A11 (1965).

63. H. J. Walter and G. E. Kimball, Quantum Chemistry, (John Wiley & Sons, Inc. New York, 1965), thirteenth printing, Chapt. XI.

64. W. McGowan and L. Kerwin, Can. J. Phys. 41, 316 (1963).

65. S. Dushman, Scientific Foundations of Vacuum Technique (John Wiley & Sons, Inc., New York, 1962), second edition, page 58.

66. R. V. Churchill, Complex Variables and Applications (McGraw-Hill, 1960), second edition, Chapt. 8.

67. J. B. Hasted, Physics of Atomic Collisions (Butterworths; London, 1964), Chapter 12, Section 33.

68. R. D. Evans, The Atomic Nucleus (McGraw-Hill, 1955), Chapter 28.

69. E. P. Andreev, V. A. Ankudinov, S. B. Boboshev, and V. B. Matveyev, Soviet Physics-JETP, 25, 232 (1967).

70. T. E. Sharp, Potential Energy Diagram for Molecular Mydrogen and Its Ions, Lockheed Aircraft Corporation, Report No. LMSC 5-10-69-9 (1969).

71. B. Van Zyl, B. Jaecks, D. Pretzer, and R. Geballe, Phys. Rev., 136A, 1951 (1964).

72. G. Lüders, Z. Naturforshg, 5a, 608 (1950).

73. J. E. Bayfield, Phys. Rev. 182, 115 (1969).

74. L. H. Toburen, M. Y. Nakai, and R. A. Langley, The Measurement of High Energy Charge Transfer Cross Sections for Incident Protons and Atomic Hydrogen in Various Gases, Ph.D. Thesis of Toburen, (Oak Ridge National Laboratory Report ORNL-TM-1988, 1967) page 215.

75. I. A. Sellin, J. A. Biggerstaff, and P. M. Griffin, Phys. Rev. A2, 423 (1970).

76. I. C. Percival and M. J. Seaton, Phil. Trans. Roy. Soc. (London), A251, 113 (1958).

77. H. A. Bethe and E. E. Salpeter, Quantum Mechanics of One- and Two-Electron Atoms, (Academic Press, Inc., New York, 1957), Sec. 67.

78. E. S. Chambers, Phys. Rev. 133, A1202 (1964).

79. P. M. Stier, C. F. Barnett, and G. E. Evans, Phys. Rev. 96, 973 (1954).

80. R. Dagnac, D. Blanc, and D. Molina, J. Phys. B: Atom. Molec. Phys. 3, 1239 (1970).

81. P. M. Stier and C. F. Barnett, Phys. Rev. 103, 896 (1956).

82. J. B. M. Stedeford and J. B. Hasted, Proc. Roy. Soc. (London) A227, 466 (1955).

83. F. J. DeHeer, J. Schutten, and H. Moustafa, Physica, 32, 1766 (1966).

84. J. F. Williams and D. N. F. Dunbar, Phys. Rev. 149, 62 (1966).

85. I. P. Skalskaya, Zh. Tekhn., Fiz., 24, 1912 (1954) [translated AEC-tr-2741].

86. D. M. Kaminker and N. F. Fedorenko, Zh. Tekhn., Fiz., 25, 2239 (1955) [translated AEC-tr-2745].

87. L. G. Fillipenko, Zh. Tekhn., Fiz., 30, 57 (1960) [Soviet Physics - Tech. Phys., 5, 52 (1960)].

88. G. O. Taylor, Thesis, Georgia Institute of Technology, September, 1969.

89. E. J. Jordan and R. P. Brode, Phys. Rev. 43, 112 (1933).

90. M. A. Menendez, (private communication).

VITA

Roger Louis Fitzwilson was born in Kansas City, Kansas on October 15, 1943. He is the son of Mr. and Mrs. R. E. Fitzwilson. On September 18, 1964, he was married to Phyllis Ann Hitchcox of Pikeville, Tennessee. The couple has two children: a daughter, Mary Ann, born February 27, 1967, and a son, Roger Alan, born October 12, 1969.

Mr. Fitzwilson attended Tucker High School in Tucker, Georgia. In 1961 he entered the Georgia Institute of Technology. During his undergraduate program, he was employed as a Co-operative student by Brown Engineering Company in Huntsville, Alabama, and as a research assistant by the Electronics Division of the Engineering Experiment Station at Georgia Tech. He received the degree of Bachelor of Science in Physics in 1965 and the degree of Master of Science in Physics in 1966. He held a National Aeronautics and Space Administration traineeship for three years of his graduate study.

Mr. Fitzwilson is a member of Sigma Xi, the American Physical Society, Sigma Pi Sigma, Tau Beta Pi, and IEEE.